NON-BROWNIAN PARTICLE SELF-ASSEMBLY FOR HIERARCHICAL MATERIALS DEVELOPMENT

by

Melissa Hanna Lash

B.S., Rutgers, The State University of New Jersey, 2011

Submitted to the Graduate Faculty of

Swanson School of Engineering in partial fulfillment

of the requirements for the degree of

Doctor of Philosophy

University of Pittsburgh

2015

UNIVERSITY OF PITTSBURGH

SWANSON SCHOOL OF ENGINEERING

This dissertation was presented

by

Melissa Hanna Lash

It was defended on

June 19, 2015

and approved by

Joseph J. McCarthy, Ph.D., Professor, Departments of Chemical and Petroleum Engineering

Sanford Asher, Ph.D., Professor, Department of Chemistry

Sachin Velankar, Ph.D., Professor, Department of Chemical and Petroleum Engineering

Dissertation Director: Steven R. Little, Ph.D., Professor, Departments of Chemical and Petroleum Engineering, Bioengineering, and Immunology

NON-BROWNIAN PARTICLE SELF-ASSEMBLY FOR HIERARCHICAL MATERIALS DEVELOPMENT

Melissa Hanna Lash, Ph.D.

University of Pittsburgh, 2015

Colloidal crystals have been explored in the literature for applications in molecular electronics, photonics, sensors, and drug delivery. Much of the research on colloidal crystals has been focused on nano-sized particles with limited attention directed towards building blocks with dimensions ranging from tens to hundreds of microns. This can be attributed, in part, to the fact that particles with greater than sub-micron dimensions do not naturally assemble in an organized fashion over reasonable time-scales due to the relatively small influence of thermalizing forces. Nevertheless, ordered arrays of large, micron-scale particles are of interest as a basis for the production of hierarchically structured materials with customizable pore sizes. Additionally, the ability to create materials from a bottom-up approach with these characteristics would allow for precise control over their pore structure (size and distribution) and surface properties (topography, functionalization and area), resulting in improved regulation of key characteristics such as mechanical strength, diffusive properties, and possibly even photonic properties. In this work, ultrasonic agitation is explored as a means of inducing large, non-Brownian microparticles (18-750 μm) to overcome kinetic barriers to rearrangement and, ultimately, to create close packed, highly ordered, crystals. Using ultrasonic agitation we have been able to create highly-ordered, two- and three-dimensional crystalline structures on a variety of length scales by adjusting external

system properties. Additionally, by mixing particle populations, multicomponent crystals are created with complex organizational patterns, similar to those of stoichiometric chemical structures. By repurposing these crystalline materials as templates, a plethora of new hierarchical microarchitectures can be created for applications in fields such as biotechnology and energy. In this thesis we begin exploring applications in tissue (bone) engineering, catalysis, battery materials and the production of patchy particles via surface modification.

TABLE OF CONTENTS

LIST OF FIGURES

PREFACE

First and foremost I want to thank my advisers Dr. Steven Little and Dr. Joseph McCarthy for their unwavering patience, support and the invaluable education that they provided me with over the past four years. Without their creative inspiration and hands-on mentoring**,** this thesis and the experimental work that comprises it, would not have been possible. I also want to thank Dr. Morgan Fedorchak for her guidance and encouragement towards my scientific success. She has truly helped me to grow both personally and professionally over the past four years. My committee members, Dr. Velankar and Dr. Asher have also been instrumental in guiding me and generating ideas for this research. Additionally, I am grateful for the support of our collaborators in Dr. Kumta and Dr. Veser's labs for their enthusiasm and dedication towards driving our joint research forward. Thank you all for your personal mentorship and for pushing me to explore new ideas and take this research farther than I though was possible.

On a personal note**,** I would like to give a heartfelt thank you to my family, especially my parents, Faye and Alan, and my sister Jessica whose never-ending patience and encouragement has helped me through the past four years. I'd also like to give a huge thanks to my friends who have supported me on a daily basis and helped me prepare this body of work. Specifically, all of the members of the Little and McCarthy labs (past and present) who I have worked with have taught me so much throughout our daily scientific/life discussions and "meetings" at conference room FF. My lab mates and ChE friends have shown me how to communicate more effectively, run faster, climb my stress away, endure 'life and times", understand the true meaning of granola

and explore countless amazing experiences (and food) throughout Pittsburgh. You have all been inspirational in my graduate career and have helped make the past four years so enjoyable. I am truly grateful to have had the opportunity to go through this journey with all of you.

Furthermore, I would like to acknowledge Dr. Alex Harmon and Dr. Kathryn Uhrich at Rutgers University for encouraging me as an undergraduate student to attend graduate school and for stimulating my love for research and scientific experimentation.

1.0 INTRODUCTION

This chapter is adapted from Lash, M. H., Fedorchak, M. V., McCarthy, J. J., & Little, S. R. (2015). Scaling up self-assembly: Bottom-up approaches to macroscopic particle organization. *Soft Matter*. DOI 10.1039/C5SM00764J.

Naturally occurring materials are elegant and sophisticated in structure, often with hierarchical features ranging in size from the nano- to macro- scales. The structural form, or architecture, of a material often dictates its function. For example, the highly regular brick-and-mortar layering of organic and inorganic elements in nacre (mollusk shell) create a strength, toughness, and hardness that makes nacre an excellent protective material for sea creatures due to the way stress propagates through it and energy is dissipated.[1–3] Similarly, the structural hierarchy of cells naturally present in cedar wood and lotus leaves highly favors efficient light harvesting due to the cellular organization, providing the ability to both focus and scatter light in different areas to maximize photosynthesis.[4] This tendency for the form or structure of a material to dictate its function is ubiquitously observed throughout the natural world, inspiring and challenging mimetic scientific design. Along these lines, hierarchy, ranging from the nano- to macro- scales, has been found to enhance material performance (e.g. strength, toughness, luminescence, electron and ion transfer, etc.). In the design of synthetic materials, mimicking natural hierarchies may enhance the intrinsic properties and usability of the designed material.[4–9] Figure 1 shows naturally occurring materials with macroscale features. One such example is the macroscopic pore structure seen in native bone

that allows for the tissue to have high mechanical strength and low material density.[6,8] Similarly, the organization of photoreceptors in the drosophila (fruit fly) eye allows the insect to have a wide field of vision.[10,11] The organization and complexity of these structural features has inspired scientific study and mimetic design across many fields of research.

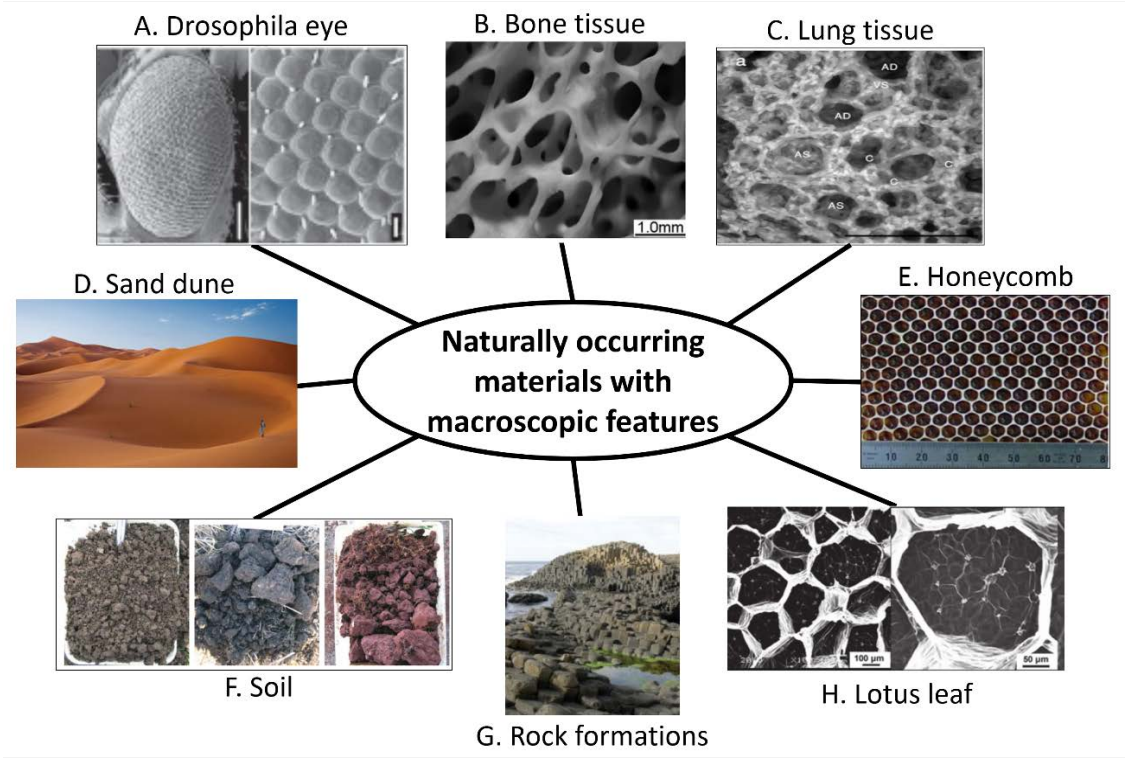

Figure 1: Naturally occurring materials with macroscopic features which directly impact the structures function and structural integrity. In part A, scale bars are 100µm and 10µm respectively and is reproduced with permission from ref. [12], Copyright 2008, Nature Publishing Group 2008; Part (B) reproduced with permission from ref. [13], Copyright 2005, John Wiley and Sons 2005; Part (C) reproduced with permission from ref. [14] Copyright 2014, Nature Publishing Group; Part (D) reproduced with permission from ref[15] Copyright 2007, Nature Publishing Group; Part (E) reproduced with permission from ref. [16] Copyright 2008, Springer; Part (F) reproduced with permission from ref [17] Copyright 2011, John Wiley and Sons; Part (G) reproduced with permission from ref. [18] Copyright 2011, John Wiley and Sons; Part (H) reproduced with permission from ref. [19] Copyright 2008, AIP Publishing LLC.

Interestingly, mimicking these macroscopic features is not trivial to accomplish synthetically. Frequently, natural materials assemble in an autonomous fashion through a process known as self-assembly.[20,21] In order to copy this behavior in a lab, researchers have sought to understand the underlying principles governing self-assembling systems with building blocks ranging from proteins to pieces of hot dog.[20–24] For self-assembling systems, the assembly is dictated by the properties of the building blocks and the spontaneous physical and/or chemical interactions that occur among them (with little to no external guidance). The assembly can also be controlled by regulating environmental features, such as the container, charge, and solution in order to determine accessible organizational configurations. The collective characteristics of these building blocks within their environment can be thought of as a set of "directions" for the assembly process. In this way, the size and material composition of the building blocks greatly impacts the organizational complexity of the resulting structure.[24–26] For atomic, molecular, and nanoscale building blocks, self-assembly is a highly accessible fabrication method. Many techniques have been developed to take advantage of natural nano-scale self-assembly with great success, likely due to the strong influence of Brownian motion. However, as the components of a system grow in size, gravity becomes increasingly influential over the components and can overpower Brownian forces, which results in incomplete self-assembly and the development of non-organized materials. Specifically, for systems of spheres, larger "non-Brownian" components ($d > 6$ μm) are more likely to settle into a randomly configured non-equilibrium metastable states, rather than self-assembling into (typically lower energy) crystalline ones.[27] Often for crystallization to occur with macro-sized spherical particles, there must exist a balance between the system's thermodynamic equilibrium state (being an organized and assembled one) and its kinetics, or the time over which self-assembly can occur.[28]

To induce particle motion and subsequent self-assembly in systems where Brownian motion is not a timely driver for crystallization, the most common method for artificially thermalizing a system of non-Brownian particles involves agitation. Adding agitation to a system of particles often leads to enhanced interparticle collisions and interactions in a way that mimics the effects of Brownian motion. For 100 μm particles undergoing agitation (in the form of indirect ultrasonic waves, for example) the time for which self-assembly occurs for a system of particles can be reduced to be on the order of minutes, with the individual particles moving substantially faster as they interact.[29] By analyzing multiple methods to fluidize or artificially thermalize large, non-Brownian particles, many new possibilities arise for adapting current colloidal, micro- and macro-particle organization methods to create new, naturally-inspired materials with macroscopic features for applications that have yet to be explored.

Traditionally, the creation of synthetic materials with macroscopic building blocks has been conducted through top-down methods. In contrast with self-assembly or other bottom-up methods, top down fabrication methods require an external assembler (such as a robot) to drive the assembly based on information stored in a centralized location, such as a blue print. The complexity of the assembled structure stems from the "assemblers" capabilities rather than the building blocks themselves. However, by understanding how to manipulate the building blocks, control over the entire assembly process can be achieved using bottom-up strategies. New routes for bottom-up micro- and nanofabrication as well as a direct path to better design artificial self-assembling systems (albeit synthetically induced) arise from exploring opportunities to expand bottom-up assembly processes to larger building blocks.[20,25,30–32] Manipulating the interactions among individual building blocks leads to method development where precise control over the bulk properties of the resulting material can be obtained. For example, tailoring the building blocks

and their orientation, with respect to each other, leads to changes in the overall pore structure (size and distribution) and surface properties (topography, functionalization and area) of a material, which in turn lead to improved regulation over the material's key functional characteristics such as mechanical strength, diffusive properties, and potentially photonic capabilities.[33–35] The applications of these functional characteristics have the potential to lead to a whole new field of self-assembled, ordered materials on a scale that has been largely untapped to date. This Chapter will present a summary of methods for rationally designing and characterizing materials that exhibit macroscale features and are derived from non-Brownian particles through self-assembly. We describe assembly routes for forming macro-crystalline arrays from spherical building blocks that span from the submicron to centimeter scales and that are comprised of materials ranging in composition. The versatility of these approaches for manipulating non-Brownian particles have wide appeal for designing novel particle-based materials on all scales.

1.1 FABRICATION METHODS FOR CREATING CRYSTALS FROM SPHERICAL NON-BROWNIAN PARTICLES

Multiple methods to artificially thermalize and self-assemble large, non-Brownian particles have been developed as a means of fabricating (non-) colloidal crystals with macroscopic features. These methods are largely dependent on an artificial agitation source, manipulating the solvent evaporation rate, customizing the substrate and/or varying the viscosity and cohesiveness of the dispersion medium. Adjusting these environmental parameters in some cases emulates Brownian phenomena and heightens the influence of system thermalization on non-Brownian particles. With respect to particle motion and position adjustability, Brownian particles naturally move erratically

through space and explore the physical and energy landscapes before eventually settling. Upon settling, they arrange into a structure which has minimized the free energy of the system. Since non-Brownian particles are not highly influenced by thermal motion, an external stimulus provides this artificial thermalizing force. Particles must have the freedom (as a consequence of the artificial thermalizing energy) to interact with each other and their environment in order to lead to self-assembly. Through these interactions, however, both attractive and repulsive forces influence the organizational state of the crystalline (or non-crystalline) structure formed. Although inter-particle collisions will lead to overall energy dissipation throughout a system of particles, as long as the total energy input to the system is greater than the rate of dissipation, the necessary freedom for erratic and exploratory particle motion is achieved.[20,36,37] Exploring this balance between fluctuational energy (either natural or externally applied) and dissipation has allowed Klotsa and Jack[38] to model the equilibrium dynamics of colloidal systems. Their work describes kinetically trapped states at different time stages throughout the crystallization process and supports the suggestion of Whitesides and Boncheva,[37] describing that particles must be able to adjust their positioning in order to effectively assemble into a periodically ordered structure. Adjustability, or the capability to reverse "incorrect" bonding between particles, avoids kinetic entrapment prior to reaching the minimum free energy state, preventing the development of disorder.[21,28,37] Figure 2 depicts the natural tendency for particles ranging from 548 nm to 1.56 mm to assemble or become kinetically trapped both in the presence and absence of an external agitation source. External agitation is seen to have a substantial impact on the non-Brownian particles where, in the absence of agitation, kinetic entrapment is seen to occur prior to crystallization. In contrast, in the case of Brownian particles, thermal energy naturally induces particle motion; thus, self-ordering occurs regardless of the externally imposed agitation. For crystallization to occur among non-Brownian

particles, constraints on particle size uniformity exist, similarly to those for colloidal particles (coefficient of variation <5%). Additionally, the driving forces behind self-assembly result from varying interparticle interactions when transitioning from the colloidal or Brownian regime to larger non-Brownian particles. The relative influence of weight (gravity), Van der Waals, electrostatics, and capillary forces changes as the diameter of the particle increases. For larger particles, the influence of weight often dominates. Additionally, mechanical forces derived from interparticle contact can also dictate assembly behavior.[39]

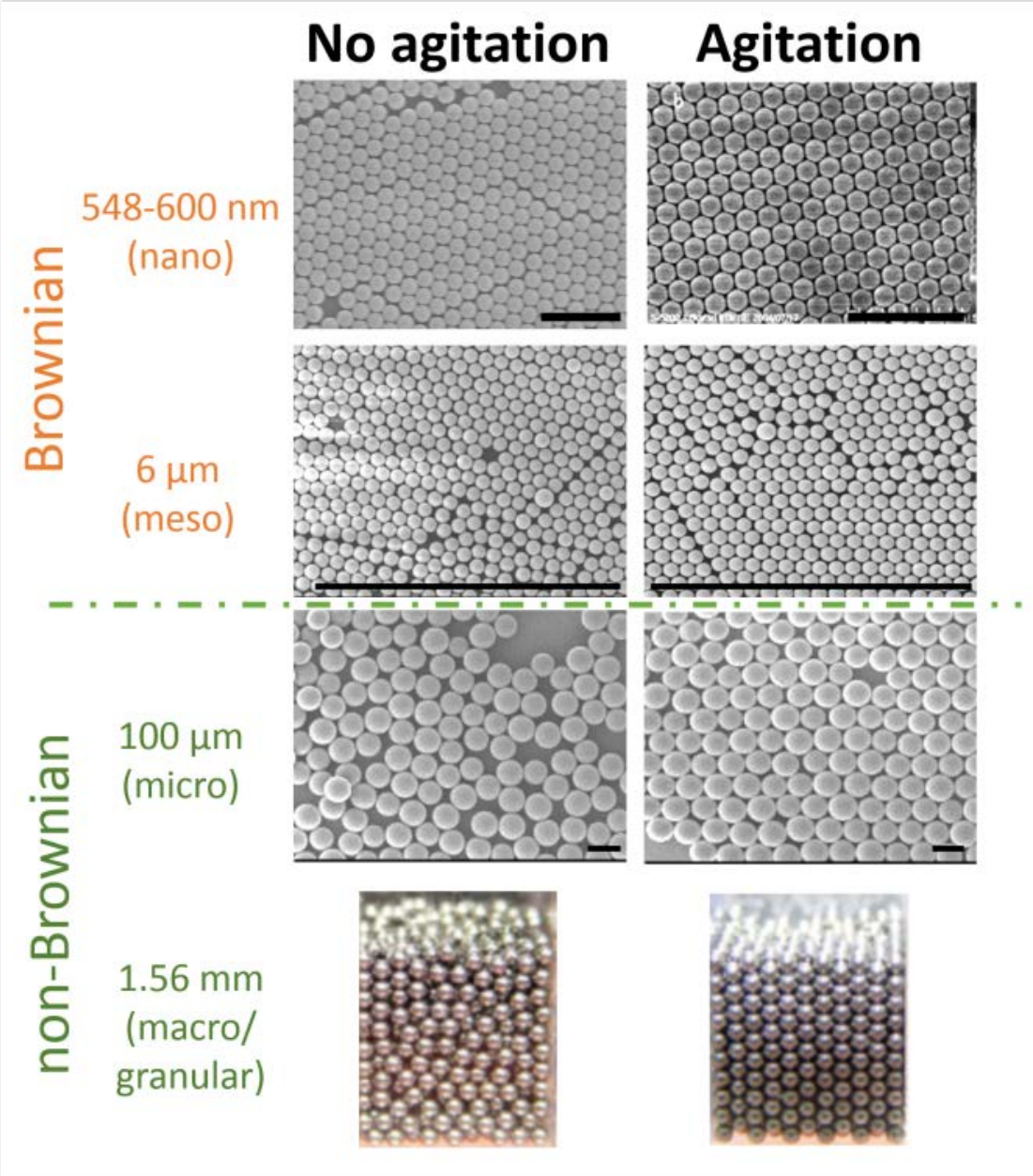

Figure 2: Comparison between nano (scale bar = 5 µm)[29,40], meso (scale bar = 10 µm)[29], micro (scale bar = 100 µm),[29] and macro/granular (scale bar = 3 mm)[27] particle packing under gravity and post agitation (organization induced via sonication bath for d≤100 µm, and sinusoidal vibrations for d=1.56 mm).

Methods for controlling non-Brownian particle assembly can be broken into two large sub-fields in the literature: microparticle assembly and granular assembly. Throughout this Chapter, fabrication methods to mobilize and organize uniformly sized spherical particles in both of these size regimes are described and compared for their commonalities and differences. We will loosely define Brownian particle size ranges as nano (700 nm > d) and meso (800 nm < d < 6 μm), and non-Brownian particle size ranges as micro (6 μm < d < 900 μm) and macro/granular (1000 μm < d) which includes particles with milli- and centimeter dimensions. We acknowledge that the transition between the Brownian and non-Brownian domains is gradual, as Brownian motion is always at play and the gravitational impact scales nonlinearly with particle diameter.[41]

1.1.1 Microparticle assembly for particle-based crystal fabrication

Methods to assemble non-Brownian microparticles have been designed to account for rapid particle sedimentation rates in fluid and the particles' tendency towards kinetic arrest.[29,42] In order to arrange microparticles into crystalline configurations, fluidic forces and solvent evaporation can be controlled and coupled with agitation to increase the time and opportunity for particle interactions.[43,44] The methods described in this Chapter and throughout this thesis do not focus on those induced using only magnets (albeit effective)[45], but rather focus on methods that can be applied to a broader set of particle compositions and particle/solvent combinations.

1.1.1.1 Buoyancy and evaporation induced assembly

Despite the tendency for Brownian forces to have a low impact on larger particle crystallization, these forces can contribute significantly to particle organization when given the proper time and conditions. For example, altering environmental conditions (such as retarding solvent evaporation,

adding thermal energy, and density matching the solvent and particle) can minimize the influence of gravity and enhance the impact of the interparticle interactions governing the overall particle behavior. Two methods to achieve this balance between particle buoyancy and evaporation have been reported in the literature and are summarized below. The first is a Mixed Solvent Evaporation (MSE) method. This process is carried out with 75 μm polystyrene particles in a 3:1 water: dimethylformamide (DMF) solvent. The balance between the solvent evaporation rate and buoyancy allow for enhanced time prior to particle sedimentation, which promotes particle movement and interactions. This MSE method leads to solvent-free crystals forming over the course of days without the need for external agitation. DMF was chosen for being a polar organic solvent with a higher boiling point than water and a density similar to that of polystyrene and water.[46] Based on a similar principle of balancing particle and solvent density, an alternative or second approach is a floating route to self-assembly. This approach has been applied to a system of polystyrene particles ranging in size from 10-240 μm in ethylene glycol at 100 °C in a slightly porous, covered vial. In this floating assembly method, the particles are influenced by a combination of buoyancy, gravity, electrostatics (attractive and repulsive) and lateral capillary forces (floating and immersion). The combination of these forces allows the particles to move and adjust their positioning as they ascend and self-organize at the fluid surface, leaving a particle-based crystal to be recovered upon complete solvent evaporation.[47]

1.1.1.2 Sonication induced assembly

Many groups have employed a sonication bath as a means of agitating particles through an external (non-thermodynamic) energy source. Within a sonication bath, ultrasonic waves emanate from the bath, causing pressure differences within the bath fluid (usually water) resulting in the formation of cavitation bubbles.[48] By altering the bath medium, the impact of the ultrasonic waves and

resulting fluid agitation may be altered and in turn alter particle motion.[29] Kotov and coworkers have shown that exposing large soda lime (SL), polystyrene or poly(methyl methacrylate) (PMMA) microparticles (ranging in size from 75-160 μm) to a slowly evaporating solvent and introducing gentle ultrasonic energy over time leads to the formation of high quality three-dimensional crystalline structures. A solution of particles is slowly added to a vial set on top of a sonication bath cover for exposure to gentle agitation. In this way, direct contact with the bath as a strong agitation source is avoided and only mild agitation is felt by the sample as the particles sediment. After full sedimentation, the sample is removed from the sonication bath and solvent evaporation is allowed to occur over a few days' time.[49–52] An additional method, developed during this work, will be described in Chapter 2.

1.1.1.3 Shaking induced assembly

Several reports also show a method for creating close-packed crystals through orbital or reciprocating shaking. Choi *et al.*[53] create a cubic close packed (CCP) lattice of poly(caprolactone) (PCL) microparticles by exposing a well-mixed, low density particle solution to continuous orbital shaking at 80 rpm throughout the solvent evaporation process. To adapt this method to multiple different types of particles (material compositions) including gelatin, they also add a brief tapping component to their fabrication process.[54] Additionally, Stachowiak *et al.*[55,56] report the assembly of PMMA spheres at a high density (40-65% w/v) solution in 70% ethanol at 250 rpm and 20 °C on a reciprocating shaker until complete solvent evaporation is achieved. They report that subsequent steps of wetting and shaking may be necessary for an ordered crystal to form.

1.1.1.4 Vibrational compacting (tapping) induced assembly

Similar to the shaking induced assembly of microparticles, a mechanical agitation source in the form of tapping applied to a sample can lead to three-dimensional particle assembly. Choi *et al*.[42] present a method for large microparticle crystallization based on substrate geometry and a controlled solvent evaporation rate. Their vertical tapping method was performed on a concave glass dish. Gelatin spheres were allowed time to settle into a randomly packed state and upon vertical tapping on the glass, a periodic, close-packed lattice formed. This tapping method was then modified such that it could be carried out in a plastic centrifuge tube to produce a three-dimensional crystal and in a rectangular mold (at an angle) to produce a two-dimensional crystal. Under these modified conditions, periodic close-packed crystals formed from gentle tapping on the sides of the container during the solvent evaporation process.[44,57]

1.1.2 Granular-particle assembly for particle-based crystal fabrication

Packing granular particles has been widely researched across the literature to study the packing density of particles and powders and their subsequent phase behavior. For example, particles of a variety of material compositions, including glass and metal, have been transformed from a granular gaseous phase to a crystalline one by tuning the vibration applied to the holding container in clever ways. In granular packing, gravity, granular temperature, and energy dissipation are essential variables in determining the crystalline (or non-crystalline) configuration.[58,59] In contrast to the methods described above for microparticles, most granular assembly methods are applied to dry or slightly saturated particle beds, rather than particles submerged in fluid.[27,58,60–63] In the absence of a solvent, there is a change in influential interparticle interactions, resulting in different particle behavior. However, despite this difference, the need for an external energy input to influence self-

assembly remains. These assembly methods are based on energy dissipation and mechanical vibrations and can be broken into two large groups: those aimed at crystallizing a disordered bed of particles and those aimed at creating a crystal through epitaxial (particle-by particle and layer-by-layer) methods.[27,58,61] These two overarching fabrication routes have been largely studied for both dry and cohesive systems under vibrational annealing.[27]

1.1.2.1 Vibration induced assembly of a randomly packed particles

When added to a container and under the influence of gravity, particles tend to organize with a packing density of $\rho \approx 0.6$ into a random configuration. However, by adding vibrations in one (vertical), two (horizontal), and three dimensions (vertical plus horizontal), a slight transformation occurs to increase packing density.[64,65] By tuning the vertical vibrations for a system of stainless-steel beads, Urbach and Olafson[63] created a two dimensional organized layer of particles via vibrational energy imparted to encourage particle-particle collisions. Their studies were among the first to organize granular particles and study the effects of the collision rate (with variables dependent on vibration frequency and amplitude) on the resulting structural order.

However, $\rho=0.6$ is not the upper bound for a three-dimensional granular packing density. By introducing vertical vibration into the system of particles, the packing density can be increased up to $\rho=0.64$, or to a randomly close packed (RCP) configuration.[64] Adding a horizontal or a combination of vertical and horizontal vibrations further increases the packing density to $\rho=0.655$ and 0.661, respectively.[64] The impact of three-dimensional vibrations on glass particle packing was further analyzed by Li *et al*.[65] where their studies show the effects of packing density over time as a function of the vibrational frequency and amplitude. They found that packing density initially increases with vibration amplitude or frequency to a maximum value and then either plateaus or decreases after a certain time period. This upper bound on the packing density is likely

due to jamming and is hard to overcome without batch-wise or continuous addition of particles during the vibrational process.[64]

1.1.2.2 Epitaxial crystal growth

Epitaxial techniques use gravity to create ordered, granular crystals in a piece-wise fashion. The growth is largely governed by particle sedimentation, and is highly dependent on the substrate and suspension properties.[59] Many approaches are based on slow sedimentation of hard spheres, and investigate the effects of varying vibrational amplitude and frequency in all dimensions.[58,64]

Pouliquen *et al*.[66] describe one of the first reports to create crystals from granular glass beads by employing horizontal agitation forces. Their setup is designed to mimic colloidal behavior among non-Brownian particles by introducing chaos into the system via particle-bar collisions during the filling process. They achieve this level of chaos by holding a funnel over horizontal cylindrical bars above a rectangular container, where the arrangement of the bars increases the inter-particle collision rate, and leads to the creation of a more homogeneous distribution of particles. Throughout this process, the container undergoes horizontal vibration and results in the formation of close packed structures. By altering the particle deposition speed and boundary conditions (container size/shape) in relation to particle size, they are able to rationally create large face centered cubic (FCC) and hexagonally close packed (HCP) regions throughout the crystal as well as square packed regions at the free surface. Nahmad-Molinari and Ruiz-Suárez[58] later show that defect free HCP crystals can form in triangular containers by controlling the rate at which steal ball bearings are added and exposed to vertical vibrations. In their experiments, particles are added one by one at a given, controlled frequency. Through this slow, yet continuous addition process, they demonstrate the relationship between energy dissipation

among the particles and the self-stabilization of seed clusters growing into larger crystalline domains.

More recently, Panaitescu and Kudrolli[61] have shown that vibrations are not crucial to the assembly process if a patterned substrate is used in conjunction with a highly controlled particle sedimentation rate. In their studies, gravitational sedimentation can act as the driving force towards crystallization of plastic particles if the deposition rate of particles onto the substrate is sufficiently slow. As the particles individually drop onto the patterned substrate in a continuous fashion, they must independently come to rest, one at a time, without damaging the substrate to produce an ordered structure. If one particle dislodges another particle, the whole particle bed is likely to become disordered. Therefore, tweaking the deposition conditions, the phase state of a packed bed, can be transformed between crystalline (ordered) and amorphous (disordered) states.

The growth of crystals through epitaxial methods is not restricted to a single particle being continuously added over time. Many groups have shown that a batch-wise addition works well to achieve FCC and HCP configurations.[64,65,67] Yu *et al*.[64] show experiment and through simulation that the size of the batch (the number of particles added at a given time) coupled with the vibrational characteristics (frequency and amplitude) has a substantial impact on the crystallization process. Their results suggest that the number of particles added per batch should be equal to the number of particles necessary to fill one complete layer within a given container in order to achieve the densest packing.

1.2 CHARACTERISTICS OF NON-BROWNIAN PARTICLE-BASED CRYSTALS

The characteristics of a crystal, or its form, can directly dictate its functionality as a material. Similar to the Brownian particle self-assembly literature, the non-Brownian particle literature has established ways to characterize crystal quality through the particle packing density, appearance of defects and grain boundaries, and the overall particle coordination or order parameter.

1.2.1 Packing density as a function of the crystal fabrication method

Through the aforementioned fabrication methods, a great number of different organizational configurations, with varying packing densities and stabilities, can be formed.[64,68,69] The Hales proof of the Kepler conjecture illustrates that for perfect hard spheres, the highest packing density achievable is $\rho=0.74$.[68,69] For spherical particles, natural thermalizing forces will naturally draw the components together with a packing density of $0.6<\rho<0.64$, or into a randomly close packed way.[70,71] When agitation in a single direction is added, a randomly close packed arrangement with $\rho=0.64$ repeatedly forms, and with more dynamic vibration (three-dimensional), a close packed structure with $0.68<\rho<0.74$ develops.[64]

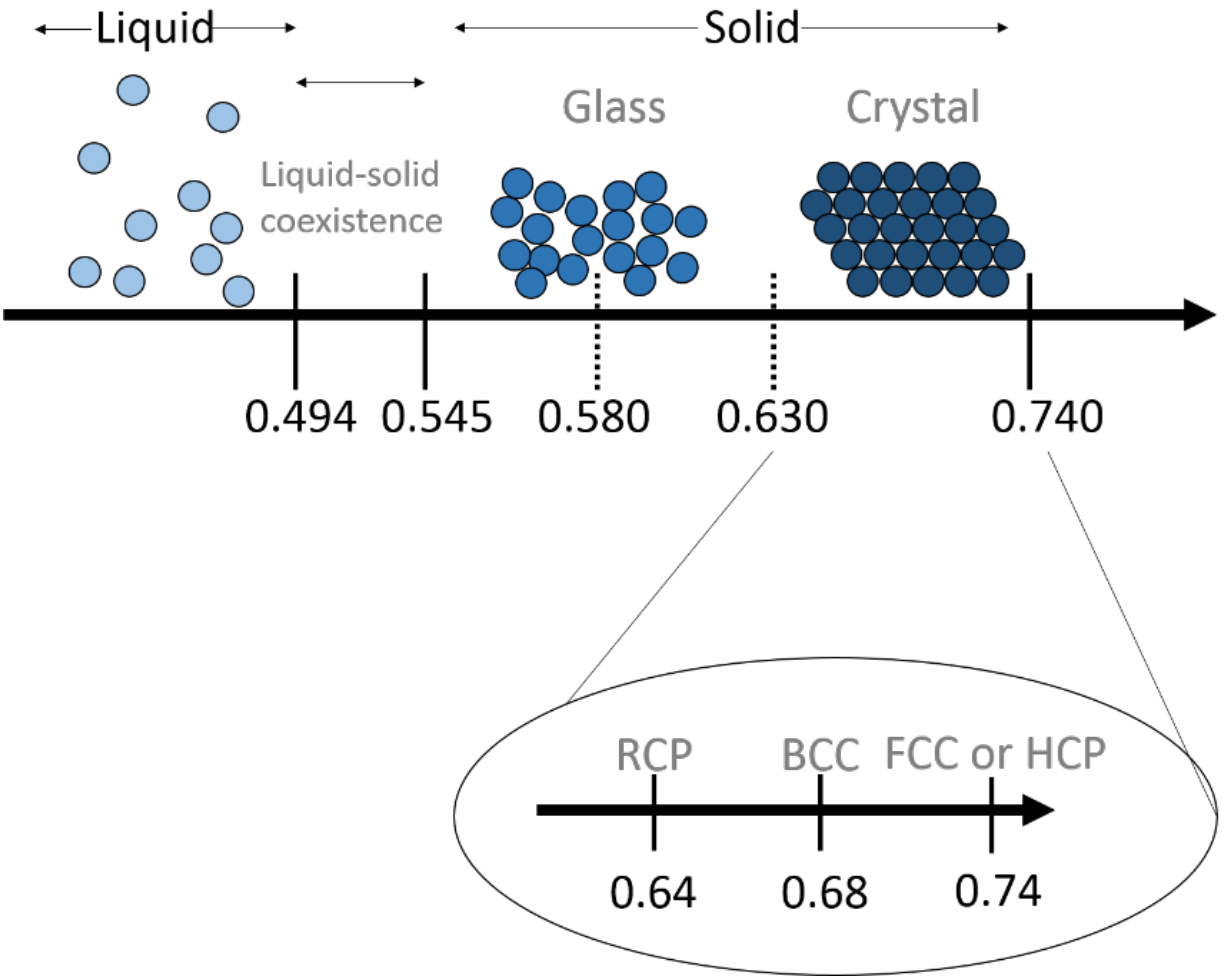

Figure 3: Variation in the particle packing density leads to changes in the phase behavior of a system of particles. The transitions between liquid and crystalline phases for three-dimensional spherical particle systems can be observed for densities ranging from below 0.494 up to 0.74.[59,72,73]

Many methods seek to produce high-density crystals with either HCP or FCC arrangements. From a packing density and thermodynamic viewpoint, these two packing configurations are similar, but from a force dynamics and elasticity perspective, they differ greatly.[74,75] In an FCC structure, each particle is supported by the three particles directly below it. The direct line of contact among the particles is straight and spans the length of the structure. Therefore, when a force is applied to the crystal, it is transmitted in a straight line from particle to particle, forming a triangular pattern at the bottom surface. Conversely, in an HCP structure, the particle-particle contact line does not exist in the form of a continuous straight line. In the HCP arrangement the contact line zigzags, causing the force to be divided across every other layer, resulting in a ring of maximum force.[74]

To deliberately create a packed structure of a certain orientation, strategic utilization of the container shape (triangular, rectangular, cylindrical) and environment can be influential and even predictive in governing the resulting organizational configuration.[60] For example, a triangular container will inhibit the ideal formation of an FCC crystal and a square container will inhibit the formation of an ideal HCP crystal.[27] However, a triangular container can act to promote condensation of an HCP structure.[58] Forming a specific crystal orientation in the improper geometric constraints will lead to the development of defects or grain boundaries throughout the bulk crystal. Furthermore, Carvente *et al*.[27,36] report that changing the saturation within the environment (in addition to container shape) impacts the orientation. Their findings suggest that dry, granular particles in a rectangular container can be coerced to self-assemble into a BCT structure, while cohesive beads form FCC crystals. They conduct this study and make the conformational changes noted by adding defined amounts of oil to their system to tweak the organizational structure right before the system undergoes vibrational annealing. The formation of

liquid bridges between the particles alters the interparticle interactions due to the introduction of capillary forces and helps induce different crystalline orientations.

Similarly to the open systems we have primarily discussed, adjusting the container properties appropriately also provides design control over the resulting crystal orientation when creating crystals in a closed system (where the particles are added to the container prior to vibrational annealing).[27,60] Low ratios of the container diameter to particle diameter have been shown to induce crystallization and increase the overall packing fraction.[76] Organizing particles in narrow containers, for instance, forces the particles to pack in planes parallel to the walls, leading to the formation of body centered tetragonal (BCT) orientations. As the space between the walls increases, the impact of shearing slowly diminishes, and gravity forces the rotation of the plane orientation yielding a diagonal FCC structure (pending that the crystal domain fits within the dimensions of the container.)[60] Studies have shown that when exposed to any type of vibration, the packing density of a particle bed will first increase to a maxima and then plateau or slightly diminish over time. This trend is observed for granular beads both transforming from of a randomly packed particle bed to a crystalline state as well as for those being batch wise added to a particle bed.[64,65] Furthermore, the packing density can be controlled by independently controlling the vibrational amplitude and frequency for crystals produced from both epitaxial and non-epitaxial crystal growth methods.[65] At both low and high frequency and amplitude, the packing fraction remains lower than RCP. Its behavior between these limits is parabolic, showing a maximum at a mid-range for both parameters. Additionally, creating a batch-wise or slow particle addition process aids in the process of increasing packing density, trending towards a higher density corresponding to fewer particles per batch, and more batches.[61,65,66]

1.2.2 Defect development

Colloidal crystals produced via self-assembly consistently form with defects intrinsically embedded within their structure. These defects can be classified into two categories: macro-defects (growth bands and cracks) and micro- defects (vacancies and stacking faults).[77,78] On the nanoscale, defects such as cracks have been shown to form during the solvent evaporation process (due to tensile stress buildup) as the crystal shrinks.[77,79] The formation of a crack is more likely to emerge between hard spheres (as compared to soft spheres) as a method of alleviating built up stress; furthermore, it was found that cracks tend to develop in the direction of the evaporating fluid.[80,81] While a great deal of research has been done among nanoparticles to overcome the challenges associated with defect formation, (such as tuning the particle interaction potential in solution and the drying rate) minimal research has been done to study this phenomenon among non-Brownian particles.[78,82,83] For the microparticle assembly fabrication methods described in Chapter 1.1 that rely on crystallization occurring prior to complete solvent evaporation, we hypothesize that large microparticle-based crystals undergo similar shrinkage and therefore succumb to a similar process of crack formation. The epitaxial granular crystallization methods, however, are often used in systems containing dry particles or slightly damp particles; therefore, they succumb to different interparticle interaction forces and are not as susceptible to crack and defect formation.[58] Nevertheless, defects and polycrystalline states can still form. Increasing the time allowed for the particles to adjust their position before jamming or becoming arrested in place (i.e. through slower particle addition to the particle bed) allows for the dissolution of these defects, resulting in an improved crystalline structure.[58] For this reason, granular crystals, unlike micro- and nano-particle-based crystals, are often grown to be defect-free. In granular distributions, point defects and faults can be created or removed manually by adding/removing a particle or switching

the plane orientation between FCC and HCP during an epitaxial (layer-by-layer) growth process.[27,58,60,84]

There is a large body of literature studying the growth process and lasting effects of defects and impurities within crystalline structures. One of the biggest impacts that defects have on the function of a particle-based crystal comes from a change in the overall packing density, which in turn causes a change in the way that force propagates through the structure (as described in Chapter 1.2).[64,84] Based off of techniques to reduce defects over the entire body of self-assembly induced crystallization literature, precisely controlling the particle environment leads to higher quality crystals forming. For non-Brownian particles, properly sizing the container with respect to the particle diameter can impact the presence (or absence) of defect formation. Additionally with micro- and milli- particles, it has been shown that increasing the intensity of the agitation (to a degree) can also help to reduce the presence of defects.[29,64]

1.2.3 Complex and hierarchical packing structures

Monodispersed, particle-based crystals can be altered to exhibit hierarchical features at the macro, micro- and nano-scales.[85] Adding hierarchy and complexity within a crystal creates the opportunity to form higher density materials as well as control the interparticle spacing between the largest particles. By altering the density and packing orientation of the particles in the crystal, the line of force propagation through the material changes, altering the material's capacity to withstand functional stress and strain.[74,86] Specifically, by incorporating size heterogeneity (in the form of multiple monodispersed particle populations) into the building blocks increases its uses as a templating material.[9] By having multiple different component building blocks, environmental cues and information can be encoded into the structure for different applications, like biological

ones that direct cellular migration or enhance the material's load-bearing capabilities.[6,9,87,88] As a template, the material can be used to form imprints for surface patterning or as a substrate or mold for further material creation.[9,85] In the creation of porous materials, hierarchical or complex particle-based crystals may also simultaneously exploit the advantages provided by multiple pore sizes and increase the available surface area and pore volume of a material. Nano- and micro-sized pores can be combined to create ample reactive sites and interfacial area for reactions to occur as well as provide size-selectivity in filtration. By further combining nano- and micro-sized pores with larger macro-sized pores, mass transport through the structure can be drastically improved by reducing transport limitations innate to singularly smaller pores or a lack of interconnectivity.[89]

Historically, multicomponent crystals have been solely produced from colloidal, or nanoparticles.**[90–92]** Mixtures of Brownian particles can organize into a variety of configurations by varying the number and size ratios of the particles in the mixture. The structures formed are similar to stoichiometric crystals found in nature. However, these types of configurations have not yet been explored on the micron and larger (granular) scales. By creating these stoichiometric structures from larger, synthetic particles, new routes for studying atomic and molecular behavior become more readily available.**[90,91,93,94]** Specifically, varying the number of small (S) to large (L) particles in a binary mixture, or small to medium to large particles within a ternary mixture, allows for a variety of mimetic structures to be created, including those that structurally resemble molecules like $NaSe_8$, $AuCu_3$, AlB_2, NaCl, ZnS, $AlMgB_3$, $AuCsCl_3$, etc.

1.3 CHARACTERIZATION OF CRYSTYLLINE QUALITY

A multitude of order parameters have been developed and validated throughout the literature to assess colloidal crystal quality. In the simplest terms, these order parameters measure how many hard sphere particles are in a given crystalline domain and the orientation of these particles with respect to their neighbors.

Three-dimensional hard sphere dense packing orientations can be described by the commonly used Steinhardt, tetrahedral, or nematic order parameters and have been done so extensively in the literature for both two and three dimensional colloidal crystals. In practice, these types of orientational order parameters (which account for particle coordination) are combined with a translational order parameter (which accounts for the radial distribution function) to describe densely packed particle systems at equilibrium and throughout their process to get there.[71,95] When combining the Steinhardt order parameter with the translational order parameter, a positive correlation emerges for hard sphere systems, revealing descriptive information for systems ranging from jammed states to those in complete disorder to those that are ordered crystals.[71,96,97] The bond orientational order parameter has been shown to accurately describe glassy structures as not purely liquid-like, but rather describes their intermediate states ranging between the liquid and crystal phases.[71,95]

Experimentally, with large amounts of microparticles, or a collection of granular particles (due to their large size), it is also common to measure the average volume or packing fraction through measurements of height and weight (or number of particles) of the packed particle bed.[65,66] In this method, the measurements are fast and easy and can show distinct differences between RCP and FCC/HCP systems.[58,98,99]

1.4 APPLICATIONS OF NON-BROWNIAN PARTICLE-BASED CRYSTALS AND THEIR INVERTED STRUCTURES

Crystals produced from non-Brownian particles offer several different advantages to those produced from Brownian particles.[32] While many of the applications of non-Brownian particles may have overlap with the Brownian regime, a distinct advantage to working with larger particles is simplicity and ease of production and characterization. Since larger building blocks are easier to produce and visually easier to track (with and without a microscope), improved monitoring of the overall crystallization process can be achieved. Larger components also provide more user control in the crystallization process (compared to molecules and nanoparticles) in terms of the strength, range and selectivity of the interparticle interactions.[25,26] By inducing self-assembly to organize non-Brownian particles for macroscale materials design, as described throughout this thesis, the complexity of the material structure can be determined by the building blocks (as a sort of encoded information) rather than by the limitations set forth by the assembler in a top-down assembly process. Advances in non-Brownian particle science make bottom-up assembly a reality for a new regime of building blocks capable of producing metamaterials as well as those with naturally-inspired architectures via cost and time-efficient processes.[32,37]

Additionally, materials with larger pores (as compared to those made from colloids) and structural features are particularly useful for the production of photonic and phononic materials,[35,91,100,101] templating and patterning biological substrates,[102] drug delivery, microelectronics,[25] catalysis,[34,103] filtration, and as model systems to study stress propagation.[60,74] Understanding the behavior of large components, such as millimeter-sized particles, as they crystallize or form densely packed structures can be used in the study of granular flow where crystallization would lead to jamming and complications in industrial production

processes.[60,70,104–106] Further investigation into the packing of non-spherical non-Brownian particles can also lead to the creation of more densely packed structures with wide implications in consumer products and packaging, as in the economically relevant problem of how much grain can fit into a barrel.[69,70] For example, Donev *et al*.[70] demonstrate higher packing fractions for ellipsoid-shaped M&M's, reaching a random packing density approaching ρ=0.74, as compared to ρ=0.64 for RCP spheres. The implications of this work spread beyond the science of M&M's and can be translated industrially for ellipsoids with varying dimensions and material compositions. The underlying physical science driving non-Brownian particle behavior can also be useful in explaining natural phenomena, such as the clotting of blood cells. While a cell is not spherical like the building blocks discussed throughout this thesis, understanding the forces and interactions acting upon larger components in a variety of environments can bring new insight to important biological processes.[107] For instance, understanding the clotting (or aggregation) phenomena of these cells in terms of their physical interactions may help to both promote clotting in wound healing as well as prevent clotting and the associated adverse side effects from clotting-induced ailments (deep vein thrombosis, heart attack, stroke, etc.).[107]

In addition to its uses in manipulating packing density and aggregation, understanding non-Brownian particle behavior leads to the creation of sophisticated templating materials. Non-Brownian particle-based crystals and their inverse structures have created a new subfield of interconnected and readily reproducible scaffolds that are being widely investigated for regenerative medicine applications. Numerous studies have shown enhanced transport of nutrients as well as cellular infiltration throughout inverted crystalline (ICC) scaffolds, for bone and cartilage regeneration in addition to *ex vivo* spheroid production for liver cells.[50,54,108–112] These scaffolds have been made from materials such as poly(2-hydroxyethyl methacrylate) (pHEMA),

polyacryalamide hydrogels, poly(lactic-co-glycolic acid) (PLGA), chitosan, and tricalcium phosphate cement as well as combinations of various other polymer blends from assembly methods described throughout Chapter 1.2.[53,109,113,114] It has been shown that with a biocompatible material, scaffolds with this type of uniform, interconnected pore architecture, can improve vascularization and ultimately enhance tissue regeneration.[115] Various studies have explored changing both the scaffolding material and the particle size and fusion conditions to control the various pore sizes within the matrix (including surface pores, windows, and internal pores).[108,113,114,116] By altering the composition and pore structure, or form, of the scaffold, the function of the scaffold could be tailored to treat ailments ranging from filling bone defects to replacing damaged alveolar (lung) tissue. ICC's currently show great potential as regenerative therapies, yet there still lies unanswered questions regarding optimal structures for various tissue engineering challenges.[108,109] Further research into the effects that different mechanical and surface properties have on various cell types (as well as how the bioactivity and degradation profile of a material impacts cellular behavior in the tissue building process) will help to better establish inverted crystals as a translational regenerative therapy.

In the future, these types of hierarchical materials could also expand in utilization into the energy fields for applications including adsorbents, catalyst supports, electrodes for batteries, double layer capacitors, and host sites for hydrogen storage.[4,33,34,89] Specifically, porous carbon is a popular platform material for these applications due to its chemical inertness and thermal stability. As a base material for fuel cell electrodes, ICC structures offer functional benefits in the creation of high surface area, thin walls and high degrees of customizability and reproducibility. Bicontinuous structures of this sort provide an open, continuous pore space, which is favorable for electrolyte access and continuous walls, which aid in the conduction of electrons and ions. By

creating structures with large surface availability, there are more sites for charge transfer across the electrolyte/electrode interface, potentially creating a more efficient electrode material.[4,34,89]

While a great deal of research has been devoted to applications of inverted crystals based on Brownian particles, the use of such crystals produced from non-Brownian particles is still in its infancy. Nevertheless, using non-Brownian particles as a template for creating new ICC-based hierarchical materials may provide enhanced structural functionality, larger pores for mass transport and greater surface availability than seen in current technologies.[4,34]

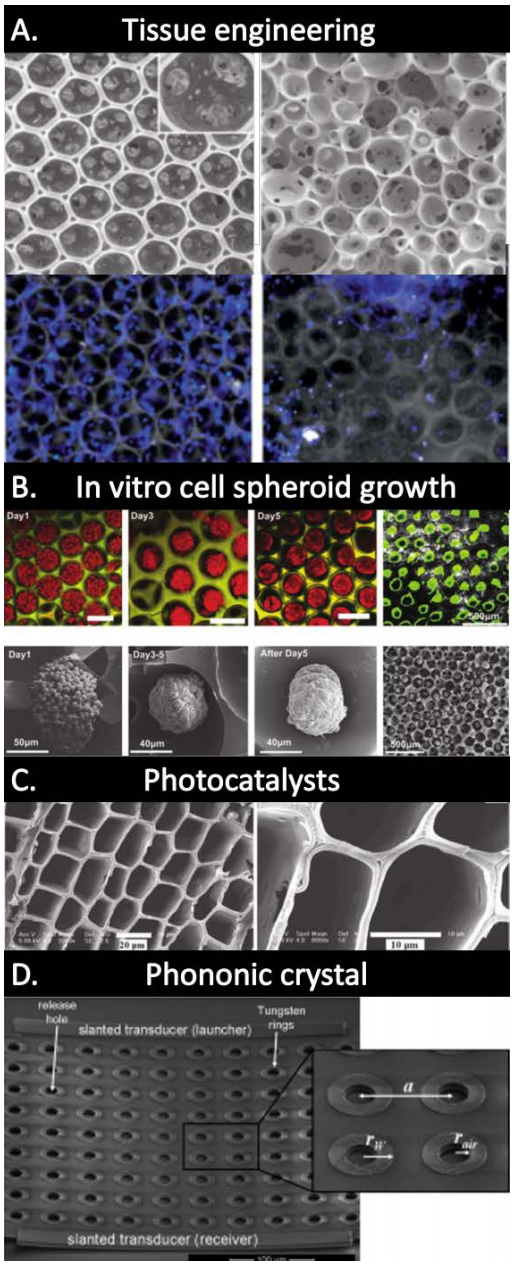

Figure 4: Examples of using macro-features to enhance the function of materials ranging with application from tissue engineering to phononics. A) Tissue engineering scaffold produced from PLGA. The SEM and fluorescence micrographs illustrate scaffold organization and interconnectivity with fibroblast (DAPI staining) penetration through the organized ICC scaffold (pore size = 211 μm) on the left hand side in a better way than the un-organized scaffold on the right hand side.[117] B) ICC scaffolds used to produce cell spheroids ex vivo. [110] C) Cedar wood coated in TiO_2 for photocatalysis. [118] D) SEM of a W-in-SiO_2 phononic crystal. [119]

2.0 NON-BROWNIAN PARTICLE SELF-ASSEMBLY AND METHODS FOR INDUCING SELF-ASSEMBLY IN TWO AND THREE DIMENSIONS

This chapter is adapted from: M. H. Lash, M. V Fedorchak, S. R. Little, and J. J. McCarthy, *Langmuir*, 2015, **31**, 898–905.

2.1 INTRODUCTION

As discussed in Chapter 1, external agitation is seen to substantially influence non-Brownian particle behavior. This Chapter in particular explores the use of sonication energy as an agitation source to overcome kinetic entrapment and induce crystallization among non-Brownian microparticles. The process of induced crystallization described herein produces particle-based crystals, defined as two- or three- dimensional ordered arrays of monodisperse spherical particles.[120] The long range order and reproducible hexagonal close packing (HCP) of these crystals make them a particularly interesting class of functional materials with applications in chemical sensing, optics, and biomedicine, as discussed in Chapter 1.[102,120,121]

A great deal of research has been done to examine the fundamental interactions driving self-assembly behavior on the atomic, molecular, and nano- scales. Brownian motion drives much of this behavior as a result of the natural thermal energy that exists within the system.[32,122–124] The atoms/molecules/particles consistently travel throughout their environment, gaining the ability to freely adjust their position until a stable configuration is achieved (which theoretically occurs

prior to kinetic arrest, locking them into a given configuration).[37] A balance between long-range attraction and short-range repulsion forces must be achieved during self-assembly to bring components together (to minimize free energy) and trap them in this configuration.[125]

Simple scaling arguments can be used to gauge the potential efficacy of thermal motion for driving particle crystallization. Consider the time it takes for a particle to move a distance equal to its own diameter due to Brownian motion alone, or the relaxation time, which is written as

$$\tau_R = \frac{\pi \eta R^3}{k_B T} \quad (1)$$

where k_B is the Boltzmann constant, T is temperature, R is particle radius, and η is viscosity. Based on this expression, a 1 μm polystyrene (PS) particle will move a distance equal to its diameter in ~1 s while a 100 μm particle will move its diameter in ~100 Ms. In terms of total distance traveled, for a 1μm particle to move 100 μm it would still take three orders of magnitude less time (10^3 s) than it does for a 100 μm particle to move that same distance.[126] Thus, for sufficiently small particles, Brownian motion can serve as a means of both macroscopic and microscopic motion, but has a relatively negligible impact on sufficiently large particles on an experimentally-relevant time scale. Equation 1 is an over estimate for the potential distance the particle can move due to Brownian motion. As the particles hit a wall or substrate surface, energy is dissipated. Additionally, in the near-substrate environment the drag force will be larger than what is shown here. Nevertheless, including the near-wall correction does not qualitatively change our argument.[127] Methods such as spin coating[128,129] and vertical,[130] horizontal[131], and Langmuir-Blodgett deposition[132,133], as well as continuous convective assembly[134,135] can be employed based on the particle/solvent combination and desired application to synthetically fabricate colloidal crystals from nanoparticles in a fluid. These processes generally create a thermodynamically stable, HCP arrangement wherein the free energy between the particles is

minimized. At the sub-micron and nanoscale, the underlying thermal effects naturally overcome other phenomenological barriers that lead to metastable configurations and a variety of particle assembly techniques are viable based on gravitational, electrostatic, and capillary-driven assembly methods, as well as physical confinement and shear flow. For example, Denkov *et al.*[135] theoretically discussed and Malaquin *et al.*[136] experimentally showed that convective and attractive capillary forces can act as the driving force for particle assembly (from colloids in suspension). In the experiments of Malaquin et al., convective assembly on a hydrophilic substrate drives 2D particle assembly once the solvent layer's thickness became equal to the particle diameter. As the contact angle between the substrate and fluid increases, attractive capillary forces dominate in the particle assembly.[135,136]

Methods to assemble non-Brownian microparticles (10 μm<d<1000 μm) have historically been more expensive and laborious.[65,137,138], in part due to rapid sedimentation rates of large particles.[42] Liu *et al.*[47] manipulate the environment to make use of fluidic forces and solvent evaporation, allowing the particles more time to interact prior to kinetic arrest in order to form 3D crystals. Zhang *et al.*[49] and Lee *et al.*[110] also took advantage of a slow evaporation rate and exposed a variety of sizes of microparticles to gentle agitation in a step-wise fashion to induce organized close packing over time.[49,110] Tang *et al.*[45] imposed an external magnetic field as a template for self-assembly at a liquid-liquid interface to arrange non-Brownian microparticles over the course of days. In these works, the crystal formed over multiple days within a confined geometry by balancing particle/solvent densities (buoyancies) and solvent evaporation rates.[45,49,110] Conversely, methods proposed by Choi *et al.*[42] report crystallization occurring on a time-scale on the order of minutes, not including the time necessary for solvent evaporation. At yet larger scales (i.e. the millimeter-scale), particle assembly has still been reported via a more

limited slate of techniques. For example, 3D close-packed crystals can be made within a confined geometry by manipulating the amplitude and frequency of 3D vibrations,[65] or by pick-and-place techniques.[139]

The objective of this research is to adapt particle assembly techniques currently used in the nano and sub-micron regime to larger particle systems. In particular, we explore the impact of externally imposed vibration/agitation (to enhance component mobility and structural adjustability) on the assembly behavior of non-Brownian microparticles (10 μm<d<1 mm).[26,46,140] In this work we vary the agitation input using a sonication bath, sonication probe and shaker plate to study crystal formation behavior for particles ranging from nano- dimensions up through the sub-millimeter dimensions on a time scale on the order of minutes. Additionally we briefly explore the impact of particle surface charge on the organization process. While other groups have reported successfully using ultrasonic agitation and shaking to induce particle close packing in 3D, [40,52,139–142] here we systematically explore the required assembly conditions as well as propose a sedimentation-driven methodology for fabrication of two and three dimensional crystals in a single step with rapid assembly times that can be used for both Brownian and non-Brownian particles. Moreover, we evaluate a host of simple characterization assessment tools for evaluating the degree of packing and organization of these macro- crystals. We find that this analysis provides both qualitative and quantitative indications of crystal packing and focus on the sonication bath as our energy input source.

2.2 MATERIALS AND METHODS

In the following, we experimentally assess the process of introducing ultrasonic agitation to polystyrene microparticles of different sizes and analyze the particle packing within the resulting structures. We also seek to explain how ultrasonic waves can be used to transport non-Brownian microparticles and induce HCP packing on the surface of a flat substrate.

2.2.1 Characterization of particle/fluid motion and behavior

Agitation was added through a variety of methods including a shaker plate (RotoMix 50800, Barnstead Thermolyne, St. Louis, MO), a sonication probe (Vibra-Cell, Newton, CT), and a sonication bath (Branson Ultrasonics, Danbury, CT). A variable autotransformer (Staco Energy Products Co., Knoxville TN) and uninterruptable power supply (Tripplite, Chicago, IL) system were connected to the sonication bath to consistently control the power input to the bath. Particle motion was observed and recorded for structures formed using all forms of agitation and those that experienced no agitation. For sonication bath prepared samples, an Olympus SZX10 Stereomicroscope (Olympus Corp. Hamburg, Germany) was used to take images every 1-3 seconds. These image series were collected for particles ≥100 μm due to the limitation of the microscope zoom/focus. Fluid motion was observed by depositing a minute amount of Rose Bengal dye (Acros Organics, New Jersey, USA) into 40 μL of deionized water (DIW) on a glass coverslip and images were taken every 7 seconds. After 14 seconds, the bath was turned on at full capacity and images were taken every 7 seconds. The diffusion process was observed with no sonication as well as with the sonication bath and probe at varying energy levels. Additionally, the motion of a particle undergoing agitation from the sonication bath was observed by placing

different particle populations ranging in size from 750 μm to 2.5 mm in diameter (d) and in density from 1.05 g/cm^3 to 3.68 g/cm^3 on top of a flat-bottomed petri dish within the sonication bath, and their projectile motion was observed as the bath was turned on (Figure 5). As the power settings on the bath were adjusted from 42-100%, the resultant particle behavior (i.e., whether the particle remained on surface or was elevated) was recorded for 10 independent particle trials.

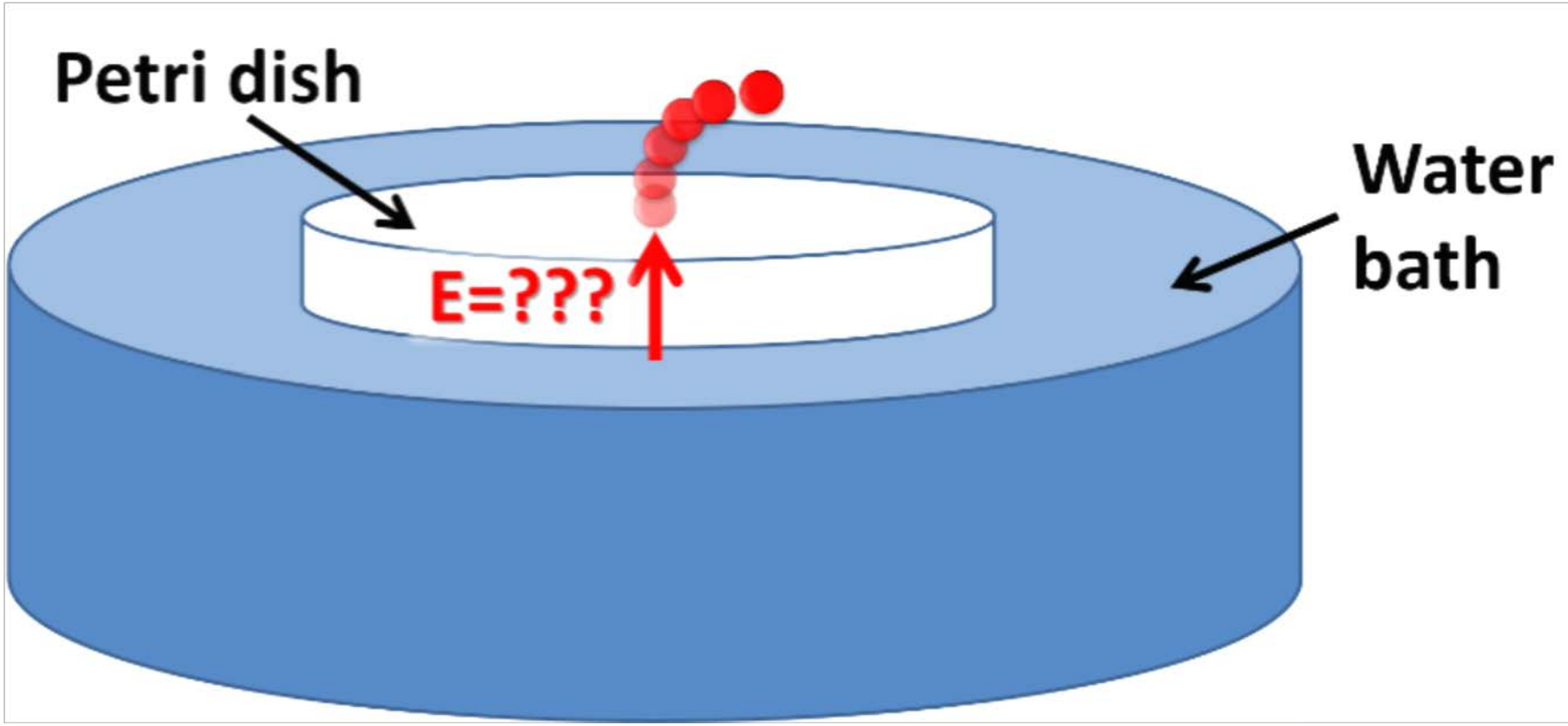

Figure 5: Particles ranging in size from 750 µm to 2.5 mm in diameter and ranging in density from 1.05 g/cm^3 to 3.68 g/cm^3 were placed in a petri dish in the sonication bath. The bath was turned on at various settings ranging from 42% to 100% of the maximum bath sonication force input (128 µN) and whether the particle jumped off of the surface was recorded. This was done with a minimum of ten particles for each particle population per power setting.

2.2.2 HCP crystal formation

Glass cover slips were washed with Piranha solution (3:1 sulfuric acid:hydrogen peroxide, Fisher Scientific) to ensure a uniformly clean surface with low surface tension (contact angle of 10±3°). Particle crystals were prepared on the surface of Piranha washed glass cover slips to create two-dimensional crystals. Samples were prepared by depositing particles in solution onto a cover slip in a plastic petri dish on top of a 1300 mL water bath. The particle solutions were made as 10% weight/weight (w/w) in DIW to produce monolayers. Polystyrene (PS) particles (d≤18 μm from Bangs labs, Fishers, IN; d>18 μm from Phosphorex Inc., Hopkinton, MA) were used. For the sonication bath, a variable autotransformer was used to tune the voltage powering the sonication bath and was experimentally used at 0%, 60%, 80% and 100% in this study and the resulting structures were compared as a function of the external agitation input.

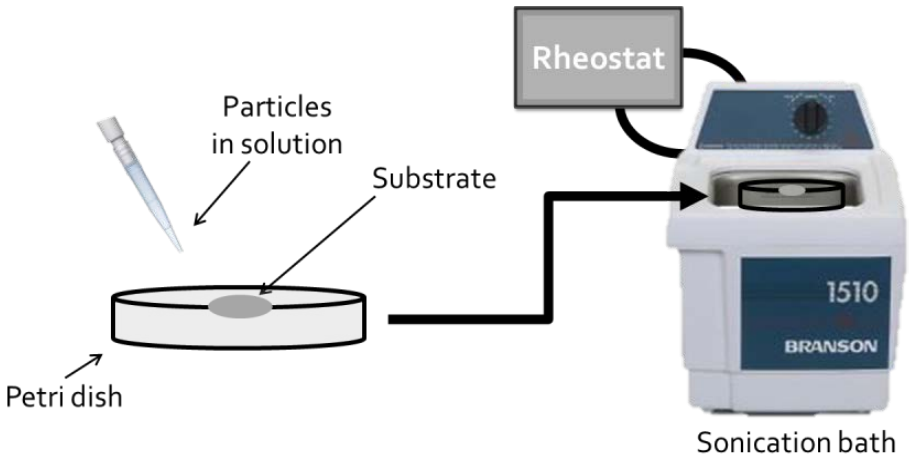

Figure 6: Fabrication process for producing crystals using a sonication bath, illustrating particles in solution being deposited onto a substrate where ultrasonic energy is introduced. The autotransformer is not necessary for production but allows for variations in the input energy.

2.2.3 Characterization of crystalline packing

The quality of crystals formed was observed using a JEOL scanning electron microscope (SEM), a Nikon Ti-U inverted light microscope, and an Olympus SZX10. For SEM imaging, crystals on glass coverslips were sputter-coated to a thickness of 5 nm. Images from the Nikon light microscope were acquired using NIS Elements software and analyzed using a Hough transform implemented in MATLAB. SEM images were also used for extracting particle position information in MATLAB. Particle position coordinates were identified and the distances between particle centers for a given particle and its nearest neighbors within a customizable cutoff distance was measured. The cutoff distance was chosen to be 1.4*diameter (as in Besseling *et al*.).[143]

2.3 RESULTS AND DISCUSSION

In this study we analyze the behavior of 6 µm, 18 µm, and 100 µm PS particles submerged in a medium of DIW where the fluid medium is used to circulate the particles and reduce friction and adhesion forces on them. We compare particle behavior in an unagitated system to that resulting from ultrasonic agitation supplied by either a sonication bath or a sonication probe; however, the majority of analysis focuses on the sonication bath due to greater reproducibility of results and higher quality crystals resulting. Additional data is in Appendix A.

2.3.1 Characterization of particle/fluid motion and behavior

The movement of particles within their surrounding fluid is enhanced by convection due to cavitation within the fluid. It has been shown that the waves created during iterative cavitation bubble formation/implosion cycles increases convection within a fluid.[137,144–147] Acoustic cavitation bubbles are produced by the sonication bath and are transferred from the water bath into the fluid surrounding the particles. The convective motion tendencies visualized in Figure 7 support the particle packing tendencies observed in Figure 9. Observing the behaviour of a dye (Rose Bengal) in water (Figure 7) suggests drastically increased macroscopic fluid motion when the sonication bath was active versus when no agitation was added. In terms of particle motion, these results suggest that the sonication bath creates convective fluidic motion that may encourage both macroscopic particle motion as well as inter-particle collisions.

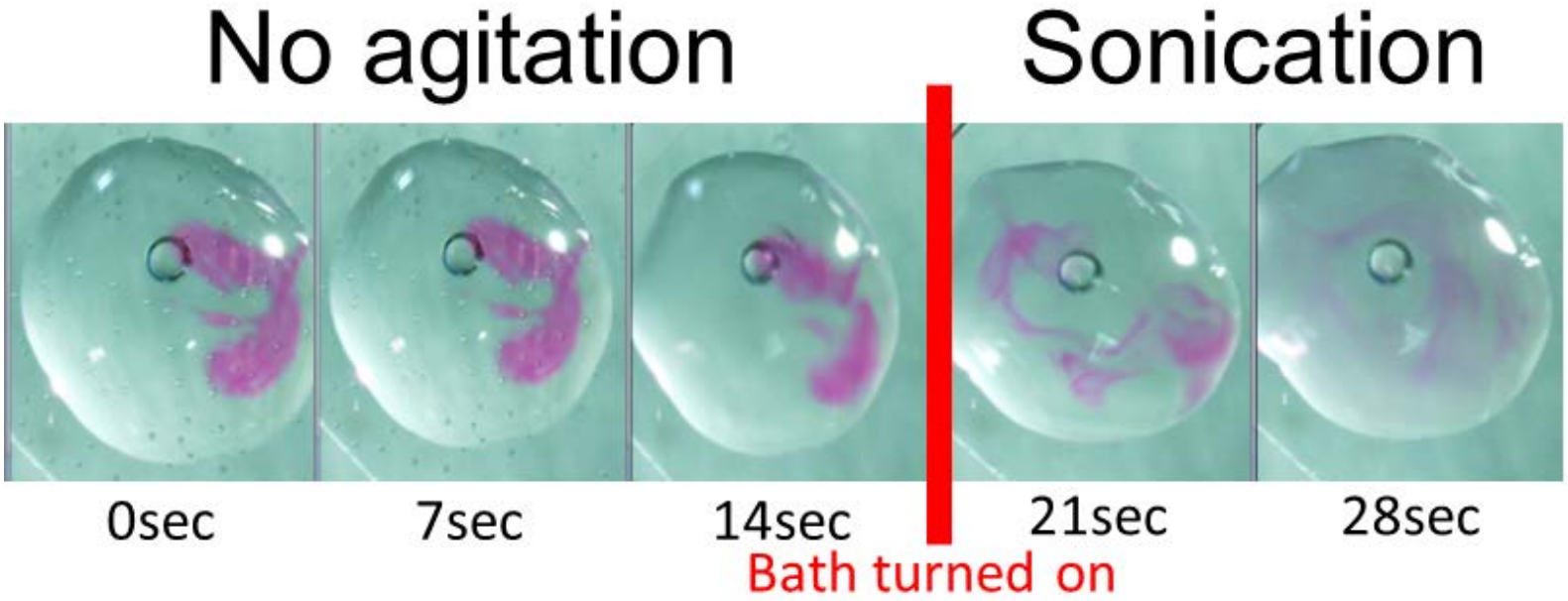

Figure 7: A series of snapshots were taken at even time increments to visually compare fluid motion before and after sonication-based agitation is added via sonication bath.

In addition to the fluid medium's influence on a particle's motion, we investigated how the energy from the sonication bath affects a dry, lone particle as a metric for analyzing the energy input to a particle while in the sonication bath. Here, we studied the conditions necessary to lift a particle off of a plastic substrate (petri dish) as a means of measuring the force exerted by the bath on the particles as a function of the input voltage. This study (with completely dry particles) represents an upper bound for the expected energy input (or force) as viscous dissipation within the fluid will mitigate the energy input in the presence of the submersing fluid. Figure 8 depicts the apparent trends when particles of mixed dimensions and densities are observed. This chart represents all of the trials performed while varying both the mass of a given particle as well as the input voltage to the sonicator. The trend line represents the lowest energy level that would cause a given particle mass to jump. Both the filled and open circles on the graph represent real data points (n=10 particles) for the particles tested in this experiment. The particles used in this test were of various compositions, including acrylic, glass and cellulose acetate. For particles made from cellulose acetate, we noticed a large degree of tribocharging such that forces due to static charge buildup disrupted the particle's motion after just a few seconds of contact (between the particle and the substrate.) Additionally, Figure 8B shows the relationship between the input sonication voltage and the sonication force that must overcome the gravitational force to move a particle(s). As the rheostat is used to adjust the power input to the bath, the single piezoelectric transducer maintains ultrasonic frequency at 40 kHz due to the internal oscillatory frequency sweep control system, and we yielded roughly a 70% energy efficiency (D. Galius, Branson Ultrasonics, personal communication, June 25, 2015). Our observations and data suggest that the force imparted from the sound waves varies linearly with the rheostat setting. This is consistent with a linear variation in sonication amplitude (at a fixed frequency). Thus, we expect that the sonication energy will vary

non-linearly with the rheostat setting (as the energy has a quadratic relationship with the sonication amplitude).

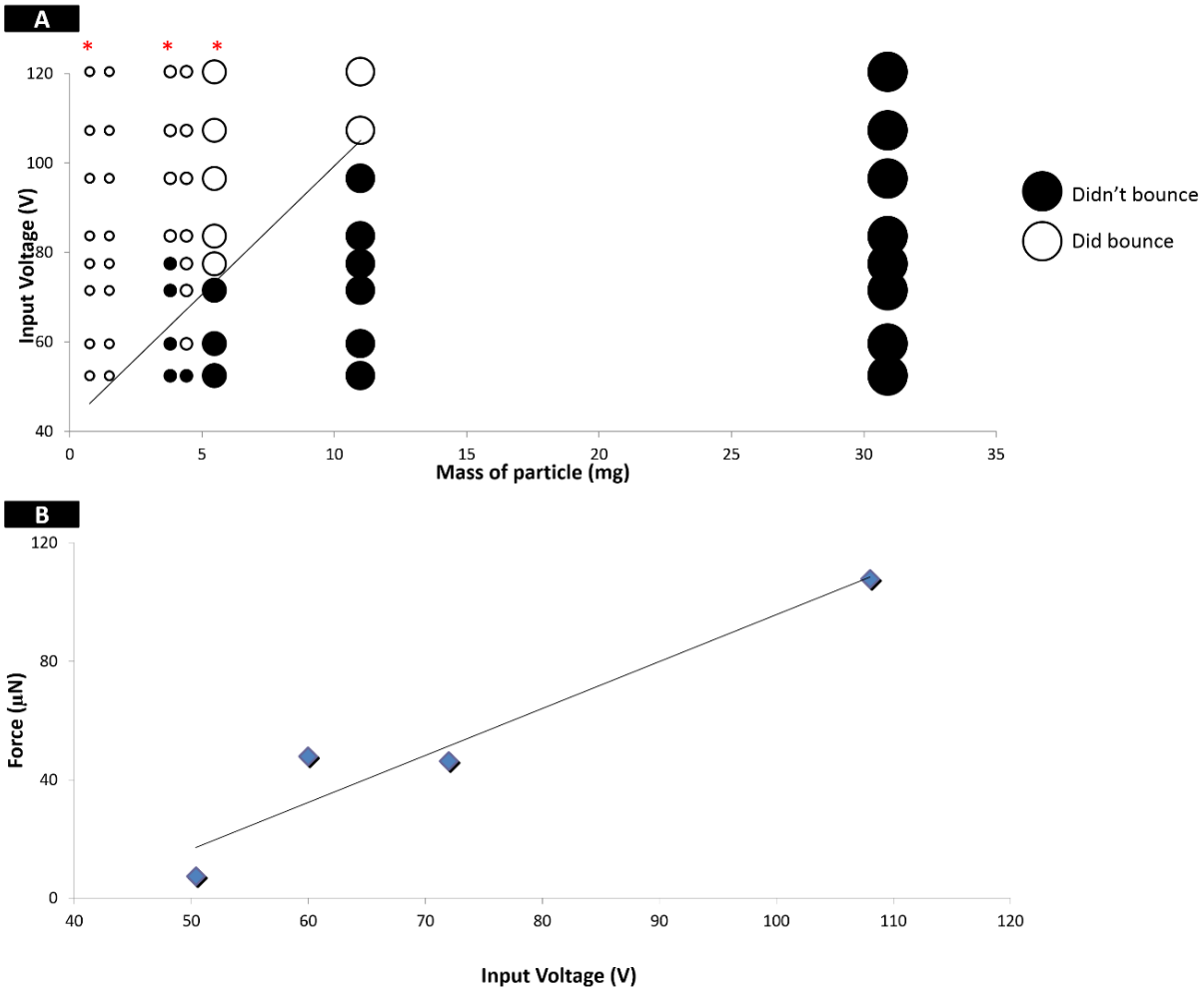

Figure 8: A) Input voltage to sonication bath versus mass of particle. Each circle on graph represents a particle population (number of particles=10) that was tested at that energy level and whether particles in that population were ejected off of the substrate or not. The trend line was drawn among data points for the greatest mass of particle that would jump at a given energy level. Note: columns with red stars represent those particles (cellulose acetate) with a large degree of tribocharging. B) Correlation between the input voltage to the sonication bath and the force translated from that input.

From a combined analysis of the fluid medium alone and particles alone, the effects of sonication input energy suggests that, based on the particle size and mass, there is sufficient energy input to move the particles both macroscopically (for the purpose of concentration) as well as microscopically (for crystal rearrangement and "annealing"). This idea will be further investigated in terms of crystallization in Chapter 2.3.2.

2.3.2 Characterization of crystalline packing

Structures formed via solvent evaporation (no external agitation) for particles ranging from 200 nm to 750 μm in diameter showed drastically different crystallization behavior compared to those particles experiencing agitation. Elwenspoek *et al*.[148] have previously shown that for particles in the vicinity of 5 μm, buoyant forces and gravitational forces do not dramatically impact particle behavior, therefore natural thermalization dictates particle movement and self-assembly. Consistent with these prior results, we observed HCP structures formed naturally through evaporation/sedimentation for particles that are 6 μm in diameter and smaller. Presumably, natural forces such as solvent evaporation and surface tension along with some thermalizing effects are strong enough to move the smaller particles into a crystalline configuration. However, we do not observe natural formation of HCP crystals when employing particles larger than 6 μm (0 μN column in Figure 9). As the particle size increases, susceptibility to thermalization on an experimentally-relevant time scale decreases. From this apparent lack of macroscopic motion, the particles do not experience the collisions/interactions necessary for an HCP structure to develop prior to fluid evaporation and particle immobilization.

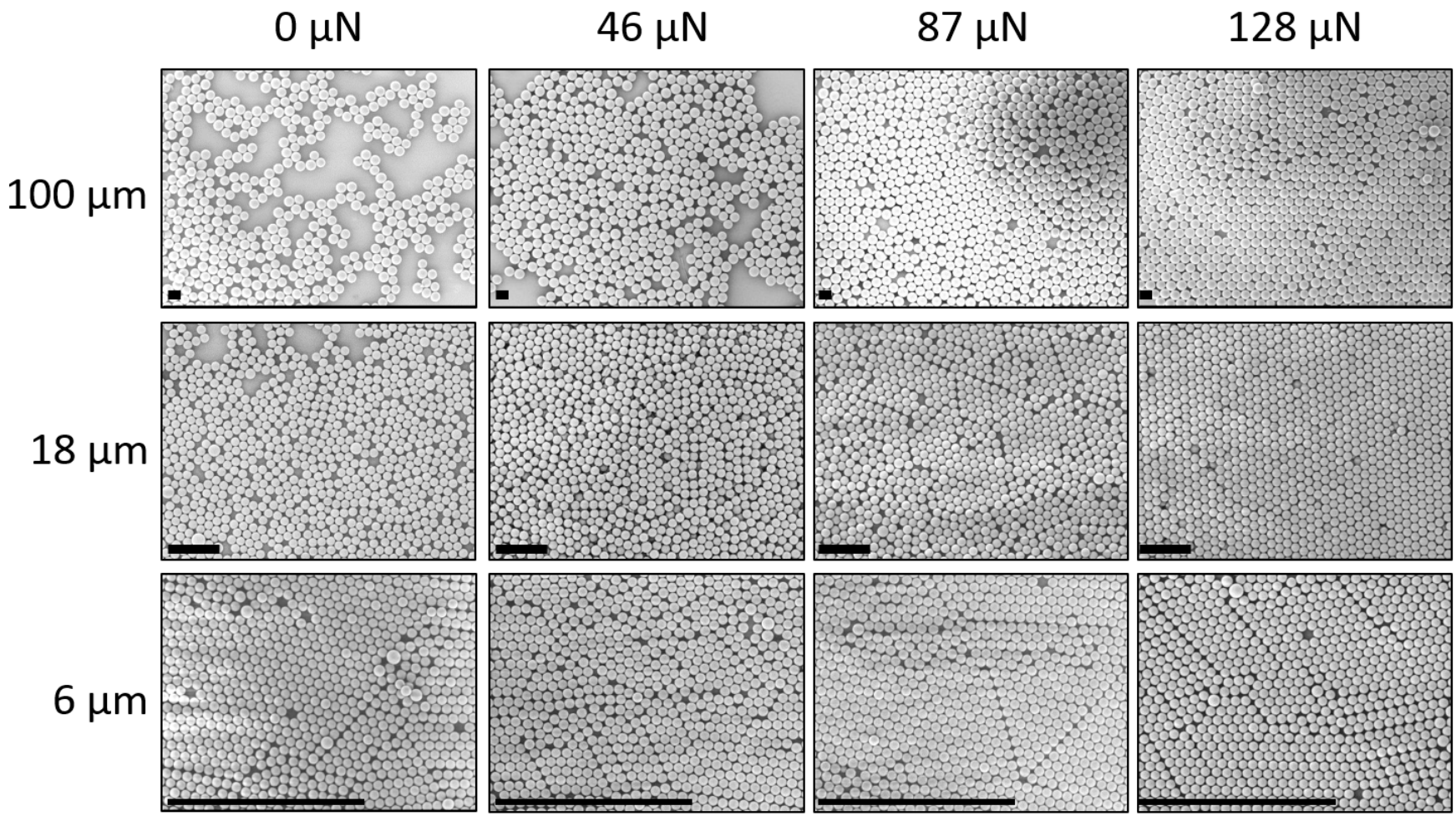

Figure 9: Direct comparison of structures formed as a function of ultrasonic agitation from a sonication bath (labeled in terms of input sonication force and particle diameter). All scale bars are 100 µm.

Figure 10 depicts the relationship between particle size and the ultrasonic energy input used to induce close packing among particles as described through a packing fraction and interparticle angle homogeneity. Figure 10A shows a 2D packing fraction relative to ideal HCP packing, with 100% indicating a near-ideal two-dimensional HCP packing fraction of 0.906.[149] Regardless of the input energy, 6 μm PS pack with an average packing fraction of 0.873, or the average sample was 96% packed when compared to an ideal configuration. Such a high degree of packing uniformity among Brownian particles is supported by observations in the literature, where sonication has been shown to decrease defects and grain boundaries for Brownian assemblies due to enhanced motion among the particles.[40] For 18 μm PS the sonication bath increased the packing density of the particles compared to evaporation alone in an increasing fashion as the input energy increased. For 100 μm particles, we observed a growing trend in the quality of packing as the intensity of sonication energy increased. This particular metric, however, can be misleading in the case where the particles are densely packed yet arranged in a random orientation (for example in non-ordered aggregates).

To overcome the measurement limitation associated with packing fractions, we evaluated the angle between particles, essentially inspecting an individual particle's placement in relation to its neighbors as a more discriminating order parameter. The gross positioning of each particle in relation to its neighbors is described by calculating the angle between particle centers. Figure 10B shows the average deviation in the angle from an ideal 60° angle of an HCP crystal (measurement includes edges of crystal grains and particles that are not fully coordinated). The quantification of angle deviation suggests that as the input energy to the sonication bath increases, the consistency and organization of the close packed structures for all particle sizes also increases. Conversely, in

the absence of agitation, the deviation in particle packing and positioning increases as the particle size increases.

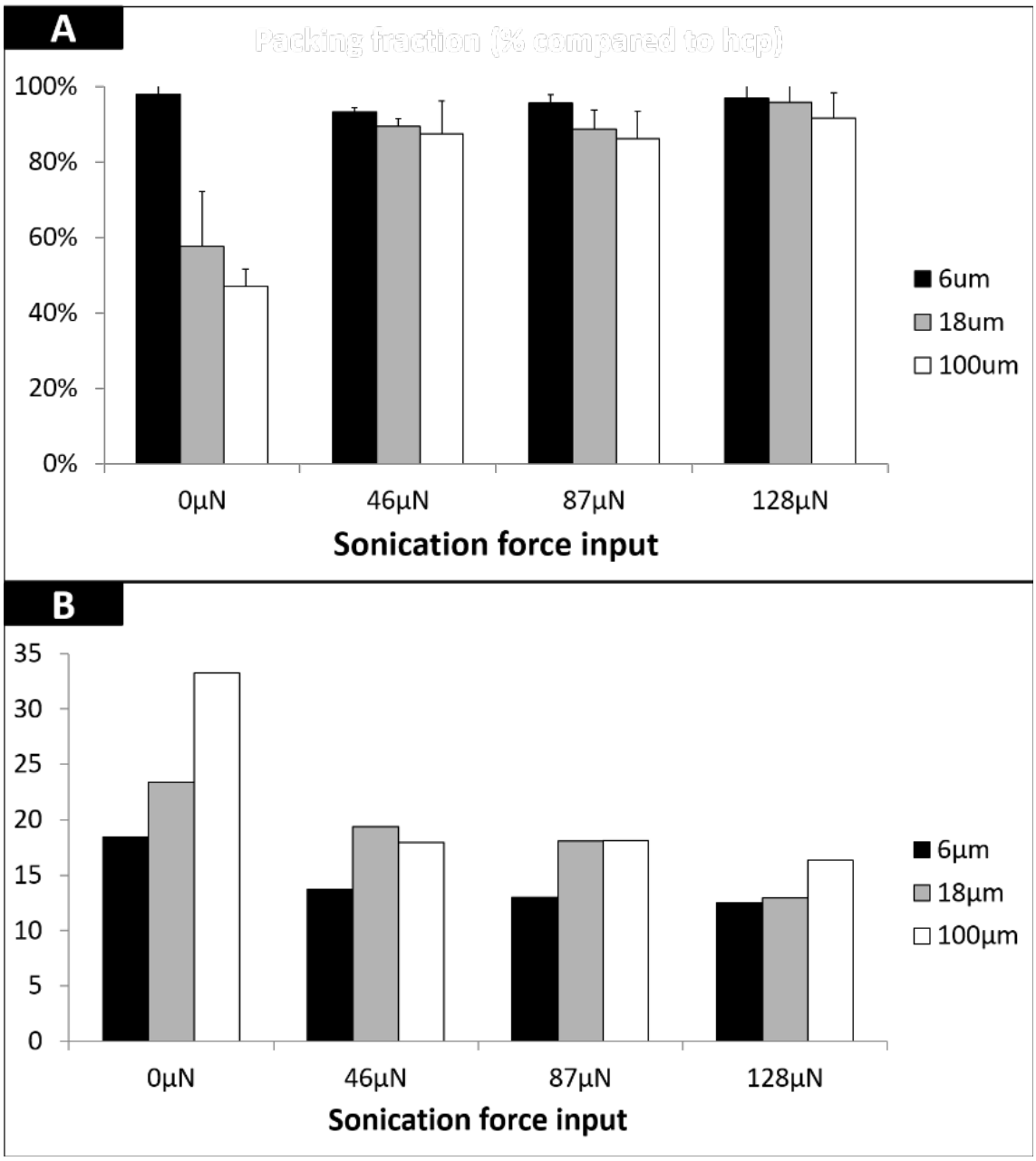

Figure 10: A) Ratio of particle occupied to unoccupied area based on different particle sizes and preparation methods. B) Deviation in calculated angles between particles for a packed structure compared to the ideal HCP packing angle. An ideal HCP crystal has interparticle angles of 60^0. Large discrepancies from the ideal value often occur when a particle has fewer than six neighbors.

Additionally, Figure 11A shows another alternative characterization tool where we plot the percentage of particles that may be considered to be within a crystal grain as a function of particle size and input energy. These calculations are centered upon an analysis of individual particles (based on real position coordinates extracted from Figure 9, among others). As discussed in Chapter 2.2.3, we define a particle's neighbor to be any other particle within a 1.4*d cutoff distance. We then classify each particle as being within a crystal (yellow), on a crystal boundary (red), or not in a crystal (gray). Specifically, the red particles are fully coordinated (i.e., they have six nearest neighbors), while the yellow particles are not only fully coordinated, but also all of their neighbors are fully coordinated (i.e. they are contained within a crystal grain). The grey particles are not fully coordinated and therefore, are not considered to be part of the crystal. Figure 11B shows an example of this classification based on the experimental results from Figure 9. This newly proposed metric has the advantage of being relatively simple in its calculation, while simultaneously exhibiting the ability to distinguish between differing highly ordered crystalline structures. We should note that although this metric is particularly sensitive to point defects or vacancies, it is less sensitive to line defects.

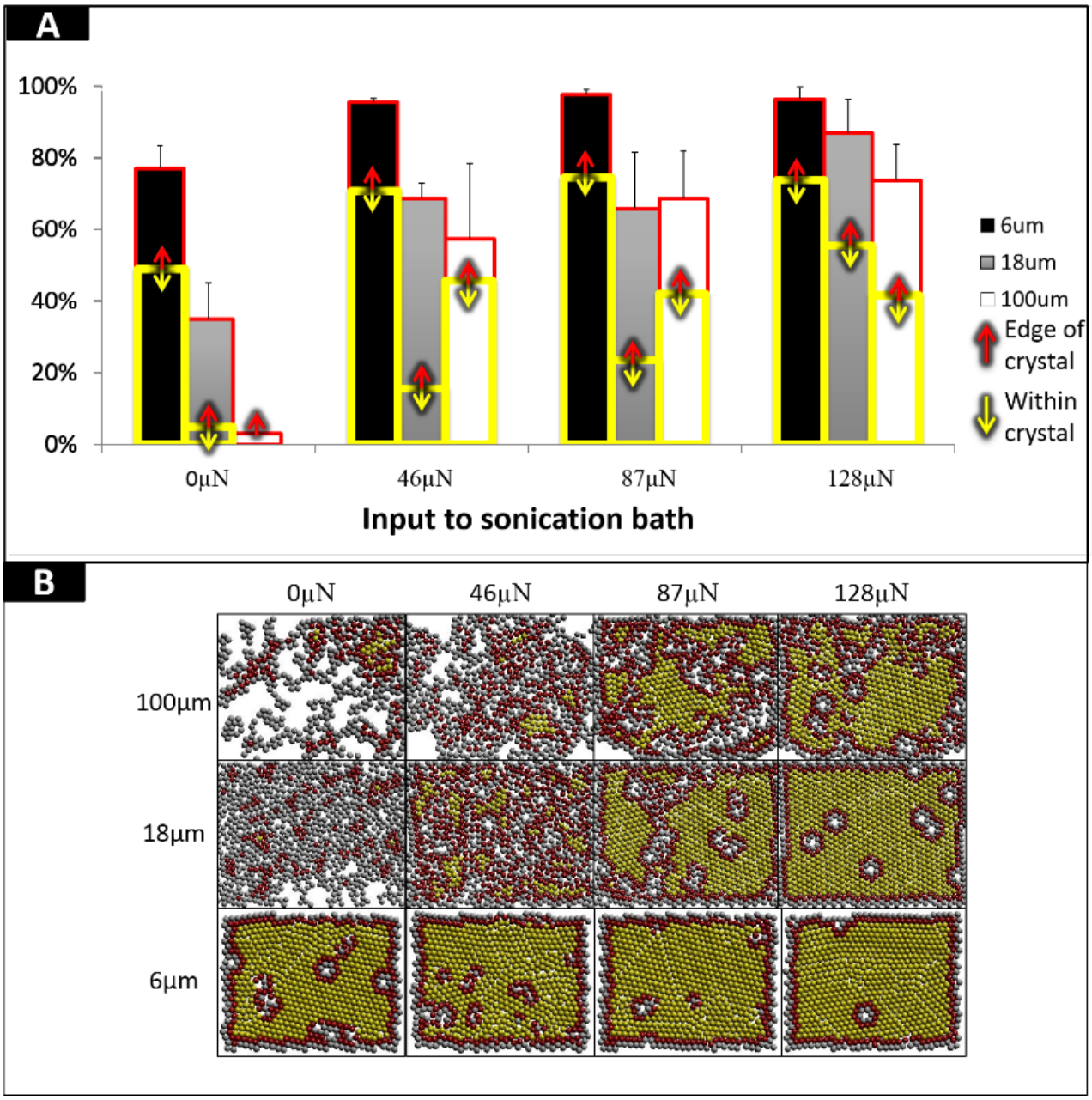

Figure 11: A) Percentage of particles that lie within a crystal grain. The histogram depicts the percentage of red plus yellow particles seen in (B) out of the total number of particles per image. Histogram shows average over six separate crystalline samples. B) Color coded depiction of crystal grain determined by how many neighbors a given particle has within a 1.4*diameter cutoff distance. Yellow particles are fully coordinated and all of their neighbors are fully coordinated. Red particles are fully coordinated but all of their neighbors are not. Grey particles are not fully coordinated and are not part of a crystal grain.

The data shown in Figures 10 and 11 suggests that the sonication bath at the highest voltage/force setting (120 V/128 µN) produces the most consistent HCP structures for all particle sizes tested. As the energy supplied to the bath was tuned down to 80% (96 V/87 µN) and 60% (72 V/46 µN) of its maximum capacity, the resulting energy transferred from the bath to the particles was decreased, leading to a reduced regularity in the structures formed. The influence of the ultrasonic energy had the greatest impact on the 100 µm particles as it both induced motion, as well as promoted crystal annealing (microscopic plus macroscopic motion). Conversely, for 6 µm particles that naturally packed into HCP crystals (natural Brownian forces are still greater than gravity in this regime), the addition of ultrasonic energy simply decreased the presence of defects within the crystal.

2.3.3 Discussion of packing mechanism

In many previous studies of 2D particle assembly, capillary forces provide a strong driving force for particle organization.[135,136,150,151] In contrast, the vast majority of the particle rearrangement in this work occurs while the particles are fully submerged in fluid, thus the rearrangement cannot be driven by capillary forces. Figure 12 depicts the crystallization process via a sonication bath to enhance particle motion and crystal homogeneity over time. Note that the density of the 2D crystal increases significantly despite the fact that the particles remain submerged. In fact, the only image in this sequence where there is complete fluid evaporation is the final time point. We further explore the dependence of sonication fluid on particle clustering in Chapter 8.1.2 (Figure 36).

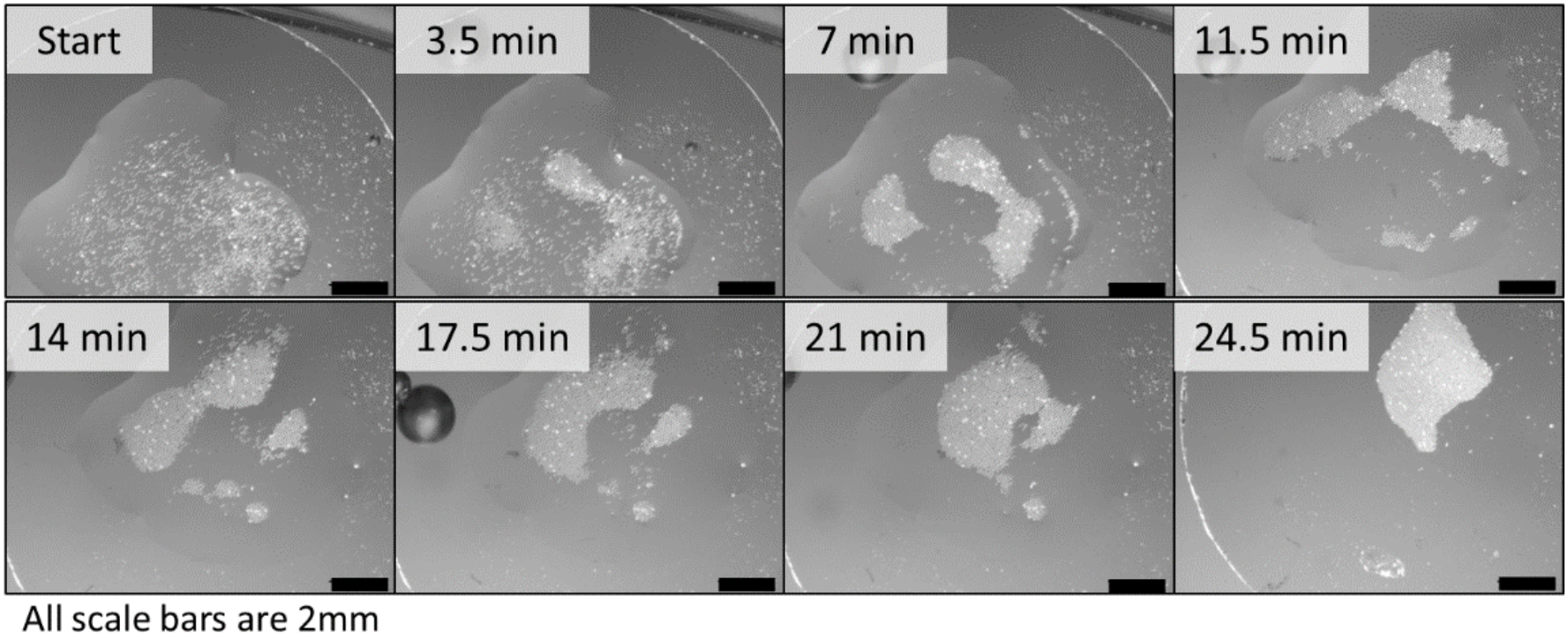

Figure 12: Images taken over ~25 minutes. Time sequence records the motion of 100 µm PS particles submerged in deionized water moving due to ultrasonic waves produced in a Branson sonication bath. The particle-level organization in the last image can be compared to that seen in Figure 9 for 100 µm particle under 128 µN of force, or at 100% sonication. Note: Bubble seen in various images is located in the water bath below the sample and is not in direct contact with the particles or their surrounding fluid.

As discussed in Chapter 2.3.1, the ultrasonic energy input to the fluid-particle system is sufficient to accomplish two things: (1) cause macroscopic fluid motion, and (2) overcome gravitational affects even for "large" particles (see Figures 8 and 9). Using the energy estimates attained from Figure 8, we can show that sonication imparts sufficient energy to advect particles at their terminal velocity within the fluid. Taking a 100 μm particle as an example, scaling arguments show that the interparticle forces estimated from DLVO theory (taking a particle surface energy of roughly 1.0×10^{-6} J/m^2) are too small to overcome this macroscopic motion beyond an interparticle separation distance of approximately 3 nm (which is comparable or even smaller than the presumed particle surface roughness). Thus, we expect that another mechanism of particle clustering is at play, at least in the early stages of assembly. We believe that the crystallization behavior seen in Figure 12 is driven by a mechanism that is similar to what is called "inelastic collapse" in granular materials.[63] Inelastic collapse occurs when particles cluster due to a spike in the energy dissipation rate and can be understood to occur in our system as follows:

- When the particles are isolated, they move at a (roughly randomly-oriented) velocity where the energy from the sonication bath is balanced with the viscous dissipation due to drag on the particles by the fluid and their proximity to the substrate.

- When the interparticle distance becomes small (due to random encounters, for example), lubrication forces between particles causes increased drag, thus dissipating more energy and reducing the relative velocity of those particles. This "cluster seed" then increases the probability of additional "near miss" encounters with other particles due to the seed's increased size. Thus, the energy dissipation rate grows rapidly as the collision probability continues to grow until a fully aggregated state is achieved among the particles.

Our larger particles behave essentially as hard spheres, thus they tend to crystallize once the local volume fraction exceeds a critical value (volume fraction >0.45).[152] Accordingly, the addition of external agitation via sonication supplies first the energy for macroscopic particle motion, leading to local clustering, and then the energy to allow defect annealing once a crystal is formed. Further exploration of this theory resides in Chapter 8.1.2, where the collapse and clustering of particles in an extreme excess of solvent (tested in water and glycerol for varying viscosity effects) occurs regardless of confinement and evaporation, further emphasizing the impact of lubrication forces in the overall particle packing/clustering mechanism. Additionally, the effects of surface charge and composition of the particles (provided they are monodispersed hard spheres) appear to be negligible in their impact on particle organization. We observed comparable clustering behavior and overall packing behavior with polystyrene (with and without negatively charged carboxyl surface functionalization) and soda lime particles in a variety of sonication fluids (deionized water (with and without sugars and salts), ethanol, glycerol, corn syrup, and organic solvents (DMSO, DCM, DMF etc.)). These results suggest that our clustering findings are robust to changes in particle bulk composition, particle surface treatment, suspending solvent, and solvent ionic strength. Theoretically, DLVO theory predicts that charged particles in fluid exhibit either attractive or repulsive forces when the interparticle interaction distance becomes very small. For non-colloidal particles, the influence of the double layers are generally relatively small compared with the particle radius and the particle weight becomes increasingly influential in comparison.[39,140,153] In the case of our research, we observed that in the presence of ultrasonic agitation, the particle weight and particle-environment interactions (ie presence of a template) overcame the net repulsive forces (derived from particle-particle and particle-fluid interactions) allowing for small interparticle separation distances to develop, where attractive

forces dominate and promote particles annealing. Evidence of this type of annealing behavior occurs consistently between particle of varying composition and surface charge in the production of crystals, as observed in Chapters 3-9.

Based on our energy calculations (and the ultrasound source that we use), this same behavior can be expected to be attainable for particles on the order of 1 mm in diameter. Figure 13 depicts crystal formation among both 600 nm and 750 µm PS. For both particle populations shown here, the added sonication energy helps to increase local particle motion and decrease crystal defects (and is required for macroscopic aggregation in the case of the larger particles). While, Figure 13 depicts the behavior of relatively few 750 µm PS particles, we expect that increasing the amount of particles will simply lead to larger crystal formation.

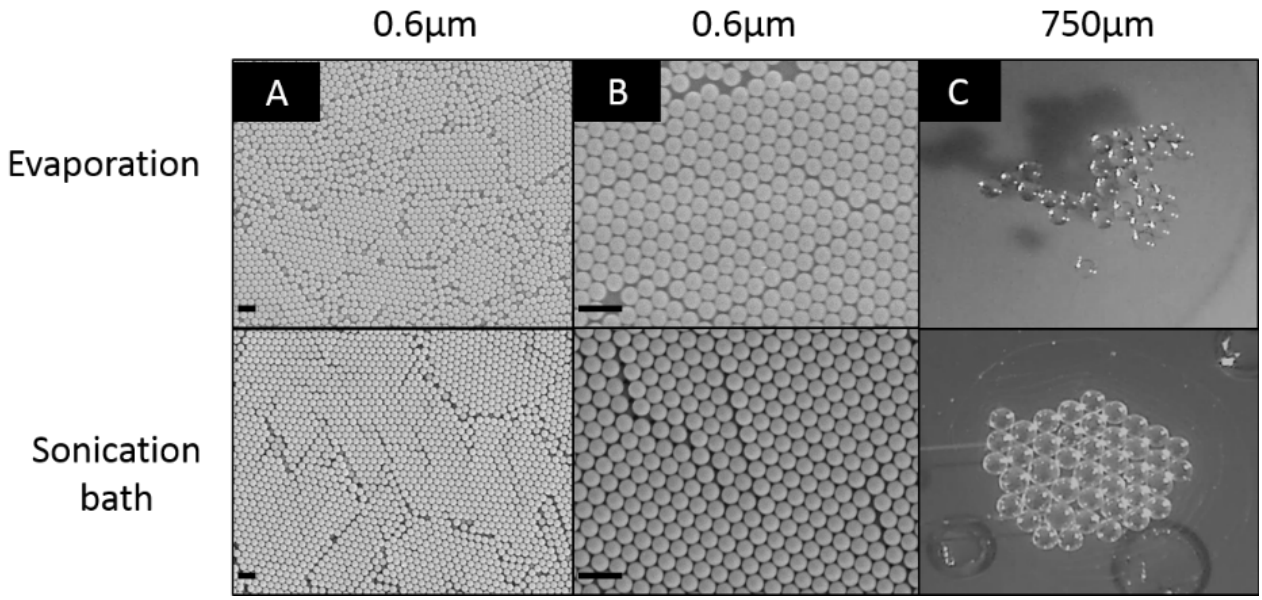

Figure 13: Images comparing self-assembly influenced by A) evaporation only (i.e., 0% sonication) and B) sonication bath (at 100% sonication) for 600 nm and 750 µm PS particles. Scale bars are 1 µm.

All of the results presented here correspond to monolayer crystals that form from a solution that is initially 10 wt%. We also looked into the nucleation process of systems with both smaller and larger the particle concentrations. Figure 14 shows a representative image where we observe a stacking effect among the particles during their assembly process. In this case we see the organization of particles around the edges on the per-level basis, giving us a high degree of confidence in the overall packing structure. When we decreased the particle concentration in water (data not shown) we observe the formation of smaller crystal nucleation sites due to fewer particles being spread over a larger area. When the local concentration of particles increases we observe HCP structure formation.

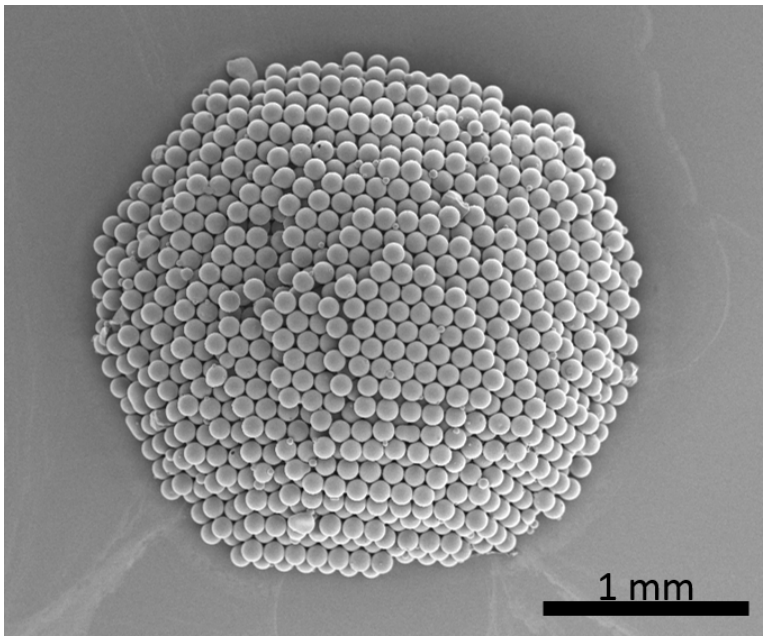

Figure 14: Three-dimensional stacking of 100 μm PS particles via sonication with a particle concentration increased above 10 wt%.

2.4 CONCLUSION

In summary, we have demonstrated a new combination of characterization methods and a more in depth analysis on how to assemble both Brownian and non-Brownian particles in a one step, time efficient method. By adding ultrasonic agitation in varying intensities, particle suspensions have been shown to move from a disordered random state to one of crystalline order (HCP crystals). We believe that these crystalline production processes and characterization methods can be extended to both larger particles and to different particle types than those presented in this paper. Additionally, as long as a high degree of monodispersity (≥95%) in particle size is maintained, the particle composition can be customized and the energy input needed for crystal packing also altered accordingly. The studies done in this paper were conducted on a relatively small scale for translation to an industrial process, but are still on a significantly larger scale than other methods published in the literature.[138] To scale up to an industrial scale process, parameters such as the size of the container or template, fluid medium, and agitation intensity would have to be adjusted appropriately.[137] The high quality HCP structures formed and studied in this work show great promise as templates with ordered and customizable pore structure either in their original form or as an inverse opal.

3.0 MULTICOMPONENT PARTICLE-BASED CRYSTALS

This chapter is adapted from: M. H. Lash, J. C. Jordan, L. C. Blevins, M. V. Fedorchak, S. R. Little, and J. J. McCarthy, *Angew. Chem. Int. Ed. Engl.*, 2015, **54**, 5854–5858.

3.1 INTRODUCTION

Although Chapter 2 focused primarily on 2- and 3-dimensional crystals of a single type of particle, more complex, hierarchical structures can theoretically be formed through those same self-assembly methods. The following Chapter describes a variety of interesting structures that can be rationally designed by agitating a collection of microparticles with ultrasonic agitation.

These structures are known as binary and higher order multicomponent colloidal crystals (bCC and mCC, respectively), which are comprised of organized arrays of particles with highly customizable architectures (feature sizes and shapes) and hierarchy. They are commonly produced on the nanoscale,[90,154] and can be produced from combinations of uniformly sized (monodispersed) particle populations of either the same or differing materials. These arrays have historically been produced by entropy-driven self-assembly of sub-micron or nano-scale particles for use in applications such as photonics (bandgap materials), chemical or biological sensing, and microelectronics where their nano-scale features enhance their functionality.[155] Nevertheless, the breadth of applications where hierarchically porous structures are useful can reach far beyond

those dependent solely on nano-scale features; however, as the diameter of the particle increases, self-assembly occurs over a much slower time scale and becomes irrelevant as a naturally-driven crystallization method.[20,25,37,156] Thus systematic fabrication of materials that span beyond the sub-micron scale has been elusive.[20,65,137] At the other end of the spectrum, for millimeter scale (and larger) particles (granular), a driving force, such as vibration, is essential to overcome the natural barriers to particle motion and arrangement.[76] In Chapter 2, we demonstrate that one can bridge this gap in materials fabrication by using ultrasonic agitation to mimic Brownian motion (or granular vibration), and induce spontaneous assembly of microspheres with dimensions ranging from the nano- to the milli-scales into hexagonally close packed (HCP) two and three dimensional crystals.[29] Herein, we extend this bottom-up assembly approach to mixed systems of particles that include a span in length-scale that is larger than any explored to date in order to attain complex hierarchical crystalline formations from binary and multicomponent particle mixtures. By doing so, we have created stoichiometric configurations of large, non-Brownian particles that resemble those formed naturally by atoms and molecules and heretofore have been reported in the literature only for nanoparticles.[91,94,157] Specifically, we examine a range of radii ratios ($\gamma_{S/L}$) and number ratios ($N_{S/L}$) of small (S) and large (L) microparticles within a mixture to explore a wide range of resulting microstructures. Additionally, through post-processing of these microstructures, we have demonstrated that it is possible to evolve these ordered arrays into binary, inverted crystalline structures with customizable, hierarchically ordered features and pore configurations that mimic those in naturally occurring porous materials (such as zeolites).

In the context of particle self-assembly, the understanding of interparticle interactions is crucial to interpreting particle phenomena.[29,125,158] Many parameters, including the particle material composition/density, size, and charge, are key contributors to such behavior, especially

in particle mixtures[157] where size mismatch has also been shown to strongly influence the resultant particle structures.[125] In fact, in hard sphere (screen-charged) mixtures of nano-scale particles, it has been observed that $\gamma_{S/L}$ and $N_{S/L}$ determine whether the system attains a stoichiometric or amorphous configuration.[90,125,157,159–161] Many experimental studies show that bCC's can only be produced when $0.154<\gamma_{S/L}<0.225$; however, simulation results suggest that $0.3<\gamma_{S/L}<0.41$ should be possible.[155] Recently, Cai *et al*.[92,155] have experimentally expanded the working size ratio to $\gamma_{S/L}=0.376$ through convective assembly in order to produce non-close packed binary crystals. For mixtures with particle size ratios ranging from the large particle being 3X to 5X larger than the small particles, entropic ordering has been widely cited as a strong driving force among sub-micron particles.[162,163]

Conversely, in granular mixtures, particle behavior is dependent on an external force (usually a vibration) to induce particle movement.[76] Typically the thermal energy in the system (k_BT), is orders of magnitude smaller than the energy required to move that particle an appreciable distance. However, oftentimes when binary particle mixtures are vibrated, a separation phenomenon known as the "Brazil nut effect" (large particles rise to the top and small particles sink to the bottom), is often observed.[164–166] Between each vibration, various metastable configurations may exist in the particle bed and these states last until the next vibration occurs.[29,76,166,167] Several factors affect the mixing/segregation behavior of large granular particles, including the frequency and amplitude of the vibration as well as the mass, density, diameter ratio of binary mixture, and the inter-particle and particle-wall coefficients of friction.[167]

Less is known about the assembly behavior of large, non-Brownian microparticles than nano- and granular (centi/milli-) scale particle behavior. Self-assembly of nanoscale components is usually limited to bottom-up methods while larger components are assembled via top-down

methods.[168] Micro-scale particles lie in the middle, however, with a great deal of untapped potential as building blocks to be manipulated in the creation of macro-scale functional materials. By employing self-assembly to organize non-Brownian particles, microparticle-based structures can be created with new opportunities for varying macroscopic hierarchy, surface functionalization, and the transport properties. Engineering these aforementioned properties, allows for design of novel materials for applications for which nanoscale features are not suitable. Here we explore a new method of creating autonomously assembled, microparticle-based crystals from particles with varying dimensions and compositions. Specifically, we employ sonication as a means of artificially "thermalizing" a system of large, non-Brownian microparticles such that we induce organization among particles up to 0.1 mm in size.[29] Furthermore, we observe that it is possible to produce a variety of multicomponent crystals with predictable stoichiometric patterns (corresponding to $N_{S/L}$) from particles that are two to three orders of magnitude larger than those previously studied in the literature. We have achieved particle organization for mixtures containing particles as small as d_S=0.6 μm and as large as d_S=21 μm combined with d_L=100 μm, where d is particle diameter, and S and L represent the small and large particle populations, respectively. While we refer to these crystals as bCCs and mCCs to follow with the nanoparticle naming convention, we acknowledge that the particles used are non-colloidal (due to size).

3.2 MATERIALS AND METHODS

3.2.1 Non-Brownian multicomponent crystal production

Non-Brownian particle-based bCC, mCC and particle-based inverted crystals (PBICs) were produced from a combination of soda lime particles (d=100 μm, NIST Standards, Fisher Scientific, Pittsburgh, PA) and polystyrene microspheres (d ≤21 μm from Bangs Labs, Fishers, IN; d >21 μm from Phosphorex Inc., Hopkinton, MA). Crystals were produced on circular cover slips (Fisherbrand, Fisher Scientific, Pittsburgh, PA), in disposable base molds (Fisherbrand, Fisher Scientific, Pittsburgh, PA), and in glass vials (Fisherbrand, Fisher Scientific, Pittsburgh, PA). In each case, the samples were placed on top of an ultrasonic bath (Branson Ultrasonics, Danbury, CT) for 20-90 minutes until dry (depending on particle solution volume and substrate) as in Lash *et al*.[29] For samples made on glass coverslips, 30 μL total volume (10 wt% solution) was used. The sample drying time ranged from 25-35 minutes (Figure 15). For samples produced in 3D molds, 100-200 mg of total particles were used and sonicated in 200 uL deionized water (DIW) at room temperature for 90 minutes. The number ratio of small to large particles can be determined from geometric consideration and influences the total mass of particles used to produce each sample.

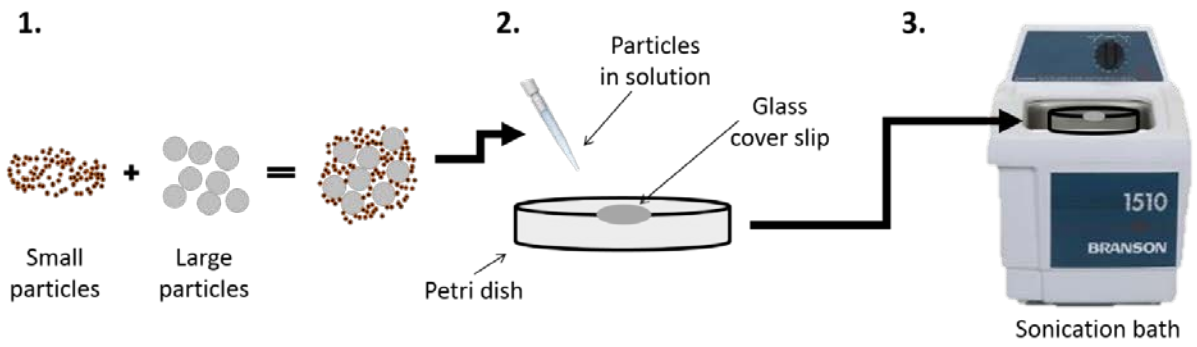

Figure 15: Schematic of binary crystal production process. 1) Mixing of two monodispersed particle populations. 2) Co-deposition of particles in deionized water on a glass substrate. 3) Introduction of sonication waves as a means of agitation. Crystallization occurs prior to fluid evaporation (see Chapter 2 for further explanation).[93]

3.2.2 Production of non-Brownian particle-based inverted crystals

Inverted crystals were created as described above in glass vials. For combinations of large soda lime particles and small polystyrene particles, the polystyrene particles were fused in an Isotemp Vacuum Oven Model 280A (Fisherbrand, Fisher Scientific, Pittsburgh, PA). 1 μm PS particles were fused at 130 °C for 90 min and 10 and 21 μm PS particles for 2 hours at 220 °C. The SL particles were then removed via a 5% hydrofluoric acid wash for 4-5 days followed by 1 day washing in DIW with constant end-over-end mixing. The wash solution was changed 1-2X/day. Prior to imaging, particle-based ICC samples were rinsed 5-10X with DIW and dried at room temperature.

3.2.3 Imaging and characterization

All samples were prepared for SEM imaging by sputter-coating with 5 nm gold/palladium alloy and imaging via JEOL scanning electron microscope. Samples were also analysed using a Nikon Ti-U inverted light microscope and an Olympus SZX10 Stereo microscope.

3.3 RESULTS AND DISCUSSION

We have achieved particle organization for mixtures containing particles as small as d_S=0.6 µm and as large as d_S=21 µm combined with d_L=100 µm, where d is particle diameter, and S and L represent the small and large particle populations, respectively. By further increasing the $\gamma_{S/L}$ above 0.21, we have formed crystals among particles where d_S=21 µm and d_L=75 µm, yielding a ratio of $\gamma_{S/L}$=0.28. However, as $\gamma_{S/L}$ increases, the likelihood for organization and achieving stoichiometric patterns decreases, as suggested in previous studies of sub-micro particles.[169] As such, we did not experimentally observe any pattern formation or long-range organization when exploring particle combinations where $\gamma_{S/L}$>0.28 or from particle populations with a dispersity, or particle size distribution above 5%. The process for producing these crystals is described in Figure 15.

In the crystallization process, a particle mixture in deionized water (DIW) is deposited at room temperature on a flat substrate and agitated by ultrasonic waves from a sonication bath. The sonication effects can be altered by changing the bath medium, the substrate, and the sonication solvent.[29] In this work we tested a variety of substrates including flat glass coverslips (both hydrophobic and hydrophilic), a cubic plastic mold, and a cylindrical glass vial; however, the bCC and mCC results shown throughout this work are produced on a flat hydrophilic glass substrate for

ease of imaging (although qualitatively-similar crystallization occurred with all substrates). When preparing samples for sonication, the volume of each particle solution (either polystyrene (PS) or soda lime glass (SL)) can be altered prior to mixing. We do not observe measurable differences when varying the volume (V) ratio across a reasonably wide range of values (<5X) (as determined by measuring the center-to-center distances among the large particles in the resultant structures); however, larger changes in the volume ratio (>5X) result in drastically different structures, depending on the number of large particles available and the area over which they were dispersed (data not shown).

Within each crystalline domain, we note a lack of overall homogeneity, as highlighted in Figure 16A. We hypothesize that this heterogeneity is due to variations in local particle concentration resulting from improper mixing of the component particles (similar to observations in Dai *et al*.).[170] Specifically, we observe a tendency for the small particles to form a layer on the substrate below the binary crystal (verified on inverted light microscope). At the same time, within the binary crystal, the concentration of small particles is often greater around the edges of the crystalline domain (Figure 16A). Despite inhomogeneity in particle mixing, the local variations in $N_{S/L}$ result in the expected configurations for these ratios, as highlighted by arrows in Figure 16A and with images in Figure 16B (where they are further correlated with variations in $\gamma_{S/L)}$.

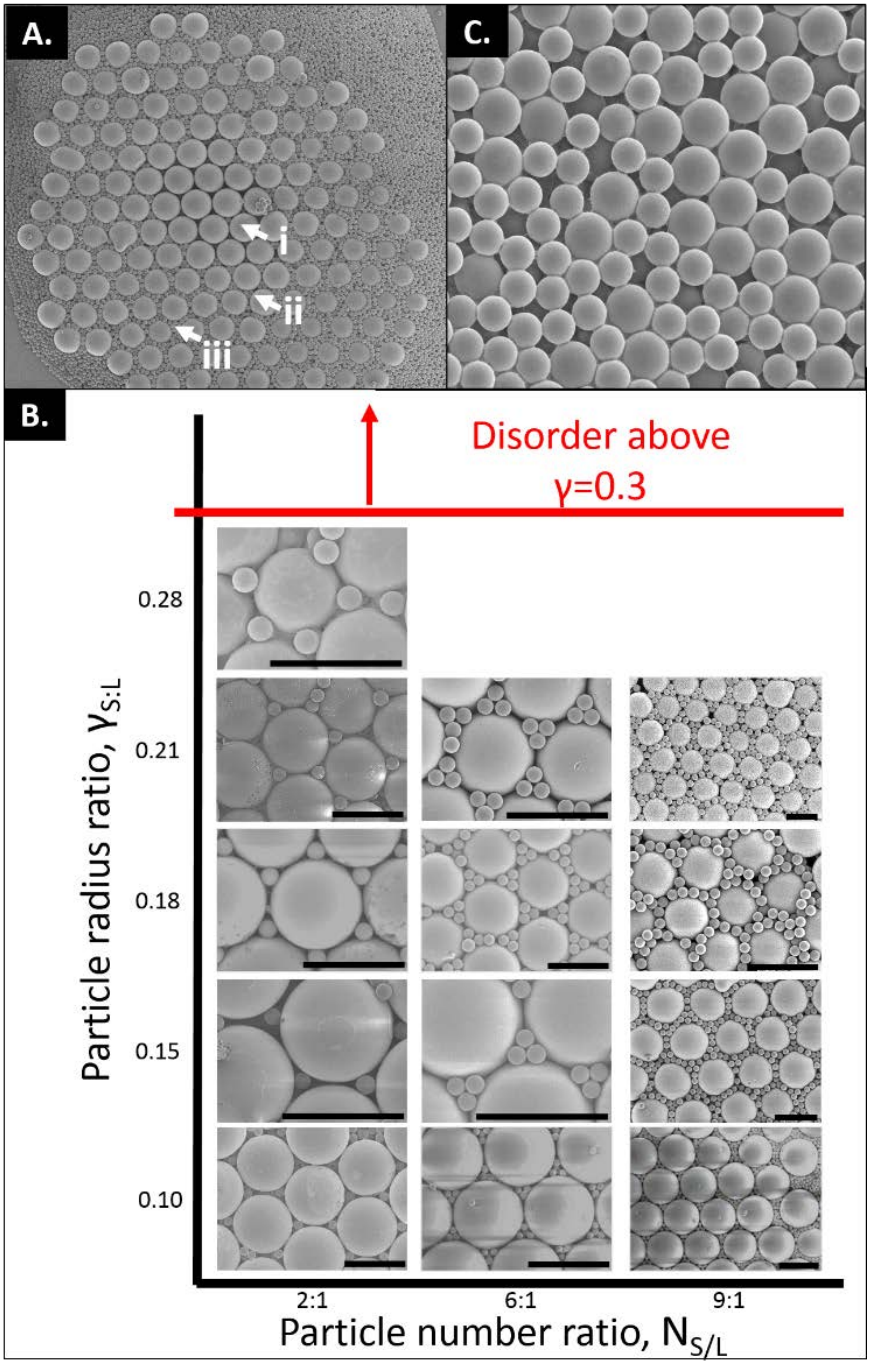

Figure 16: A) Representative overview image of a crystalline domain of 100 µm SL and 21 µm PS particles. The arrows i (2:1), ii (6:1), and iii (9:1) indicate different phases within the local regions on the sample. B) Structural configurations formed at various radius ratios, ranging from $0.1<\gamma_{S/L}<0.28$. C) Disordered packing observed between particles outside of a feasible number (stoichiometric) range that would be expected to produce order (21 µm and 15 µm in size, with $\gamma_{S/L}=0.71$). All scale bars are 100 µm.[93]

These areas of short-range order occur for $0.10<\gamma_{S/L}<0.28$. When the radius ratio is below 0.1 we observe closely packed structures of the larger particles, with space-filling from the smaller particles, but ultimately no discernable stoichiometric pattern formation (Figure 17). Stoichiometric pattern formation was not observed at this lower bound due to a geometric limitation, where the smaller particles are too small to remain in the larger particle interstitial spaces. On the other end of the stoichiometric spectrum, Figure 16C depicts the amorphous particle arrangement that is typical for size ratios close to unity (here, $\gamma_{S/L}$ =0.71), where instead of acting like independent particle populations the two particle sizes behave more like a single non-uniform population, thereby leading to disorder. Other incidents of disorder arise from the formation of defects and cracks in the crystalline structure. We suspect that the formation of defects for these non-Brownian bCCs occurs in a similar way to defect formation among nanoparticle mixtures and monodispersed particle-based crystals. The formation of defects and cracks may develop due to the competition between the dense crystal structure formation versus the hydrodynamic pressure in the fluid evaporation process, non-uniformity in particle size, or changes in the orientational configuration (e.g. switch between HCP and FCC).[160,171]

At higher particle number ratios of small to large particles, we no longer observe stoichiometric patterns. Instead, these binary crystals are characterized by smaller particles that "space fill" the voids within the larger particle crystal (as seen in Figure 17). For three dimensional crystals of this nature, this high level of organization can be seen throughout the crystal, as shown in the cross section displayed in Figure 18 and 21.

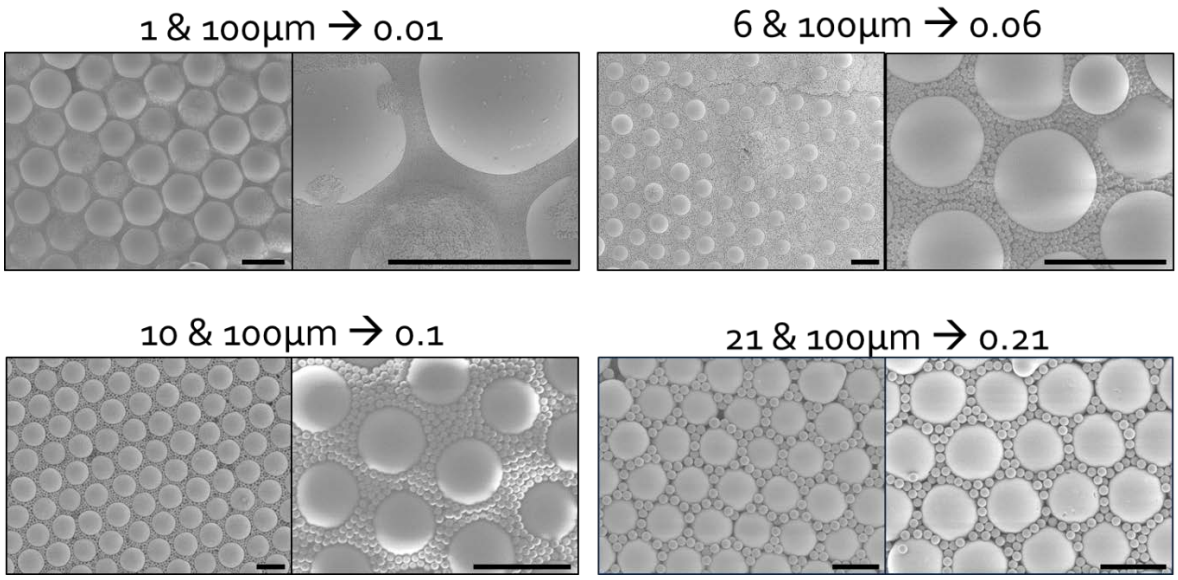

Figure 17: Binary crystals formed via sonication from particle mixtures with varying $\gamma_{S/L}$ with excess small particles. These structures serve as the template for creating particle-based inverted colloidal crystals. Scale bars are 100 µm.[93]

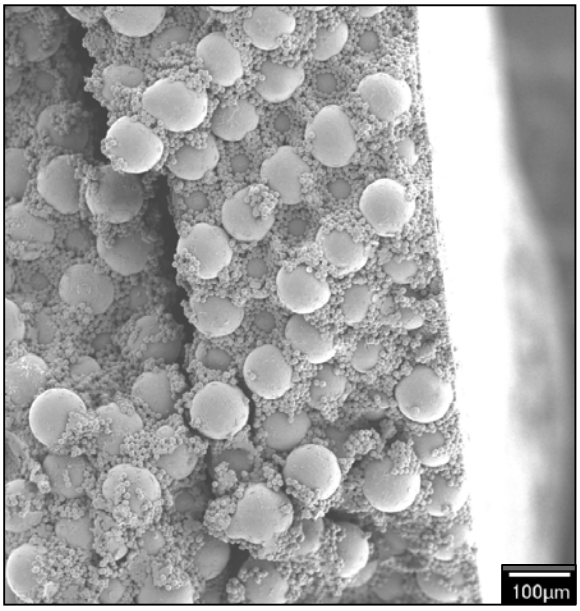

Figure 18: Cross section of 100 µm SL and 10 µm PS binary crystal captured by SEM.

The methods described here can be extended for the creation of binary crystals from granular particles (Appendix C) and multicomponent (tertiary) crystals with varying $\gamma_{S/M/L}$ (Figure 19). Many combinations of triphasic crystals should be feasible provided that a given phase and its nearest co-mixture population are within the observed size ratio ranges that allow crystallization (e.g. $\gamma_{S/M}, \gamma_{M/L} \leq 0.3$, but > 0.1) The mCC structures shown here are created via sonication on a flat substrate with all particle solutions in equal volume ratios.

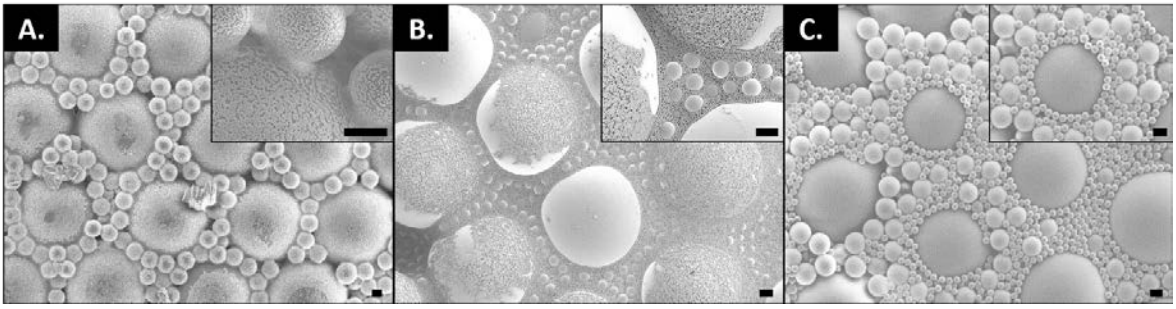

Figure 19: mCC structures created via sonication on a flat glass substrate. Triphasic mixtures were made from A) 0.6, 18, and 100 µm particles B) 1, 10, and 100 µm particles C) 6, 18, and 100 µm particles. All scale bars are 10 µm.[93]

We have also been able to successfully form inverse hierarchical crystals similar to those fabricated on the nano-scale.[91,172–174] Inverted colloidal crystals (ICC) are widely studied and templated with nanoparticles as well as with larger particles.[46,51,91,175,176] However, in all previously reported studies, the ICC backbone is comprised of a continuous solid material (usually a polymer).[92,108,113,173] Here, we demonstrate the novel use of fused, smaller microparticles serving as the backbone material to the ICC, creating an open and interconnected network known as a particle-based ICC. Figure 20 depicts the binary crystal template and Figure 21 depicts these structures formed from fused 1, 10, or 21 µm polystyrene particles that remain after etching away the 100 µm soda lime particles. The original binary crystal was co-assembled as described

previously, however an excess of the smaller particles was used to achieve a higher degree of sample homogeneity (bCC and particle-based ICC seen in Figure 20). These structures are observed to have long-range order over a large area, as shown in Figure 21B,D&F. Within these particle-based ICC's 1) niche microenvironments form in the large spherical cavities 2) an innate interconnectivity emerges from the porous nature of the crystalline walls composing the scaffold as well as 3) an increased internal surface area can be achieved by optimizing particle and fusion point size.

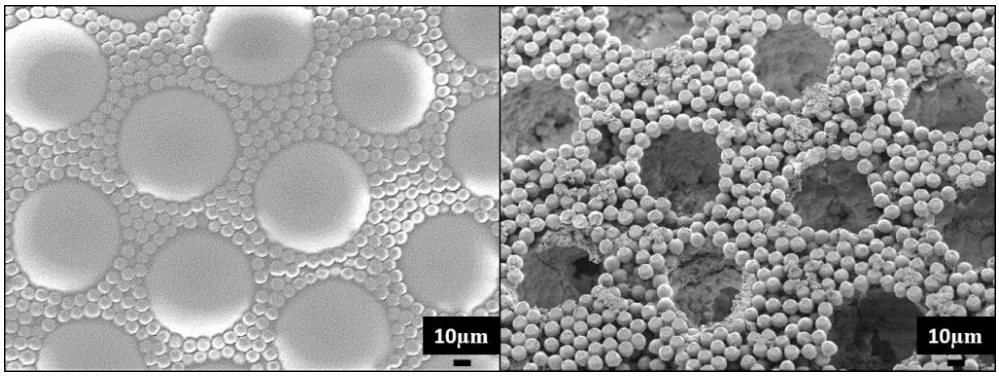

Figure 20: Binary crystal formed via sonication and its inverse structure. 100 µm soda lime and 10 µm polystyrene particles were co-assembled. To form the inverse structure, the 10 µm particles were fused together at 225 °C for 2 hrs. The 100 µm were etched away using a 5% hydrofluoric acid wash over 4-5 days, followed by a deionized water wash for 1-2 days. During washing, the wash fluid was changed 1-2 times/day and samples were mixed constantly via end-over-end rotation. All scale bars are 10 µm.

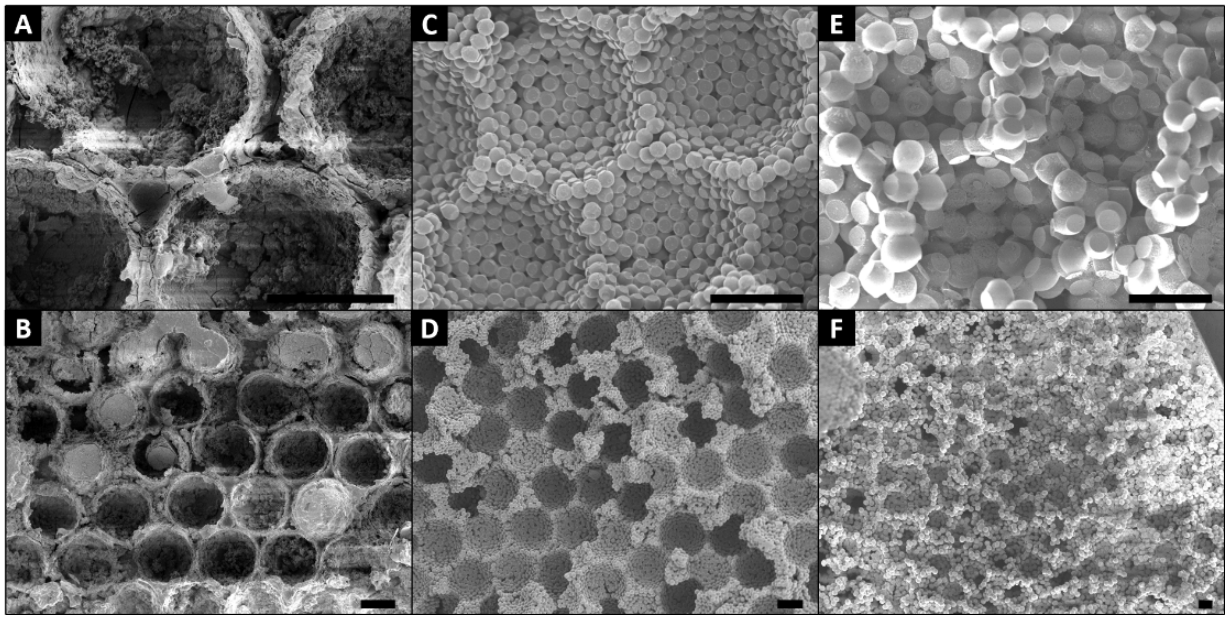

Figure 21: Inverted crystal composed of polystyrene particles post removal of 100 µm SL particles via a 5% HF/DIW wash sequence. The ICCs are made of A&B) 1 µm particles, C&D) 10 µm particles E&F) 21 µm particles. All scale bars are 50 µm.[93]

3.4 CONCLUSION

By agitating particles in a way that can overcome gravitational and kinetic limitations, we have shown that conventional applications of self-assembly typically employed at the atomic and nano-scale can be translated to the micro-scale where the impact of Brownian forces are negligible. Furthermore, this mimicry of natural thermalization processes can be used in the creation of larger scale multicomponent crystals and the formation of their inverse structures. These structures can be produced from particles of varying sizes and materials, allowing for rapid, bottom-up creation of hierarchical (and porous) materials that would traditionally be produced through a (potentially lengthy and costly) top-down approach. Additionally, their macroscopic shape can be easily engineered by varying the substrate shape in the fabrication process. These materials offer new opportunities for creating customizable and self-assembled niche microenvironments for drug delivery and tissue engineering, as well as new acoustic dampening, battery and filtration materials, among others. Additionally, they resemble naturally derived materials such as zeolites and biological tissue (e.g. bone, cartilage and lung), due to their high surface area, bi-dispersed pore distribution, and multilevel hierarchy.[50,108,177] Translation of such materials will require scaling up the crystallization process. Further investigation into the mechanism behind microparticle mixture organization may allow for the creation of large crystalline domains with long-range order within bCC, mCC, and particle-based ICC structures.

4.0 ORDERED MACRO-POROUS NETWORKS FOR BONE REGENERATION

4.1 INTRODUCTION

Using the crystalline structures built in Chapter 2 as a template, this chapter discusses our exploration into creating unique bone tissue scaffolds with large, regularly ordered pores from bioactive cements. As an extension of the crystals created in Chapter 2, the crystals created in here as templates are three-dimensional in nature and formed in pre-designed molds (as compared to the two or three dimensional free-forming crystals organized on a flat substrate in Chapter 2).

In contrast to the complex structures described in this Chapter, any of the aforementioned crystals could potentially serve as scaffolds for tissue regeneration given the right material combination and specific application. Scaffold design is an integral component of tissue engineering due to its role in facilitating the regeneration of new, healthy tissue in a way that mimics the body's natural regenerative processes.[50,54,178] This is of particular importance when there is an inability for the body to naturally heal itself, as in a nonunion bone fracture.[179,180] Traditionally, autografts or allografts are used for bone repair of defects and nonunions, and these methods are considered the gold-standard treatment. However, these approaches have considerable drawbacks, including the creation of a second surgical site to procure the autograft, chronic pain, and (in the case of allografts) potential immunogenicity.[181]

An emerging alternative approach to auto- and allografting is tissue engineered scaffolding. One category of engineered scaffolding uses synthetic materials that are both bioactive, such that they provide spatial and/or temporal cues for bone repair, yet break down and are flushed from the body when they are no longer needed.[181–183] Materials of this sort are able to elicit a controlled response in physiological conditions that cells will respond to. From an engineering perspective, a successful bone scaffold must possess high levels of porosity for cell infiltration and attachment as well as uninhibited pathways for nutrient and waste exchange while still maintaining appropriate levels of mechanical stability.[114,117] Calcium phosphates (CaPs) are an attractive material used for bone regeneration due to their similarities to native bone tissue, biocompatibility, high mechanical strength and osteoconductive and sometimes, osteoinductive properties (that is, they provide a surface that permits bone growth into its pores or channels and may even stimulate primitive cells to differentiate into a bone-forming cell lineage.[184–186]

Creating functional scaffolds with the aforementioned characteristics from CaPs in a reproducible manner is non-trivial, however. Traditional methods for inducing high levels of porosity (e.g. ceramic and pore-foaming techniques) typically provide limited control over pore structure and produce a random pore network that may be difficult to reproduce and ensure interconnectivity. Reports show that to ensure pore interconnectivity in the scaffold, the porosity often approaches 95%, which in turn, presents a problem in the structural integrity of the materials.[50] Therefore, the creation of a scaffold with a uniform and ordered pore distribution would ensure the reliability of the pore interconnectedness and the reproducibility of the microarchitecture, while not surpassing a threshold of 74% porosity.[50,53,108,114] Additionally, several reports suggest that ordered structures exhibit greater mechanical strength and elasticity, which in turn improves the functionality of a synthetic bone scaffold.[75,187,188]

Using the particle self-assembly techniques discussed in Chapter 2, we hypothesize that a non-Brownian crystalline array can be created as a template for producing an ICC scaffold for bone regeneration with a three-dimensional, macro-porous structure composed of interconnected niche microenvironments for the recruitment, infiltration and proliferation of osteoblast precursors cells from a mesenchymal stem cell (MSC) lineage. We first fabricated polylactic acid (PLA) and PLGA ICCs (as several reports in the literature have done) to hone our fabrication and imaging techniques.[46,109] Building from this approach, we sought to create CaP ICCs in order to capitalize on the innate bioactivity and structural properties of the cement, while exploiting the pore structure and interconnectedness of the ICC structure for cellular, nutrient and waste diffusion. In contrast to other porous CaP scaffolds, we will be incorporating controlled drug release within an ordered ICC composite scaffold into our design to mimic the body's natural repair mechanisms and improve the quality of the tissue regeneration.[114,189–191] In this approach we will be increasing the porosity from a maximum of 52% (previous reports use a square packed template) to 74% (we are employing an HCP template). Additionally, we will be releasing proteins such as platelet derived growth factor (PDGF) to recruit MSCs and bone morphogenetic proteins (such as BMP2) and transforming growth factor beta (TGF-β) to help induce osteoblast precursor growth, differentiation, extracellular matrix production and angiogenesis in the local microenviornement.[192] By designing a release schedule from a three dimensionally ordered macroporous bioactive scaffold, we hope to not only recruit new cells to the defect or injury site, but also increase the rate and quality with which those cells transform into healthy, new bone tissue.

4.2 MATERIALS AND METHODS

4.2.1 Soda lime particle crystalline templates

Glass vials (1 mL capacity) containing 150 μg SL particles and 200μL DIW were suspended in the sonication bath for 90 min. Following sonication, the fluid was allowed to fully evaporate. The soda lime crystals were then fused together via calcination for 3 hrs at 680 °C with a ramping rate of 15 °C/min in air. Fusion temperatures and times were varied in method development from 670-690 °C for 2-5 hrs before settling on this protocol.

4.2.2 Polymer-based inverted crystals

Solutions of PLA and 75:25 PLGA in dichloromethane (DCM) (10 wt%) were respectively added to the soda lime particle crystals post-fusion and cooling. The solution was added until the crystal was fully submerged (~200 μL). After the DCM fully evaporated, the glass vials were cracked and the samples were removed and transferred to a Nalgene container containing a 5% HF solution. Samples were rotated end-over-end until complete removal of SL particles was achieved as monitored on a stereomicroscope. Washing generally occurred over ~8-10 days with a daily exchange of wash fluid and end-over-end mixing. On days 4 and 7, the Nalgene container with sample was submerged for 10 s in sonication bath, the wash fluid changed and was then returned to mixing. On day 8, the sample was washed 5-10X in DIW, immersed in DIW for 24 hours of mixing and dried for further use. Notably, PS particle-crystals would not work in this combination due to the PS's solubility in DCM.

4.2.3 Polystyrene particle crystalline templates

Polystyrene (PS) particles (90 and 200 μm in diameter) were organized as described in Chapter 2. Briefly, 600 μL of particles in solution (10 wt% in DIW) were deposited and sonicated in stainless steel molds (as pictured in Figure 22) for 90 minutes. Samples were then fused at 165 °C for 48 hrs and 220 °C for 8 hrs respectively.

4.2.4 Cement-based inverted crystals

A cement slurry was added with pressure to infiltrate it throughout the particle bed. The cement powder (ReCaPP) was prepared by mixing calcium salts and disodium hydrogen phosphate. Alpha-tri-calcium phosphate (α-TCP, pure phase, Sigma-Aldrich, USA), calcium carbonate (99+%, Acros Organics, USA), calcium sulfate di-hydrate (99+%, Acros Organics, USA), and disodium hydrogen phosphate (≥99%, Sigma-Aldrich, USA) were mixed in an agate mortar-pestle for 30 min. Notably, SL particle-crystals would not work in this combination due to the cements inability to withstand HF washing.

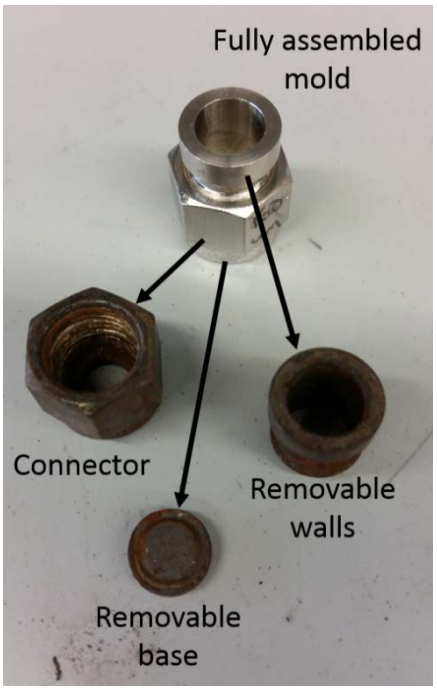

Figure 22: Stainless steel molds used to produce crystals via sonication. Molds can withstand high heat (T>700 °C)

4.2.4.1 Preparation of ReCaPP liquids

The liquid component of the ReCaPP consisted of a colloidal solution of nano-sized calcium phosphate (nano-CaPs) homogeneously dispersed in a buffer solution. Details of the nano-CaPs preparation can be found elsewhere.[193,194] Briefly, for each milliliter of nano-CaPs solution, 250 µl of 0.75 M $CaCl_2$ was added drop wise to a 750 µl of phosphate precursor solution, pH 7.5, comprised of 0.357 M NaCl (>99.5%, Fisher Scientific, USA), 13 mM KCl (>99%, Fisher Scientific, USA), 15 mM dextrose monohydrate (Fisher Scientific, USA), 64 mM HEPES free acid (99.5%, Sigma-Aldrich, USA) and 1.91 mM of $Na_3PO_4 \cdot 12H_2O$ (98+%, Acros Organics, Thermo Fisher Scientific, USA).

4.2.4.2 Cement preparation and hardening in the fabrication of scaffolds

Each of the cement samples was prepared by mixing 250 mg of the cement powder with 150 µl of the nano-CaPs solution in a polystyrene pour boat. Once mixed, the cement slurry was loaded into a 1.0 mL syringe and deposited on top of cooled PS crystals. A tamping device was then used to compress the cement encouraging infiltration through the crystal, filling its voids. Samples of cement and PS crystals were then placed in an incubator and allowed to harden for a minimum of 24 hours while incubated at 37 °C. PS particles were removed via calcination in air at 500 °C for 3 hrs with a ramping speed of 2.77 °C/min.

4.2.5 Imaging of scaffolds

Samples were cut using a razor blade for imaging cross-sections. An Olympus ZS100 microscope was used to visualize the pore structure of the sample and to watch the cement infiltration prior to drying. SEM was also used to image the scaffolds and a sputtercoat thickness ~5 nm was applied for imaging. MicroCT scanning of the scaffolds in water was conducted using a vivaCT 40 microCT system (SCANCO). Three dimensional images were reconstructed with SCANCO software at the same threshold across all samples. Each scan was reoriented with DataViewer (GE Healthcare). Scans were done at 55 kVp with a resolution of 10.5 µm.

4.3 RESULTS AND DISCUSSION

Three-dimensional SL and PS crystals were formed in a predetermined size and shape using the sonication methods discussed throughout this thesis as a template for creating inverted crystalline

bone scaffolds. Monodispersed particles ranging from 100-200 μm were selected for their ability to create highly organized templates, generate pore sizes that are large enough for angiogenesis and vascularization, and do not pose barriers to diffusion. [29,112,116,176,195] Both PLA and PLGA solutions were infiltrated into a PS crystal as shown in the schematic in Figure 23. Iterative experiments were conducted to develop a fusion protocol for these crystals as well as a washing protocol (data not shown).

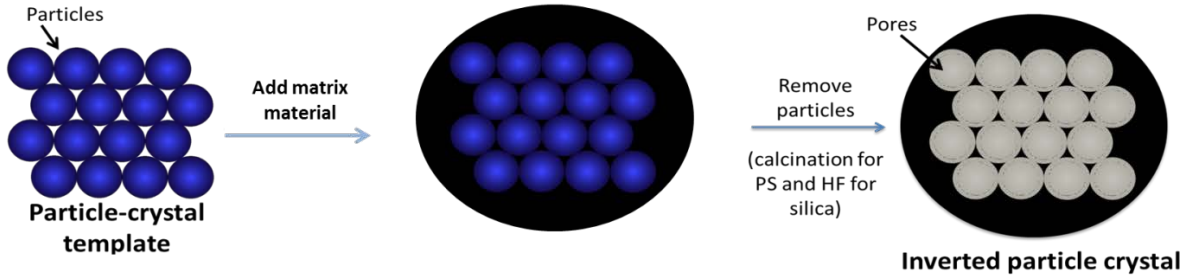

Figure 23: Schematic of ICC fabrication process

Figure 24 shows ICCs produced from PLA. In these experiments, both the PLA and PLGA scaffolds looked comparable from a macroscopic structural viewpoint. Interconnectivity of the pores was observed in both the PLA and PLGA scaffolds.

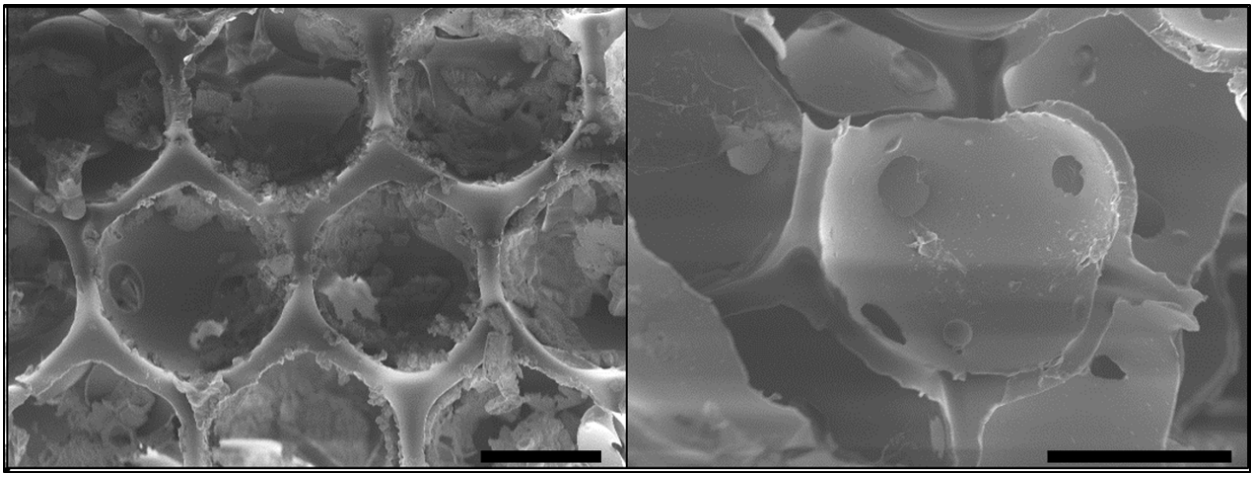

Figure 24: Representative SEM images of PLA ICCs. Scale bars are 100 μm.

Building upon our success in fabricating polymeric ICCs, we sought to create cement ICCs as well to capitalize on the interesting bioactive properties of the cement and build a stronger structure. Using the same crystalline templates, we pushed a cement slurry into the matrix and allowed it to harden at physiological temperature. During the template removal process the cement dissolved in our HF washing step so we transitioned to using a PS templating crystal with the same dimensions. Polystyrene template removal was tested via solvent washing (using organic solvents such as dimethyl sulfoxide (DMSO), DCM, tetrahydrofuran (THF) and acetone) and through calcination. Calcining the samples in air completed the particle removal faster and more efficiently than solvent washing did, resulting in highly porous and hierarchical scaffolds. Calcination temperatures tested ranged from 500°C to 700°C for times ranging from 30 min to 3 hours. We found that lower temperatures over longer periods of time (i.e. 500°C for 3 hours) led to the best results. When calcined for shorter durations of time, we did not observe full removal of the particles and the higher temperatures left a more brittle cement structure remaining. Figure 25 depicts the process of fabricating these CaP ICC scaffolds. (A) & (B) show the particle crystals prior to the adding of cement, (C) shows the crystal in the mold after calcination and (D) & (E) show views from a stereomicroscope and SEM respectively, of the macroscopic pore structure.

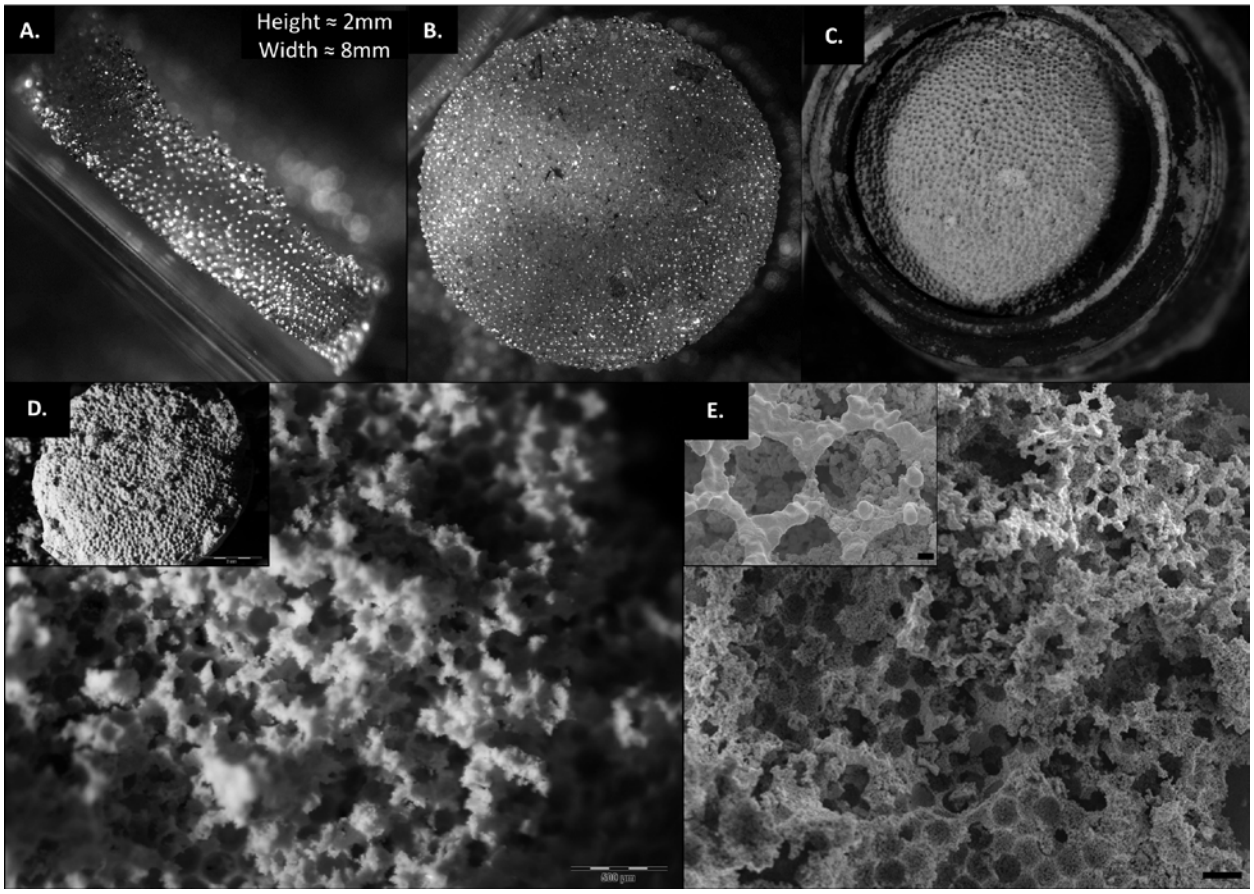

Figure 25: Production of a CaP ICC. A) side view of 200 µm PS crystal B) top view C) CaP cement added to the crystal in mold and imaged after calcination for 3 hrs at 500 °C D&E) CaP scaffold imaged once removed from molds post calcination. D) Scale bar is 5mm. E) Scale bar is 100 µm in the larger image and 10 µm in inset.

Micro computed tomography (microCT) was also used to visualize the cement scaffolds. microCT is an X-ray imaging technique that creates a high resolution 3D rendering of the sample. Figure 26 shows the microCT results showing the upper, lower and a side surface of the scaffolds. All images were taken at the same threshold and showed evidence of a pore structure. However, the resolution of the scans made these 3D renderings inconclusive on depicting an inner pore structure. In order to collect more illustrative scans in the future we will increase the resolution

(and decrease the high levels of noise in the scans) while and include control samples of solid CaP and PS fused particles to help discern our results.

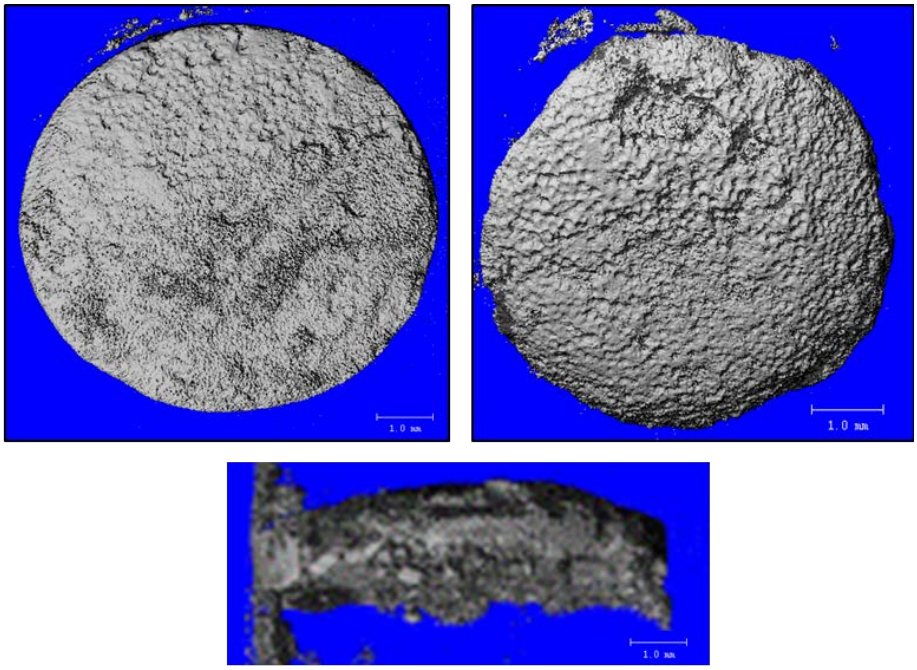

Figure 26: microCT rendering of CaP ICC scaffold showing the top and bottom layers as well as a side view which showed pores

4.4 CONCLUSION

The creation of these highly organized three dimensional CaP scaffolds serves as a proof of concept for creating a more advanced drug delivery system. In the future we are designing monodispersed PLGA particles (using a double emulsion process for protein encapsulation) of varying molecular weights (MW) to self-assemble as the template for the CaP ICC.[190,196] By mixing microparticles of different MW's, the length of time over which the polymer degrades (and subsequently releases the therapeutic agent) can be precisely tuned (as in Ref [190,197]), allowing for sequential delivery of therapeutic growth factors to the defect site. This type of temporal drug

release provides a “set of instructions” for the cells invading the defect site to guide them in forming new bone. The degrading PLGA particles will also be leaving behind an intact CaP ICC scaffold with niche microenvironments (void spaces) for bone to begin forming. We believe that these organized, controlled release CaP scaffolds will not only act as a support for bone formation but also provide spatial and temporal cues throughout the regeneration process.

5.0 ORDERED MACRO-POROUS NETWORKS FOR CATALYSIS

5.1 INTRODUCTION

This chapter expands upon the application-driven research in Chapter 4 to demonstrate the adaptability of our crystal formation techniques to a wide range of scientific fields. In a similar fashion to how we applied a particle-based crystalline template in tissue engineering, here we pursued the creation of active hierarchically structured catalytic materials using the methods developed in Chapter 3. In this Chapter we create binary crystals and their inverse structures from complex engineered nanomaterials (CENs). PBICs, as created previously, have an interconnected pore structure that would prove beneficial for bulk transport and are reminiscent of monolith structures currently used in catalysis research. However, if these PBICs were produced from an active nanoparticle backbone, a novel material can be produced that has both the advantages of a hierarchical pore structure, but maintains the available surface area and nanoscale structure of current state-of-the-art nanocatalysts.

Porous silica is widely used in industrial reaction engineering due to their tunable pore morphologies and high specific surface areas.[198] Precise control over the pore structure can lead to the selective uptake of molecules, enhanced interfacial contact and can facilitate rapid mass transport.[85,199,200] Furthermore, materials with a multimodal pore structure, or pore hierarchy, can

selectively allow molecular transport through one phase and ion transport through another.[200] Particulate catalysts are continually redesigned and synthesized for use in unique catalytic reactions. These newly designed catalysts continue to increase in complexity (e.g. shape, size, bimetallic composition, etc.). However, in application, these NPs are often unusable because they deactivate and sinter at high reaction temperatures.[201] Therefore NPs are typically coupled with an inert support, sintered into larger, stable NP aggregates or incorporated into a monolith structure. Monolith structures, albeit more difficult to synthesize, present numerous advantages to other support methods. Most importantly, using a monolith inside the reactor reduces the pressure drop compared to a packed bed with the same geometric surface area and allows increased gas flow, ultimately promoting faster conversion rates.[199,202] Monoliths also eliminate space and weight increases from inert supports (conventionally paired with free NPs). Lastly, the void fraction can be controlled when using a monolith structure. By incorporating pore hierarchy into the monolith structure, large macropores can be used to facilitate molecule transport and provide easy access to large active surface areas created by the presence of meso- and micro- pores. Furthermore, these macropores allow an escape path for the product and reduce the instances of unwanted secondary reactions.[203]

In designing an efficient and active catalyst/support monolith, the system must readily promote rapid heating of the catalyst to the operating temperature and be able to withstand thermal expansion (and contraction) without crack formation (in the material itself or the washcoat). Compared to conventional particle catalysts, monoliths offer numerous advantages, including high specific surface area, low pressure drop, efficient interphase mass transfer with low resistance, robust thermal and mechanical properties, and a simple method for scale up.[204–207] These properties can be attributed to the material's heat capacity, high mechanical strength and chemical

stability, resistance to shock, high temperatures, vibrations and fast conversions in feed composition.[204–206] By tuning the physical and geometric properties (e.g. shape, size of the channels, thickness and porosity of the wall as well as thickness and microstructure of the catalytic layer, etc.) of the catalytic system (monolith substrate and catalytic washcoat) the material can be customized for a variety of catalytic applications.[206,208]

One way to precisely tune the pore size, orientation, and multimodal distribution is to make use of a colloidal crystal template and create a three dimensional ordered macroporous material or inverted colloidal crystal (ICC). Traditionally in catalysis, nanoparticle-templated ICCs provide structures with the potential for high catalytic activity due to high surface availability and ease of mass transport, but would benefit from further increasing the available volume per surface area and removing diffusion barriers within the microchannels (to help prevent unwanted secondary reactions). We hypothesize that capitalizing on the benefits of the open pore structure of an ICC using large non-Brownian particles as the template, combined with a particle-based inverted crystalline backbone (PBIC), will help to enhance the available surface area and achieve hierarchy in the pore structure, where the macropores will facilitate bulk material flow and the smaller micropores will facilitate molecular transport and exhibit size selectivity. In this study, we create PBICs using both silica nanoparticles (NPs), which could act as a support for a plethora of active metal catalysts and complex engineered nanomaterials (CENs) made of nickel NPs embedded within porous amorphous silica in a hollow configuration (hNi@SiO_2).[209] This research serves as a platform for organizing CENs in a monolithic structure that would allow for scalable NP use in practical reaction engineering applications. Monolithic structures produced from CENs are unique because they will be lighter in weight by eliminating the need of an additional catalyst support yet will maintain high catalytic activity. They will be potentially cheaper to produce and will be a step

towards producing more sustainable catalysts (waste reduction by providing higher activity per volume materials). A synthetic monolith designed in this way will have strong diffusive properties from an open, interconnected pore structure, high surface area for reaction sites, and a hierarchical porosity than can be tuned for selectivity and separations purposes.

5.2 MATERIALS AND METHODS

5.2.1 Fabrication of silica nanoparticles (NPs) and hollow nickel NPs

Hollow Ni@SiO_2 (hNi@SiO_2) materials were made using a one-pot, multi-step reverse microemulsion synthesis previously developed in Ref[209]. 50 mL of cyclohexane (≥99%) and 10.5 g surfactant Brij 58 (≥99% polyethylene glycol hexadecyl ether, Mn ~1124, Sigma-Aldrich, USA) were refluxed at 50 ºC until the surfactant was fully dissolved. Next, 1.5 mL of 1 M $Ni(NO_3)_2 \cdot 6H_2O$ (99.999%) was added drop-wise, followed by 1.5 mL hydrazine hydrate (Sigma-Aldrich) to form a nickel hydrazine complex. Next, 5 g of tetraethylorthosilicate (TEOS, ≥99%) was added, followed by 3 mL of ammonium hydroxide (30%). After 2 hrs of aging for silica growth, particles were precipitated with 2-propanol, collected via centrifugation, washed three times with 2-propanol, and dried in air. The crushed powder was then calcined in a Thermolyne 79300 tube furnace for 2 hrs at 500 ºC in air.[210] Silica spheres were synthesized using the microemulsion hNi@SiO_2 procedure, except 1.5 mL DIW was added in place of the aqueous salt, and hydrazine was excluded. They were calcined for 2 hrs at 500 ºC in air. Before use in the PBICs, the NPs silica surface was rehydroxylated by stirring 0.1 g in 20 mL DIW at 95 ºC for 1 hr.[209]

5.2.2 Production of non-Brownian particle-based inverted crystals

Inverted crystals were created in stainless steel containers (depicted in Figure 22) from combinations of "large" and "small" particles in a binary crystal. For combinations produced from large polystyrene particles and small silica particles, crystals were formed via two methods. In the first method, a crystal made of 200 μm PS was first formed via sonication (as in Chapter 2).[29] The crystal was fused at 220 °C in an Isotemp Vacuum Oven Model 280A for 9 hrs. Upon cooling, a 10 wt% solution of silica nanoparticles (30-50 nm) (Produced via procedure above in Chapter 5.2.1) was added to the solvent and allowed to evaporate. In the second method, the two particle populations were sonicated together in solution (as in Chapter 3).[93] For both preparation methods, the binary crystals were calcined in air at 700 °C for 2 hrs with a 5 °C/min ramping speed. The time and temperature for calcination was determined using thermogravimetric analysis (TGA) in order to examine the sample's weight loss as a function of time and temperature. Samples were allowed to cool and then removed from the containers for imaging and characterization.

5.2.3 Characterization via electron microscopy

Samples were removed from molds, cut and mounted on stubs for imaging. Each sample was sputtercoated with a ~5nm gold/palladium coating and imaged via SEM. Nanomaterial particle size and morphology were characterized with transmission electron microscopy (TEM, JEOL-2000FX electron microscope). Particle measurements of TEM images were done using ImageJ software (http://rsb.info.nih.gov/ij/).

5.3 RESULTS AND DISCUSSION

Nano-PBICs were created here for the first time using both silica NPs and hollow nickel-silica NPs (hNi@SiO_2). Similarly to the PBIC's produced in Chapter 3, these scaffolds maintain both their nano- and macro- structures throughout the fusion process. Figure 27A shows the macroscopic structure while Figure 27B shows a zoomed in SEM image of the NPs and Figure 27C shows the individual particle identity maintained post-fusion via TEM for SiO_2 particle-based structures. These structures were produced via a two-step fabrication method, where the PS crystal was pre-formed and NPs were added post crystal fusion.

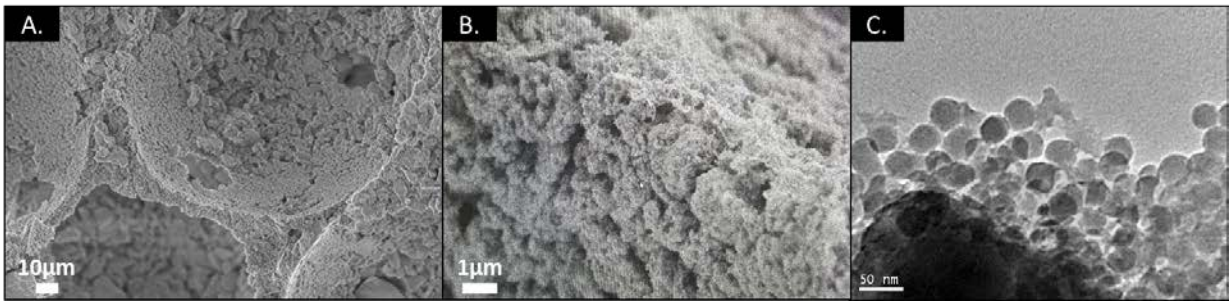

Figure 27: SiO_2 PBIC A) macrostructure B) microstructure C) NPs broken up (from PBIC) and imaged via TEM

In addition to the microscopy evaluation depicted in Figure 28, TGA was used to confirm the removal of the PS template by evaluating the sample weight loss over time and temperature increase. Loss of PS occurred from 250-400°C which is consistent with what is seen in the literature.[34,211,212] The greatest weight loss occurs during first 65 min at temperatures below 500 °C (Figure 28). However, in order to improve material stability and fuse the silica NPs, we raised the temperature to 700 °C for 2 hours. This also ensures that all of the PS will be removed during

this elongated time and at higher temperatures. Under these conditions, the silica monoliths were fragile upon handling, but remained intact.

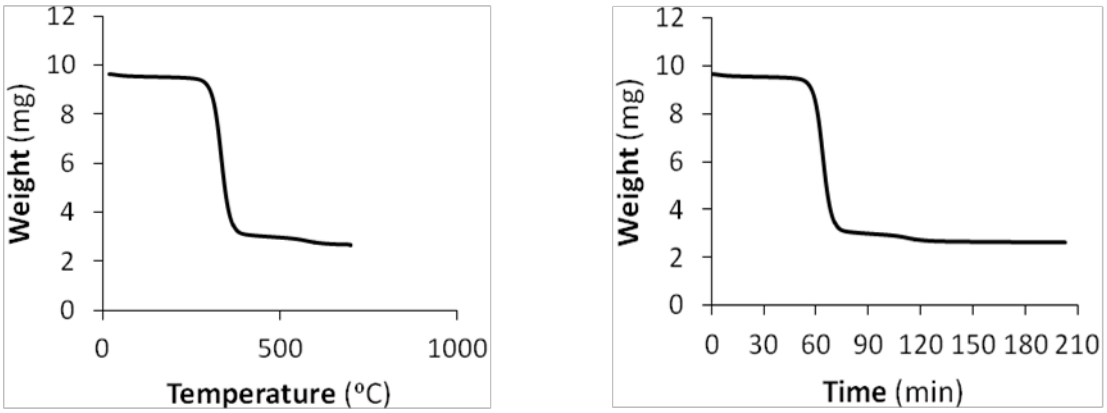

Figure 28: Weight loss of a sample of ordered 200 μm PS and 30 nm SiO_2 measured by TGA.

For many catalytic applications (such as the rapidly emerging technology of chemical looping combustion for clean combustion of fossil fuels[213]), silica is used as an inert support but alone cannot catalyze the reaction. In order to create a structure based on an active material, we transitioned to using hollow core-shell particles comprised of nickel NPs within a silica shell. We built these structures utilizing the same production and characterization methods as we did with SiO_2 NPs. One of the primary advantages to using these hNi@SiO_2 CENs involves achieving greater exposure between the active catalytic components and the reactants due to the high surface area and thin walls (low diffusion barriers), which is desirable in heterogeneous catalysis. These CENs behaved similarly to the SiO_2 particles and continued to present a problem in overall material stability. In both cases, imaging shows thin monolithic structures being formed. Figure 29 depicts why we believe these samples formed with far fewer layers than their template had. The NPs appear to not be infiltrating into the PS particle matrix to form a thick monolith. We observed

that the NPs in two different solutions remained on top of the crystal surface and never fully infiltrated the crystal.

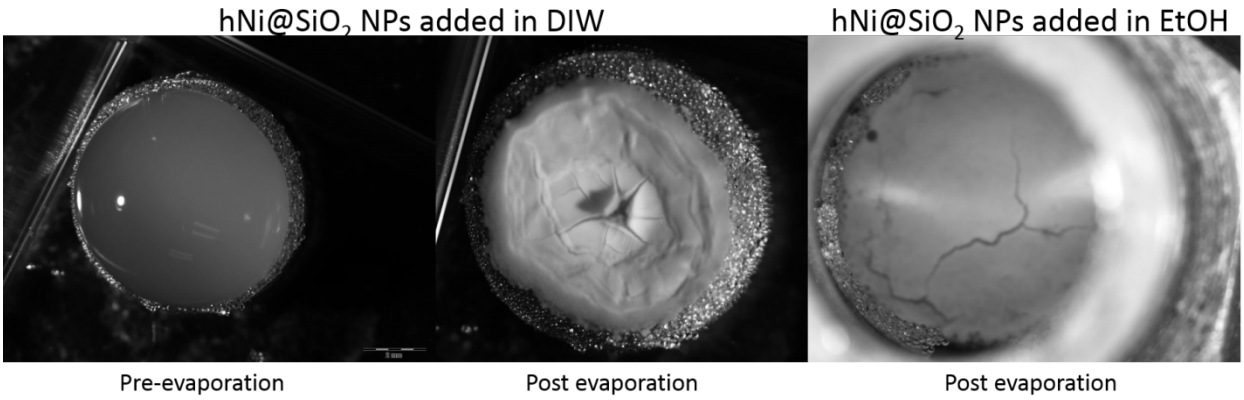

Figure 29: Depiction of NP solution behavior when added onto of a PS crystal. In both DIW and EtOH NPs layered on top of the PS crystal

In order to overcome this limitation (most likely arising from surface tension and hydrophobic effects[214] we sought to co-crystallize the hNi@SiO_2 NPs and PS microparticles. Figure 30 shows the resulting structures produced from hNi@SiO_2 particles co-crystallized with 200 μm PS. The overall structure is shown in Figure 30A&B, where (A) depicts the bottom of the sample, where there were primarily NPs in an unorganized manner and (B) depicts the top of the sample, where the macroporous structure is observed. As the sample was flipped over to image the top, it crumbled. Figure 30C represents a zoomed in view of (B) with an SEM inset of the pore structure. In order to ensure that individual NPs maintained their particle identity and did not fully fuse into a continuous phase (as it appears in Figure 30C), TEM was used to evaluate the state of the NPs post fusion (Figure 30D). In the TEM images, the grey outer ring of the particle forms from the silica shell which has a thickness of ~10 nm. The dark ring that appears on the inner wall of silica shell is composed of small nickel NPs with a diameter of 1-2 nm. In the center of the NP,

there is a hollow cavity with dimensions of ~10 nm in diameter. Through this analysis we observed that the NPs still maintained their individual particle identity, yet fused at their contact points. The thermal stability and reactivity of the hNi@SiO_2 particles have been well characterized in Ref [209]. In this work, we would like to repeat many of the same studies to compare the activity and performance of free hNi@SiO_2 NPs as compared to hNi@SiO_2 monoliths.

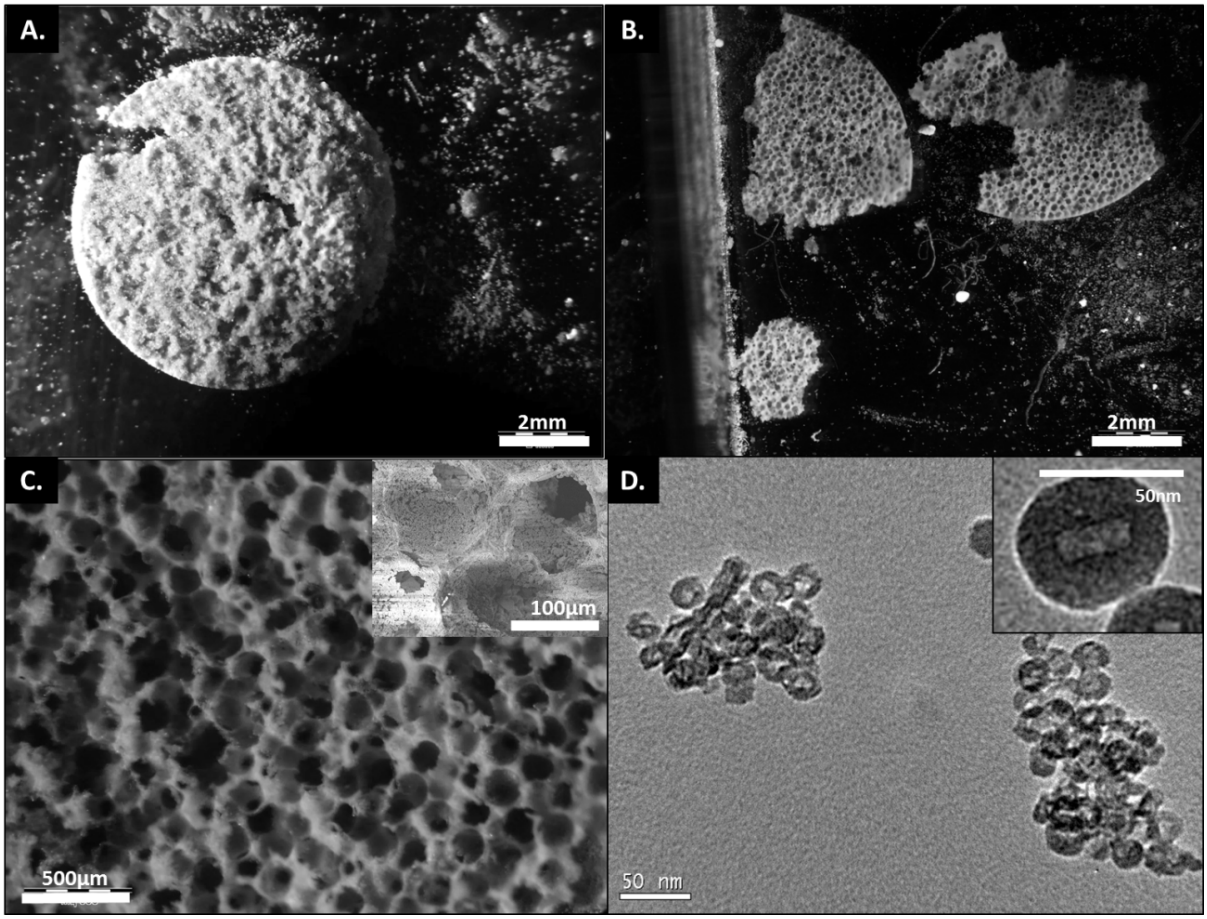

Figure 30: PBICs produced from hNi@SiO_2 NPs co-crystallized with 200 µm PS particles. A) Macroscopic view of the bottom of the co-crystallized PBIC structure B)Macroscopic view of the top of the co-crystallized PBIC structure C) Closer view of structure seen in (B) D)TEM of hNi@SiO_2 NPs.

The co-crystallized structures show great openness and interconnectivity through the windows of the macropores in the bulk structure using minimal amounts of material (<20 μg for a plug ~8 mm in diameter and 0.5-1 mm in height). Instead of forming an imprint as we saw when we used the two-step fabrication method, here we see layers and a dimensionality to the pore structure. However, we are still not fully gaining the sample thickness and mechanical stability needed for catalytic applications. We believe this is due to the Brazil Nut Effect causing a partial particle separation, where a layer of NPs forms on the bottom and then mixes with (surrounds) the microparticles above that layer.[165] This behavior is resulting in incomplete NP infiltration throughout the entirety of the PS crystal. The current ratio used was 60 μg PS and 20 μg of hNi@SiO_2, which should yield ~10 layers within the macropore structure. In our preliminary results, we are observing ~3-4 layers forming (which are an improvement over the two-step fabrication method we initially tested, which produced ~1-2 layers). We propose that incrementally increasing the number of NPs up to a 1:1 ratio will help to optimize the reproducibility and homogeneity throughout these structures with the goal of increasing the strength and robustness of the material.

Upon successful creation of these structures, we plan to characterize their efficacy as a catalytic monolith through multiple metrics prior to reactor testing. First, we plan to measure the surface area and porosity using Brunauer Emmett Teller (BET) analysis. A 6-point BET analysis will be used to measure total surface area and an 84-point N_2 BJH analysis with a Halsey thickness curve correction and Kruk-Jaroniec-Sayari correction to determine the pore size and distribution. Furthermore, we will test how the material can withstand the stress of varying reactor conditions by measuring the elasticity (stress/strain response) of the material using an Intron testing system and also measure the oxygen carrying capacity of the monolith at varying temperatures using TGA.

5.4 CONCLUSION

Designing CEN-based monoliths with macropores has the potential of having a large impact on the industrial scaling of catalytic materials. By forming PBICs through the co-crystallizing of CENs and microparticles, we are creating a structure that will have the capacity to withstand pressure drops and allows for better reaction conversions without the need for added supports. This unique monolith structure also eliminates the safety concern of airborne free NPs and creates high active site availability while maintaining uninterrupted pore diffusion pathways for bulk transport.

6.0 ORDERED MACRO-POROUS NETWORKS AS LITHIUM ION BATTERY ELECTRODES

6.1 INTRODUCTION

The crystals and PBICs created in Chapters 2 and 3 also show great promise as a platform for creating electrode materials for energy storage and conversion. In this Chapter we will discuss our preliminary studies in carbonizing PBICs and our plans for further experimentation and battery testing. The primary goal of this work is the development of a novel, high-efficiency electrode for use in lithium ion batteries.

Lithium ion batteries (LIBs) are a class of rechargeable batteries that are increasingly attractive due to their use in portable electronics, electric vehicles and the storage of renewable energy.[4,215,216] To meet the demands required by these applications, LIBs are designed with the ability to increase the energy storage capacity by 100–150% per unit weight and volume compared to traditional aqueous batteries and have long cycle lives.[4,34,215,216] These batteries operate through ion transfer between a positive and negative electrode in their charging and discharging cycles. The state of the art in LIBs is plagued by low energy and power density, high costs, and large reaction volume changes. Additionally, the electrode (usually made of carbon or graphite) often suffers from less than optimal electron pathways and the need for binders or conducting agents

embedded within them to allow for good conductivity.[4,34] By creating a monolith-like structure from non-Brownian particles as an electrode for LIB's, there would be structural advantages derived from the interconnected pore framework for ion and bulk fluid diffusion with the intent of creating longer lasting batteries. Additionally, by coating these structures in silicon, which reacts with lithium at low potentials and has a high theoretical specific capacity, the performance and life-cycle of the electrode material can be elongated.[216] In this work, we are taking two approaches to forming high surface area electrode materials with a pore structure that may significantly enhance mass transfer and surface availability for energy storage. The first approach involves carbonizing a polystyrene-based PBIC and coating the material with silicon and the second involves creating silicon foam from a crystalline soda lime template. In both of these strategies, a three dimensionally ordered porous structures provide ample space for reaction volume fluctuations and possess an increased capacity for material loading due to the low material per volume ratio.[89]

6.2 MATERIALS AND METHODS

6.2.1 Production of non-Brownian particle-based inverted crystals

Inverted crystals were created in stainless steel containers (depicted in Figure 22) from combinations of "large" SL and "small" PS particles in a binary crystal as in Chapter 3.2.2. Samples were prepared with both 1 μm and 10 μm PS beads. An Isotemp Vacuum Oven Model 280A (Fisherbrand, Fisher Scientific, Pittsburgh, PA) was used to fuse the samples, where 1 μm PS particles were fused at 130 °C for 90 min and 10 μm PS particles for 2 hours at 220 °C. Upon

cooling, the samples were placed in a furnace in an inert Argon environment (atmospheric pressure) and heated to 625 °C for 3 hrs with a ramping speed of 7.5 °C/min. The soda lime particles were then removed via a 5% hydrofluoric acid wash for 4-5 days followed by 1 day washing in DIW with constant end-over-end mixing. The wash solution was changed 1-2X/day. PBICs were rinsed 5-10X with DIW and dried at room temperature for future use. The samples were then placed under vacuum and coated with a uniform amorphous Si coating using a low pressure chemical vapor deposition system (LPCVD). 2% silane (SiH_4) in argon gas was decomposed at 500 °C to form a coating ~100 nm in thickness.[215]

6.2.2 Production of silicon foams from non-Brownian soda lime crystals

Similarly to the PS particles described above in Chapter 4.2.1, soda lime particle-based crystals can be produced via sonication in DIW for 90 min in stainless steel containers (depicted in Figure 22). 150 µg of soda lime particles were weighed out and dispersed in 200µL DIW. Once prepared, the soda lime crystals were fused together via calcination for 3 hrs at 680 °C with a ramping rate of 15 °C/min in air. The crystals were then placed under vacuum and coated with an amorphous silicon coating as described above and in Ref [215]. The SL template was then etched away using a 5% HF rinse for ~30-60 min while being periodically monitored via microscopy for complete removal of SL.

6.3 RESULTS AND DISCUSSION

6.3.1 Carbonization of microparticle PBICs for electrode materials

Using the PBIC's discussed in Chapter 3 (like those pictured in Figure 22) Figure 32 shows PBIC's that have been carbonized to increase the porosity and conductivity of the material. In the carbonization process, the polystyrene burns to form an ordered, porous carbon network. However more work needs to be conducted to improve the reproducibility and robustness of these materials for energy storage and conversion. With the creation of small samples of carbonized PBIC's we have observed the potential for an effective electrode material upon the fabrication of larger samples. Currently, we are working on coating these materials with silicon to act as a semiconductor for the transfer of ions between the electrolyte fluid and the carbon backbone. Upon creation of this structure, we will conduct electrochemical testing of this material as an LIB anode will be completed as done in Ref. [215].

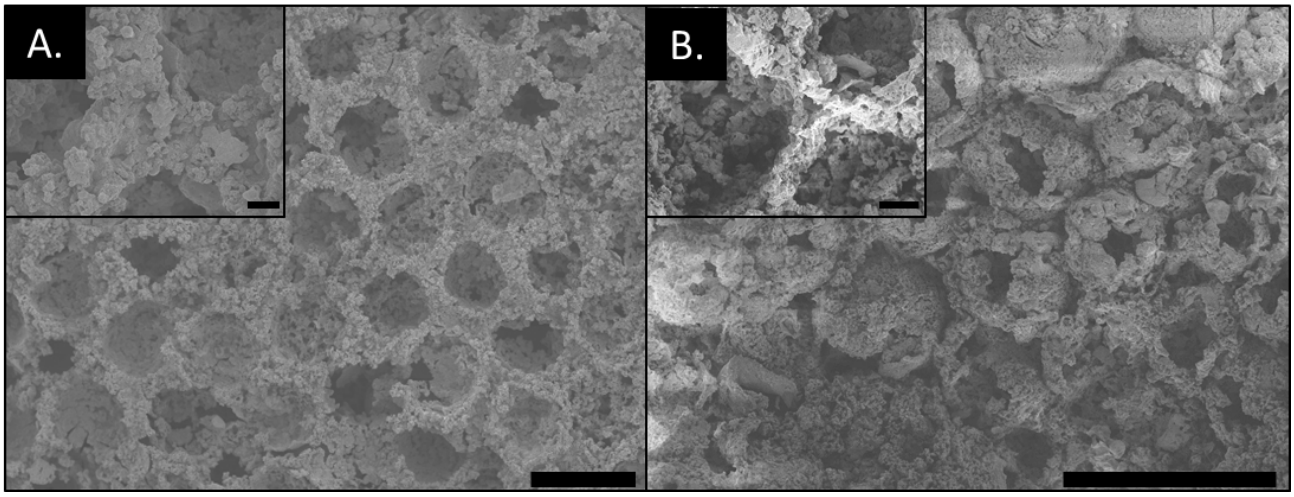

Figure 31: PS PBICs converted to carbon made from A) 10 μm and B) 1 μm particles. Scale bars are 100 μm in the larger pictures and 10 μm in the insets.

6.3.2 Silicon foams as electrode materials

Highly organized soda lime crystals were formed via sonication methods (as in Chapter 2) and gently fused together at high temperatures. These crystals were coated in a ~100 nm silicon coating and then soaked in a 5% HF solution to etch away the particle template. Evidence of the coating can be seen in the color change of the crystal which was initially white. Figure 32 shows the macroscopic structure of these foam precursors. The structure was monitored throughout the etching process. Both SL and silicon can be etched by an HF solution, however SL etches at a greater speed.[216] In Figure 32A, the coated crystal is shown prior to washing. Every half hour the sample was monitored for the removal of particles and the HF solution was replaced. After two hours of washing we removed many (but not all) of the SL particles. On the surface we can observe evidence of these "cages" and the remaining space where particles once were (Figure 32C). Through the washing process, evidence of silicon etching was observed in the form of metallic flakes in the wash solution. Further analysis via electron microscopy (both SEM and TEM) will be used to measure the thickness of the remaining coating and determine if the overall structure remains dense (particles remain) or has become hollow (full removal of particles).

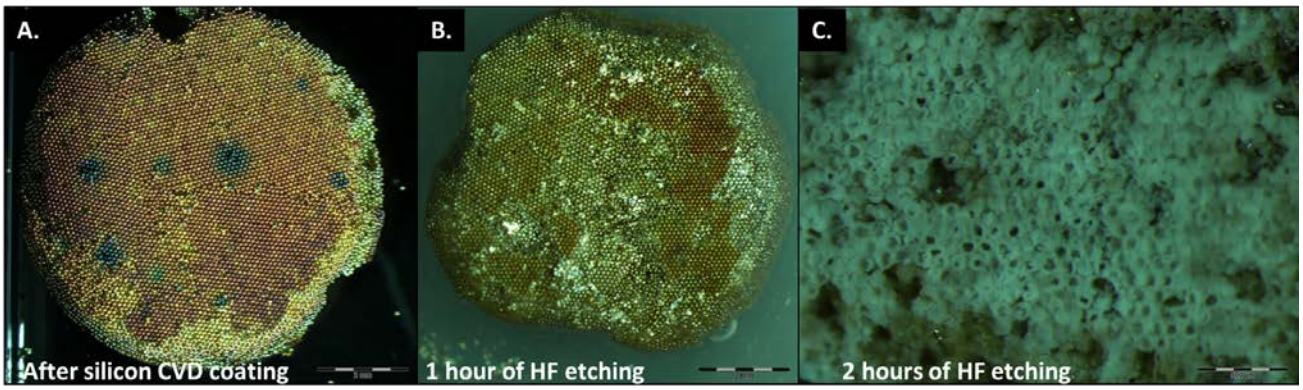

Figure 32: A) 100μm SL particle-based crystal coated with silicon through chemical vapor deposition. B) after 1hr of 5% HF washing during gentle agitation C) after 2 hours of HF washing. Sample was dried and imaged

6.4 CONCLUSION

The fabrication of monolith-like structures from non-Brownian particles appears promising as an electrode for LIB's. The preliminary results described here suggest that these architectures can be designed to exhibit an interconnected pore framework for ion and bulk fluid diffusion out of conductive and semi conductive materials with the intent of generating longer lasting batteries. Future electrochemical testing of these materials will help to optimize the performance and life-cycles of these new electrode materials.[216]

7.0 USING SELF-ASSEMBLY TO CREATE PARTICLE SURFACE PATCHINES

7.1 INTRODUCTION

The last application of non-Brownian particle organization that we studied involves using the self-assembly process itself (Chapter 2) as a means of imparting surface patterns on the particles. These preliminary studies illustrate the potential for this labeling technique as an extension of previous research published in the Little lab.[138]

In nature, biological signatures of anisotropy or "patchiness" are abundantly seen, such as on cell's surfaces during tissue organization or during an immune response.[217,218] Synthetic materials, such as spherical particles, can be fabricated to mimic this anisotropy.[138,219] By labeling the surface of a synthetic particle, a new class of particles known as patchy particles have been created.[220,221] Patchy particles are defined as particles on the nano- or micro- scale with at least one well-defined patch on their surface and that interacts with other particles or surfaces through highly directional, anisotropic interactions.[221,222] The number of patches on the surface of the particle, as well as the patch composition, can lead to different functionalities and applications of this emerging technology.[221] Techniques such as micro-contact printing, physical vapor deposition, or fluid masking can be used to modify a portion of the particle's surface.[220] Recently, Kamalasanan *et al*.[138] demonstrated that forming patches on particles can be done by exploiting a particle's orientation with respect to its neighbors for selective masking (templating). For

instance, aligning particles linearly can lead to the formation of two or three patches (one at each contact point and potentially one at the bottom contact point) and create a colloidal crystal or 2D hexagonal array that can lead to six patches. Building upon this technology, we are looking to scale the aforementioned approach to even larger non-Brownian particles and capitalize on the organizational process as a means of imparting patterns.

The creation of large patchy silica and polystyrene particles (100 μm in diameter) is completed using a similar crystallization process as described in Chapter 2 for non-Brownian particles with the addition of a dilute masking agent. The masking agent localizes at the contact points as the fluid surrounding the particles begins evaporating and forms liquid bridges. During evaporation these liquid bridges are the last points to dry, leaving behind patches of concentrated masking agent. The different masking agents used here were a biphenyl solution in DMSO and a dilute gelatin (Jell-O®) solution in water. Techniques for fluorescently labeling the particle surfaces are being explored in order to determine the surface patterns on the particles after the crystal structures have been dispersed. Polystyrene surface labeling was completed using antibodies conjugated to fluorophores and the silica labeling was done using organosilanes.

7.2 METHODS

7.2.1 Particle surface modification

Carboxylated PS particles (Bang's Lab, Fishers, IN) were washed once in 25 wt% ethanol in deionized water and twice in deionized water. Prior to labeling, the particles were washed in a Polylink coupling buffer (Bangs Labs, Fishers, IN), twice in preparation for the addition of

aminated primary antibodies using carbodiimide chemistry.[223] A 200 mg/mL solution of EDAC (1-ethyl-3-(3-dimethylaminopropyl)carbodiimide)) in coupling buffer was prepared. A 166.7 mg/mL solution of Sulfo-NHS (N-hydroxysulfosuccinimide) in buffer was also prepared to stabilize the reactive esters that are made when EDAC reacts with the carboxyl groups on the polystyrene surfaces. 2 μL of EDAC solution and 6 μL of Sulfo-NHS solution were added to each 10 wt%, 50 μL PS sample. The samples were put through end-over-end mixing for twelve minutes immediately after the addition of the Sulfo-NHS and EDAC. The samples were then centrifuged for 3 minutes and the supernatant was removed. 50 μL of phosphate buffered saline (PBS) was added to each sample followed by 8 μL of Goat Anti-Mouse IgG (H+L) and mixed end-over-end overnight at 4 °C. Samples were washed three times with 50 μL of Polylink wash/storage buffer (Tris buffer) to block any open sites and washed twice in PBS. 50 μL of PBS was added to each sample along with 8 μL of Alexa Fluor 647-conjugates AffiniPure Donkey Anti-Goat (AF647) while end-over-end mixing for 45 min fluorescent conjugation. This procedure was also repeated with AF488 (green) instead of AF647 (red), replacing the Goat Anti-Mouse with Rabbit Anti-Bovine and AF647 with AF488. The samples were washed with 50 μL PBS and imaged using a Nikon Eclipse Ti microscope.

Silica particles (Corpuscular Inc, Cold Spring, NY) 100 μm in diameter were washed twice with 95% ethanol prior to surface modification. A 7.2 vol% solution of (N-(triethoxysilylpropyl)dansylamide (green silane) in ethanol was prepared and allowed to react for two minutes prior to adding to each sample of washed silica particles. Conversely, a 0.041 mg/mL solution of ((R)-N-triethoxysilylpropyl-o-quinineurethane)), (blue silane in crystal form) was prepared in ethanol. This solution was heated and stirred until the crystal dissolved. The solution was allowed to react for 2 min and then added to the particles. For both chemistries, the samples

were end-over-end mixed for 3 min and then the supernatant was immediately removed. The silica particles were then washed twice in ethanol, dried and imaged using a Nikon Eclipse Ti microscope.

7.2.2 Patchy particle creation

Patchy particles were fabricated from both polystyrene and silica particles. Once the polystyrene particles were washed with 25% ethanol and deionized water, and the silica particles were washed with ethanol, a masking agent was added to both PS and silica particles. The two masking agent solutions used in this experiment were a 75 mg/mL biphenyl in DMSO solution and a solution of 0.60 mg/mL gelatin powder in deionized water. The masking solutions were added respectively to particle solutions and deposited on a hydrophilic glass slide to undergo sonication (as in Chapter 2).

The particles were then dually labeled so that the portions of the particle surface that were not at the contact points or covered with the masking agent were labeled first. Following the removal of the masking agent from the contact points, the patches of the particles were labeled with another agent. The polystyrene and silica particles were labeled with the first color following the labeling procedures provided in Chapter 7.2.1. Because AF647 and the green organosilane are less bright than their counterparts, they were added to the particles in the first round of labeling. After the first round of labeling, the masking agent was removed. To remove the gelatin patches attached to the silica surface, the particles were washed twice with hot water. The biphenyl was removed from the polystyrene particles by washing the particles with DMSO. The particles were then labeled with their respective second labeling agent at the patches using the appropriate labeling procedure. The particles were imaged using a Nikon Eclipse Ti microscope.

7.3 RESULTS AND DISCUSSION

The masking agent used during the formation of the colloidal crystals greatly impacted the surface pattern and characteristics of the patches. Various concentrations of gelatin and biphenyl solutions were tested to determine the effect of the masking agent concentration on the patch size. For a gelatin solution, the patches were very inconsistent at concentrations below 0.60 mg/mL. For particles with biphenyl patches, we found that concentrations of 75 mg/mL (in DMSO) resulted in a more consistent patch formation. Figure 33A illustrates how the masking agent (fluorescent sodium salt was used preliminarily as a proof of concept) gets localized at the contact points prior to breaking the crystal apart for further modification. Figure 33A shows patch formation at the contact points using the florescent salt. Since this salt is water soluble, however, we did not further use it when labeling with antibodies, as it would get washed away during the labeling procedure. In Figure 33B&C representative images of particles masked with a gelatin solution (Figure 33B) and a biphenyl solution (Figure 33C) are shown. The size of the patches made on the particles when using gelatin as the masking agent was smaller than when using biphenyl. This discrepancy in size may arise from the partially solubility of PS in DMSO during the labeling process, causing the PS to swell slightly and fuse. The patches observed may be breaking points that have biphenyl on them. Further testing, possibly with EDAX could help to determine the chemical composition of these patches. Neither masking agent produced uniform patches, however the patches made when using a biphenyl solution appeared more consistent than the patches made using a gelatin solution.

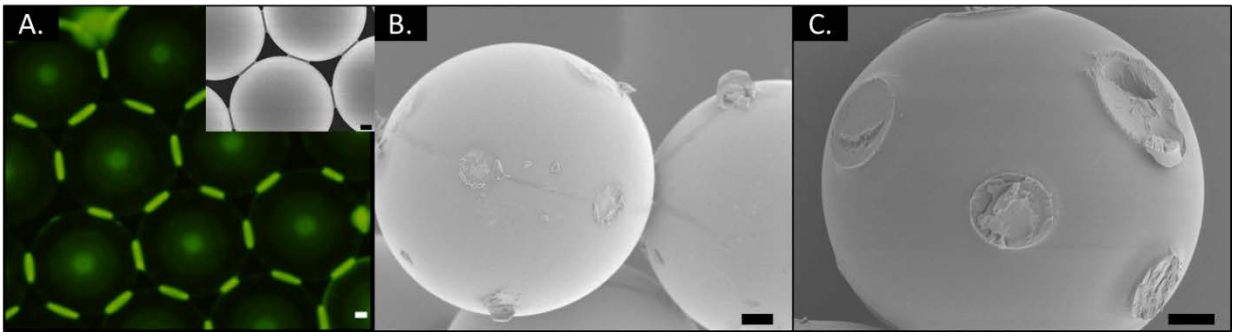

Figure 33: Patchy particles formed via the process of colloidal assembly in a A) dilute fluorescent salt solution with SEM inset showing masking bridge formation B) 1.13 mg/mL gelatin solution broken up to see patches C) 75 mg/mL biphenyl solution broken up to see patches. Scale bars are 10 μm in length.

Using the biphenyl and gelatin masked polystyrene particles, dual-labeling of the surface with proteins was preliminarily explored. Polystyrene particles jointly labeled with AF647 and AF488 are shown in Figure 34A. This representative image shows the dual labeling and formation of patches on the particle surface. However, there is some overlap in excitation color, resulting in the patches looking yellow-green and the surface appearing an orange-red color (instead of being starkly red and green as in ref [138]). Figure 34B shows a representative image of dually-labeled silica particles. Similarly to the observations made for surface modified polystyrene particles, we did not see clear distinctions between patch and surface upon fluorescent imaging. This lack of resolution may be due to the similarity between the absorption wavelengths of the green and blue silanes. Overall, these results suggest that more research is needed to improve production methods for creating patchy particles. It appears that there is incomplete coverage of the masking agent at the patches and likely nonspecific adsorption of protein or dye to the particle surface (additional data and discussion in Appendix B).

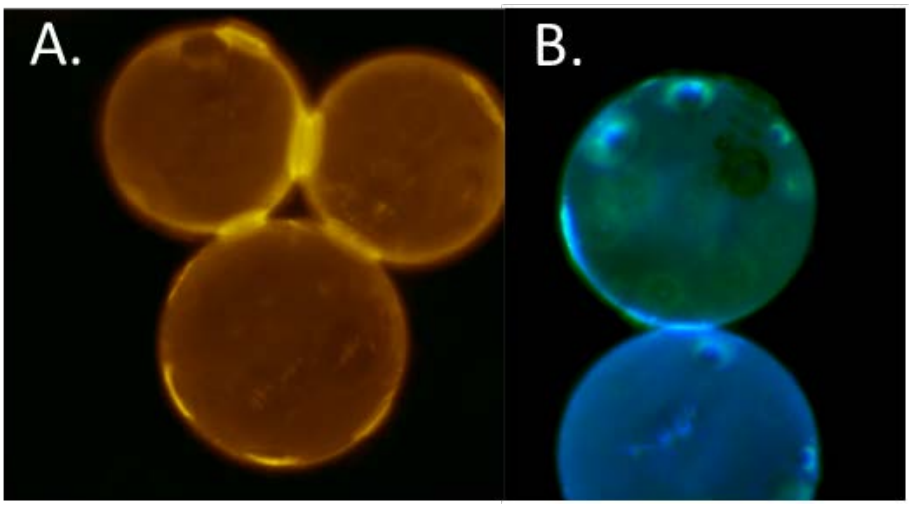

Figure 34: (A) Dual labeling of 100 µm polystyrene particles with unmasked portions of the particles were labeled with AF647 dye (red) and the contact points were labeled with AF488 dye (green) (B) Dual labeling of 100 µm silica particles with unmasked portions of the particles were labeled with blue dye and the contact points were labeled with green dye.

Additional experiments and research into creating solid and reproducible patches on particles of both polystyrene and silica will help to improve the quality of patches produced. All of the images presented in this work were taken using a Nikon inverted light microscope and SEM at each step of the labeling process (surface conjugation observed in Appendix B (Figure 41)). Using confocal microscopy or other techniques may help to improve the imaging of these particles to more accurately depict the patches and particle surfaces the three dimensions. Since this work has been completed, we have found new particle suppliers who are able to create more uniformly sized particles. Perhaps repeating these experiments with particles of greater size uniformity and in a 3D mold will help to improve the reproducibility and quality of patch formation.

7.4 CONCLUSION

Using the self-assembly process to label particles is a technique that can be implemented with ease and on a short time scale. Our preliminary work shows examples of patch formation and surface modification on two different types of particles. By continuing to improve our labeling and imaging techniques, the goal of conjugating carefully chosen chemical groups to the patches is within reach. In the future, we would like to increase the complexity and versatility of patch formation with the hope of creating smart particle systems with capabilities ranging from acting as an artificial immune synapse to systems that can rationally autonomously assemble.

8.0 FUTURE STUDIES

The methods for non-Brownian particle assembly described throughout this thesis serve as a platform through which we are exploring repurposing crystalline-based materials for a variety of applications. Namely we explore their use in bone tissue engineering, catalysis and energy storage and conversion. To further our exploration into these specific fields as well as others, additional research into the mechanism by which non-Brownian particles organize may help to drive their application forward. Additionally, we present here the creation of hierarchical materials prepared for these applications but need to continue our exploration into testing their efficacy and optimizing their design and scale-up for practical usage. This Chapter serves as an explanation of how we believe this research can be continued to achieve these goals.

8.1.1 Non-Brownian particle organization

Extending our study of non-Brownian particle assembly to other particle types, sizes and shapes may bring about new applications for non-Brownian particle based crystals. For example, HCP configurations have a packing density of 74% but other orientations pack less densely. These less densely packed crystals may be more appropriate when it comes to certain applications such as templating inverted crystals for insulation materials. Conversely, varying the shape of the particle may allow for more densely packed domains[69] which could prove advantageous in applications

such as separations. Throughout this thesis we have systematically explored HCP orientations of spherical particles but have not addressed other configurations such as simple cubic (square packing). Alternate configurations are widely studied on the nanoscale[224] and some of our results suggest that they could be rationally created among microparticles as well. Figure 35 shows an example of a square packed crystalline region bordering on an HCP region in an array made of 15 µm PS spheres. We have seen similar behavior arise among small regions of 100 µm particles as well but need to further investigate how and why they form in this way.

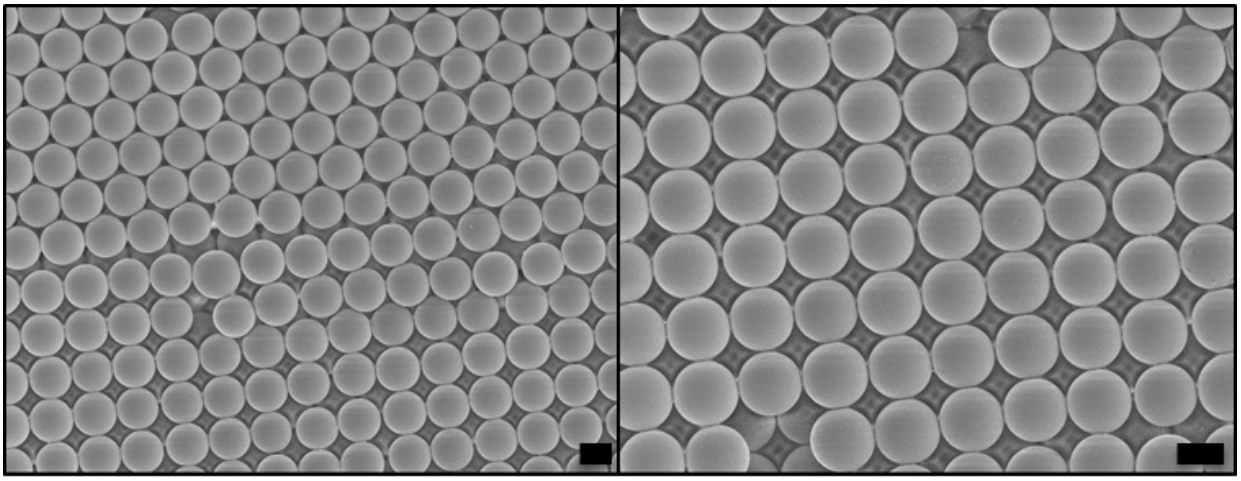

Figure 35: Square packed crystal formed from 15 µm PS. The left hand side shows the transition between HCP and CCP and the right hand side shows a closer view of the CCP array. These structures are multilayered. Scale bars are 10 µm.

8.1.2 Lubrication collapse

The mechanism through which the particles organize when ultrasonic agitation was briefly explored in Chapter 2, however, we only explored the cases where full fluid evaporation occurred. We believe that in the presence of an extreme excess of sonication solvent, the particles will still

tend to cluster as the bath is turned on in a similar way as they did in the work discussed in Chapter 2. Figure 36 shows this behavior in both water and glycerol for soda lime particles 100 μm in diameter. These additional experiments further show that the mechanism behind the particle assembly is closely related to hard spheres behavior when in the absence of confinement (as compared to the confinement imposed in Chapters 2 and 4). In a confined space, hard spheres are expected to form into a close-packed lattice for entropic reasons when their concentration exceeds a certain threshold (see Figure 3 and Ref [27]). However our research shows that these particle systems order even in the absence of confining boundaries (either solid or fluid). We hypothesize that this novel particle clustering behavior is due to new physics that we call "lubrication collapse." Lubrication collapse is reminiscent of "inelastic collapse" in gas-solid and solid-solid flows[63] – where particle clusters are formed due to an instability caused by energy loss through sequential inelastic particle-particle collisions. Additionally, this phenomenon is related to the formation of "hydroclusters", which have been proposed to explain shear thickening of dense hard-sphere suspensions.[225] Here, we believe that particle clustering – *even at small initial concentrations* – is driven by the following process: (1) when the particles are isolated they move at a (roughly randomly-oriented) velocity where the energy from the sonication bath is balanced with the viscous dissipation due to drag on the particles by the fluid; (2) when the inter-particle distance between any particles becomes small (due to random encounters, for example), lubrication forces causes increased drag, thus dissipating more energy and reducing the relative velocity of those particles (essentially creating a minihydrocluster); (3) this "cluster seed" then increases the probability of additional "near miss" encounters with other particles due to the seed's increased size. Thus, the energy dissipation rate grows rapidly as the collision probability continues to grow

until we reach a local solids fraction high enough to induce a fully aggregated state among the particles (i.e., the hard sphere crystallization limit is *locally* reached).

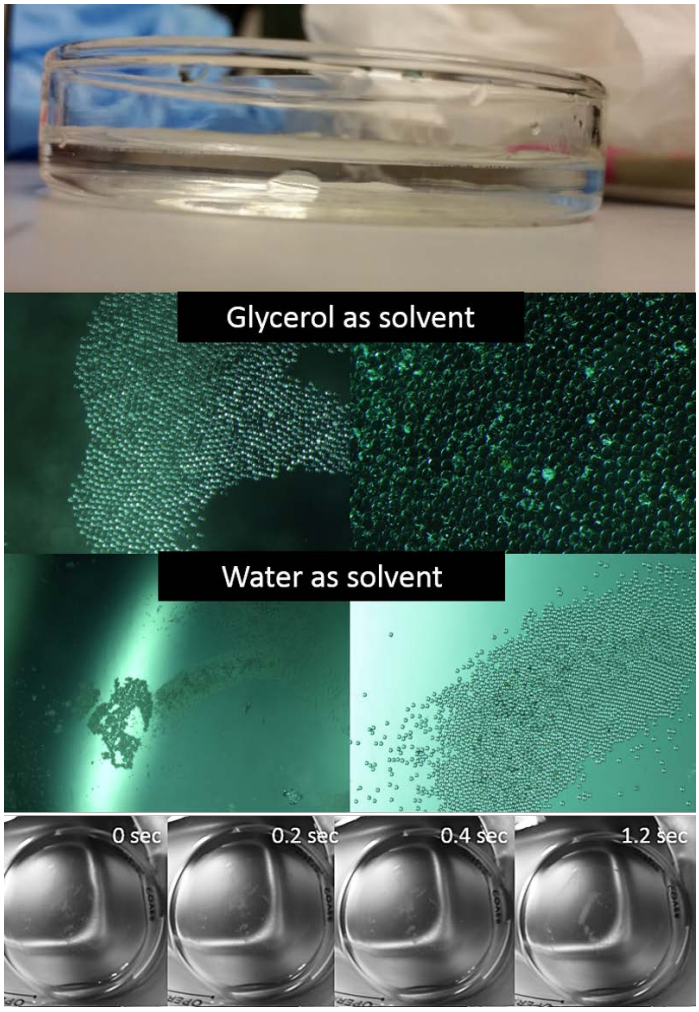

Figure 36: The top image shows the glass dish used as the substrate, showing the approximate height of fluid in comparison to the 100 μm soda lime particles seen on the bottom of the dish. The solvents used were glycerol and water. A very dilute mixture of particles in solution was added to the glass dish and placed (starting in a dispersed state) in the sonication bath. After 2-10 minutes the bath was turned off and the particles were imaged while fully submerged in the glass dish. The bottom row shows 100 μm SL particle clustering behavior in DIW in the first 1.2 seconds. Behavior in glycerol was comparable.

Further experimental and computational testing of the "lubrication collapse" phenomena should be conducted to help explain this new physics. In these experiments, the influence of particle size as well as solution viscosity (liquid solutions and air) should be tested independently for their impact on the likelihood of particle clustering and the emergence of crystallization. Additionally, using Lattice-Boltzmann and Discrete Element Methods the presence and significance of viscous and lubrication forces between particles can be modeled and used to corroborate the experimental data discussed above.

8.1.3 Applications of non-Brownian particle templates

The work completed in this thesis serves as a proof of concept for the potential applications of this science. We describe preliminary studies conducted to fabricate novel bone engineering scaffolds and monoliths for catalytic reaction engineering and battery materials. Chapters 4-7 independently discuss the next steps involved in taking this research to the next level but here we will describe our vision for future experiments in greater detail.

8.1.3.1 Bone regeneration scaffolds (continuation of work in Chapter 4)

Future studies are aimed at continued scaffold design and the beginning of *in vitro* testing. The scaffolds described in Chapter 4 were produced using polystyrene particles as a template. To improve upon this design we would like to transition to using monodispersed PLGA particles as a template so that these particles could be designed to release desired therapeutic proteins or antibiotics. Additionally, the inclusion of PLGA initially within the scaffold will help provide additional structural support to the scaffold and degrade away slowly as cells infiltrate into the construct and begin producing bone. The PLGA particles will be fabricated in the Little Lab using

a microfluidic device and a double emulsion synthesis process. Mechanical testing of the scaffolds should be conducted to measure the stress-strain response and the material's elasticity when force is applied. Additionally, we would like to measure the pore distribution throughout the scaffold and quantity the *in vitro* drug release to observe how the therapeutic agent encapsulated releases and leaches out of the scaffold over time. Based on the cell infiltration and proliferation response the release schedule will be tuned by altering the PLGA's MW, the drugs encapsulated or possibly changing the polymer used. Upon full characterization of the scaffold *in vitro* and the collection of positive results, *in vivo* testing should be pursued.

8.1.3.2 Catalytic monoliths (continuation of work in Chapter 5)

Designing CEN-based monoliths with macro- and nano-pores has the potential of having a large impact on the industrial scaling of catalytic materials. By forming PBICs through the co-crystallizing of CENs and microparticles, we are creating a structure that will have the capacity to withstand pressure drops and allows for better reaction conversions without the need for added supports. This unique monolith structure also eliminates the safety concern of airborne free NPs and creates high active site availability while maintaining uninterrupted pore diffusion pathways for bulk transport.

To further characterize the material properties of these monoliths in preparation for reactor testing, we will be evaluating how the material responds to tensile and compressive stresses and how well it holds up under simulated flow conditions that will represent those endured within the reactor. Reactor testing and testing conditions will be determined in collaboration with the Veser lab in a similar fashion to those studies completed in Ref [209,226].

In the development and testing of these materials, we are seeking to improve upon the sturdiness of the monoliths we are currently producing. This will allow us more flexibility in

material testing and characterization. Our preliminary materials have not held up well to handling. We firmly believe that making thicker samples (by adding in more NPs) will help to address this current limitation. Additionally, we are developing a new mold with dimensions that will fit the reactor's quartz tubing setup to eliminate the necessity of cutting the monolith and allow us to insert it directly into the reactor for use.

8.1.3.3 Electrode materials (continuation of work in Chapter 6)

Chapter 6 presents our preliminary studies in creating materials for electrode research. This preliminary research in its current state has shortcomings, primarily revolved around the material stability. We are exploring different ratios of "small" to "large" particles as well as increasing the total number of particles and particle fusion temperatures to prepare more robust structures that will not be as highly susceptible to cracking. Creating stronger materials that can be handled without crumbling is crucial to the future battery testing and ultimate success of their research development. Future studies for carbonizing the materials will be conducted in the molds followed by an HF washing cycle and CVD of a silicon semiconductor coating for the transfer of ions between the carbon backbone and the electrolyte fluid. In collaboration with the Kumta Lab we will be pursuing electrochemical testing.[215] Throughout the testing process, iterations of material development will need to be conducted to improve the reproducibility, robustness, and efficiency of these materials as electrodes. Additional characterization of the materials may include but are not limited to surface area and porosity measurements, life cycle analysis, and evaluation of the tensile stress. A similar set of characterization and electrochemical testing experiments should be done for the silicon "foams" in addition to the carbonized PBICs.

9.0 CONCLUSIONS AND FUTURE PERSPECTIVE

Advances in non-Brownian particle science enable bottom-up assembly for a new regime of building blocks capable of producing metamaterials as well as those with naturally-inspired architectures via cost and time-efficient processes.[32,37] By inducing self-assembly to organize non-Brownian particles for macroscale materials design, as described throughout this thesis, the complexity of the material structure can be determined by the building blocks (as a sort of encoded information) rather than by the limitations set forth by the assembler in a top-down assembly process. Non-Brownian particle-based crystals offer distinct advantages (as compared to their Brownian counterparts) due to their larger size. Larger building blocks are easier to produce and visually easier to track (with and without a microscope) leading to improved monitoring of the overall crystallization process. Larger components also provide more user control in the crystallization process (compared to molecules and nanoparticles) in terms of the strength, range and selectivity of the interparticle interactions.[25,26] Non-Brownian particle-based crystals and their inverse structures have created a new subfield of interconnected and readily reproducible scaffolds that are being widely investigated for applications in regenerative medicine and have broad potential across a multitude of other fields.

9.1 PERSPECTIVE ON TRANSLATION FROM BENCH-TOP TO INDUSTRIAL USE

This chapter is adapted from: Lash, M. H., Fedorchak, M. V., McCarthy, J. J., & Little, S. R. (2015). Scaling up self-assembly: Bottom-up approaches to macroscopic particle organization. *Soft Matter*. DOI 10.1039/C5SM00764J.

While the nascent field of non-Brownian particle self-assembly has grown substantially in the past five to ten years with applications of porous materials, ranging from regenerative medicine to photonics, to tackling the age-old problem of granular compaction, there still exists a breach in the literature, however, between nano, micron and granular-scale science. A large majority of research for both microparticle and granular particle systems shows that crystallization occurs as a result of agitation; however the microparticle literature mainly studies wet systems while the granular literature studies mainly dry systems. Additionally, when looking at multicomponent mixtures, the microparticle literature just recently expanded to include studies of co-crystallization to create stoichiometry-mimetic structures in much the same way the nanoparticle literature has done. Granular particle mixtures, however, generally are studied for how they mix and segregate and have not been extended in this way to mimic atomic behavior.[165,227] By studying both wet and dry particle systems across size scales, there lies potential for extending the science behind particle rearrangement to rationally design structures with specific macro-, micro-, and nano- architectures.

Bridging these fields even more in practice will further elucidate interparticle phenomena in a practical and scalable way that can have a significant impact on understanding crystallization at larger scales. For instance, extending the methods leading to spherical non-Brownian particle crystallization on a bench scale can be scaled to create larger crystalline domains as well as to create methods applicable for systems of non-spherical building blocks. Additionally, this type of

understanding can be applied to designing precise packing configurations and achieving desired crystal orientations. Deliberate crystal growth of this kind has the potential to lead to the creation of structures with a variety of functions stemming from different (and customizable) physical properties including mechanical stiffness, structural density, and mass transport potential (derived from the pore size and pore size distribution). Investigating particle behavior at the macro-scale as an extension of what has been thoroughly studied on the nano-scale creates new possibilities for translation of the fundamental science into scalable fabrication methods. Traditionally top-down, assembler-based, fabrication methods have been solely used for assembling large particles since self-assembly of non-Brownian particles has not been developed on an industrial scale.[24,25,228] However, with the increase in knowledge of non-Brownian particle interactions and assembly, this challenge can be overcome to produce uniquely porous materials, featuring complex structures with customizable surface functionalization and multi-scale hierarchy. Exploration into the fabrication and application of non-Brownian particle-based crystals has the potential to transform biomedicine through ICC scaffold creation, enhance the efficiency of ion transport in battery-based materials through high surface area, improve monolith-like catalyst supports for reactor engineering, more precisely filter sound waves for phononics as well as transform the state of the art in a plethora of undiscovered applications to improve human life.

APPENDIX A

EXPLORING A SONICATION PROBE AS THE ULTRASONIC AGITATION SOURCE

Similar experiments to those done with a sonication bath throughout Chapter 2 (see Figure 9 for comparison) were done with a sonication probe at both a 20% and 40% amplitude in a 1.3 L water bath (same volume as sonication bath). These results were generated to test varying impacts of sonication energy in a search for the "necessary" amount/type of energy input to propel these microparticles into motion and promote crystallization. The results, as seen in Figure 37 shows that for 6 μm particles, external agitation is not necessary to promote crystallization. However, as the particle size increases more agitation is needed to induce particle motion, leading to clustering behavior (and subsequent crystallization in the case of 18 μm particles but not 100 μm)

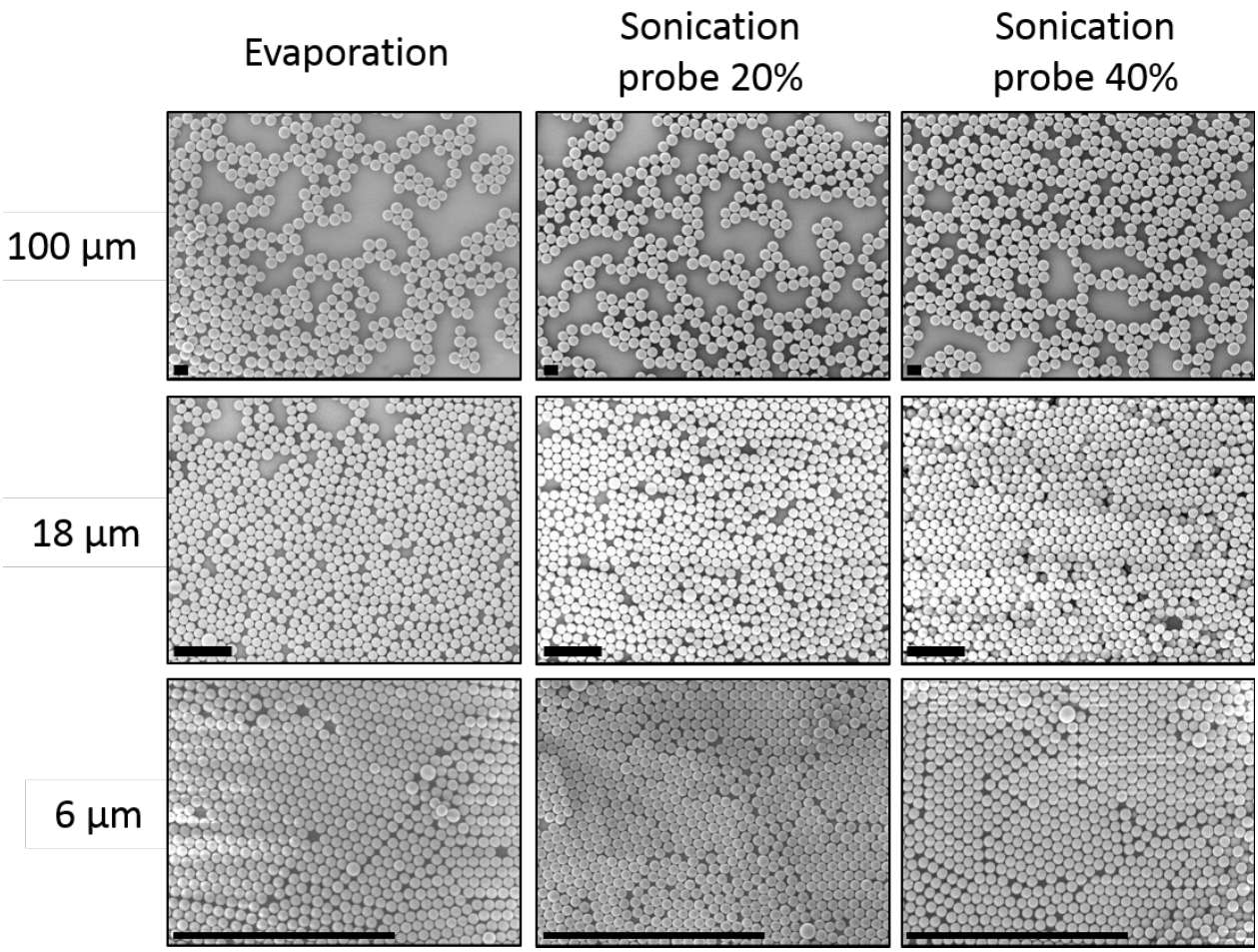

Figure 37: Direct comparison of structures formed via evaporation and with ultrasonic agitation from a sonication probe tuned to 20 and 40% of the maximum amplitude.

This macroscopic particle behavior (or lack thereof) can be further explained in Figure 38, where the dye diffused slightly more when the probe was on (compared to when it was not) but still did not diffuse as fast as in the sonication bath (Figure 7). In terms of particle motion, the water surrounding the particles in our sonication probe samples does not move as much as in the bath, and in turn does not agitate the particles and encourage the same level of motion leading towards crystallization behavior (Figure 39).

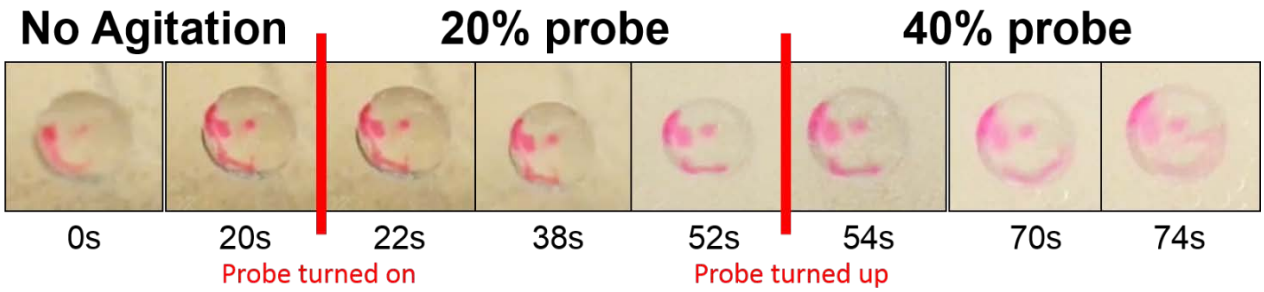

Figure 38: A series of snapshots were taken at even time increments to visually compare fluid motion before and after sonication-based agitation is added via sonication probe-induced agitation. The probe was tuned to two different energy levels, 20 and 40% (of maximum strength).

From a more quantitative view, Figure 39 depicts an analysis of the final structures produced from exposing particles to sonication probe-based agitation. This analysis (explained in Chapter 2.2) of crystallinity includes calculating a packing fraction (Figure 39A), determining the size and prevalence of crystal grains (Figure 39B), and identifying the position of particles in relation to their neighbors (angle between the centers of neighboring particles) (Figure 39C). The most common angle (or mode of the distribution) across all samples fit within a narrow window around 60° (data not shown). Discrepancies, however, are seen in the amount of variation seen per sample. Visually this can be noticed in Figure 39C. All three characterization methods reveal that for the larger, 100 μm particles, each method of adding ultrasonic agitation beyond that naturally experienced during evaporation, enhanced the quality of particle clustering and packing. Comparatively on the lower size limit of this work, for 6 μm particles, the quality of their crystalline structure was largely unchanged by the addition of energy and they organized into an HCP arrangement regardless of the preparation conditions. All experimental data shown was conducted with polystyrene particles. Similar behavior was observed with 100 μm soda lime beads as well (data not shown).

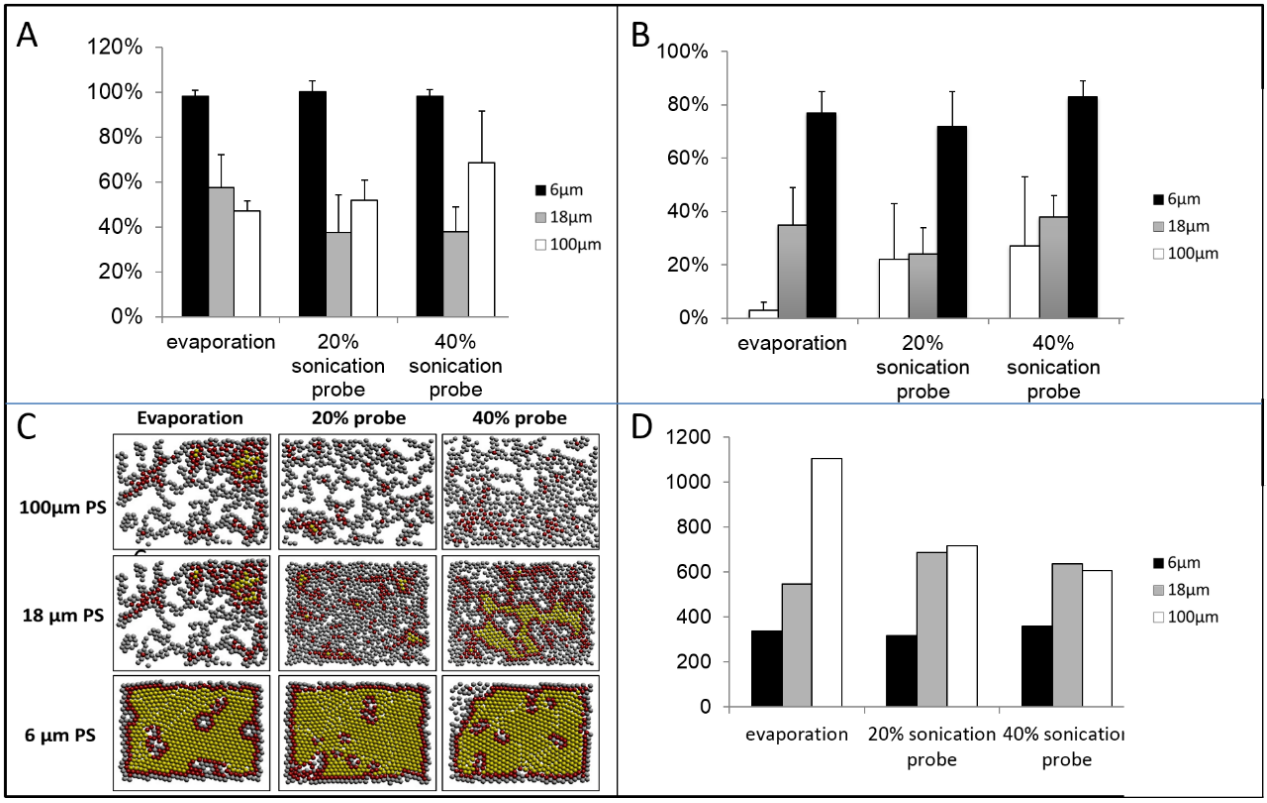

Figure 39: A) Ratio of particle occupied to unoccupied area based on different particle sizes and preparation methods. B) Percentage of particles that lie within a crystal grain. The histogram depicts the percentage of crystal-based particles (red plus yellow as seen in Figure 39C) out of the total number of particles per image. C) Color coded depiction of crystal grains determined by the presence of six nearest neighbors to a given particle and its neighbors. Yellow particles are fully coordinated with all neighbors fully coordinated; red particles are fully coordinated; grey particles are not fully coordinated D) Variance in calculated angles between particles for a packed structure. An ideal HCP arrangement has angles=60°.

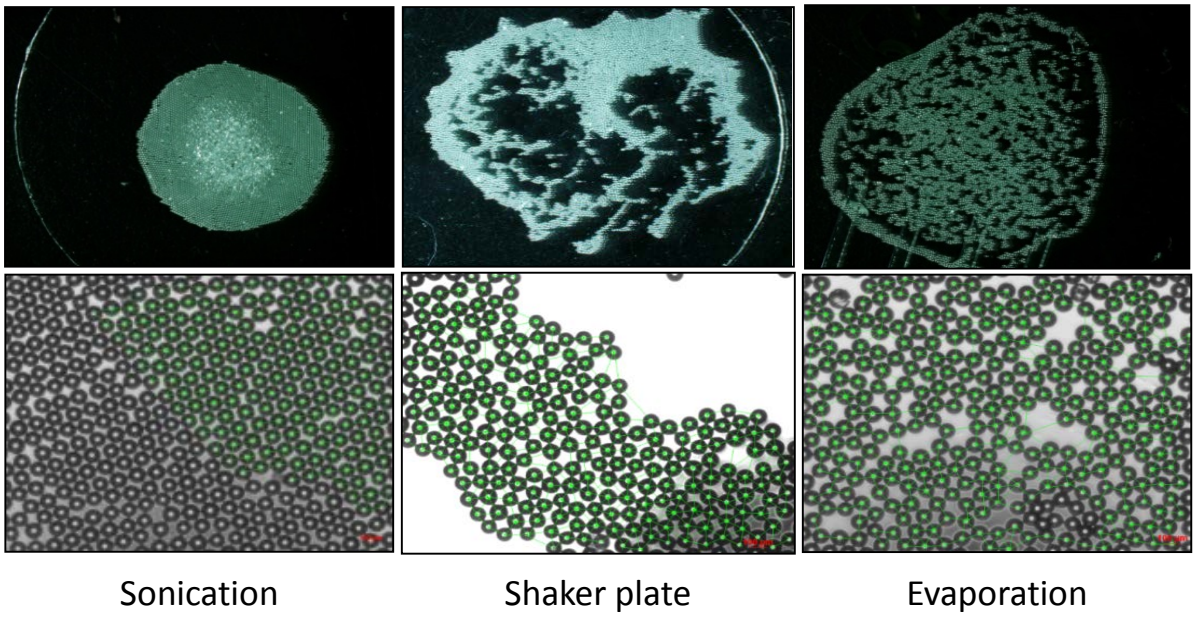

Figure 40: Comparison of packing order induced by various forms of agitation using 100 μm PS particles

APPENDIX B

PARTICLE SURFACE MODIFICATION

When the polystyrene particles were incubated with a primary antibody overnight at room temperature, the AF647 conjugate was much less visible than when incubated at 4 °C. Figure 41A shows polystyrene particles labeled with AF647 and incubated with the primary antibody at room temperature versus 4 °C (Figure 41B). These results suggest that the reactivity is temperature dependent. The AF647 became visible on the surface when the particles were excited with orange visible light. The images show some random aggregation of the AF647 antibody at some portions of the particle surface, which could be reduced by the addition of a surfactant, such as polyethylene glycol (MW=400) prior to incubation. Similar results occurred when polystyrene particles were labeled with AF488 antibody and excited with blue light. Conversely, silica particles were labeled with both green and blue silanes, and the reaction did not have temperature dependence. They also showed uniform labeling across the surface. The green and blue dyes were excited with ultraviolet light. The time required to label silica particles with silane chemistry is considerably less than the time needed to label polystyrene particles with antibodies. Figure 41C shows silica particle labeled with a blue organosilane.

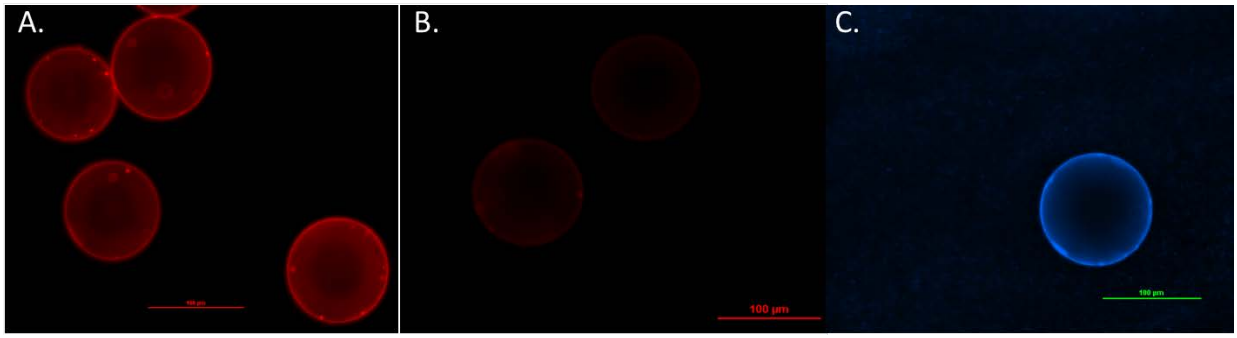

Figure 41:100 µm polystyrene particles activated with EDAC and Sulfo-NHS and incubated overnight at (A) 4°C (B) room temperature (C) 100 µm silica particle labeled with a blue silane.

APPENDIX C

GRANULAR PARTICLE ORGANIZATION

By increasing the size of the particles from the microscale into the granular realm, we sought to explore the possibility of creating stoichiometric configurations by adding agitation (as discussed in Chapter 1.2.3). Preliminary experiments have been conducted with acrylic particles 10 and 2 mm in diameter in a brine, or super-saturated salt water solution (26-28 wt% salt). Brine was chosen due to its higher density than water and minimal viscosity changes. A sonication bath, horizontal shaker plate, vibrating table, and vortex were all explored for their impact on organization. Notably, the sonication bath did not successfully agitate the particles enough to produce gross movement among them. Alternatively, by adjusting shaker plate speed, the amount of agitation can be tuned to induce motion and collisions among the particles. However, at high speeds (rpm) "splashing" of the fluid becomes disruptive to packing. Organization among both particle populations was achieved around 60 rmp. When mixed, the two populations will co-crystallize as seen in Figure 42, where the smaller particles will space fill between the larger ones. When the larger particles are organized and then small particles are added during agitation an LS_2-like configuration is achieved.

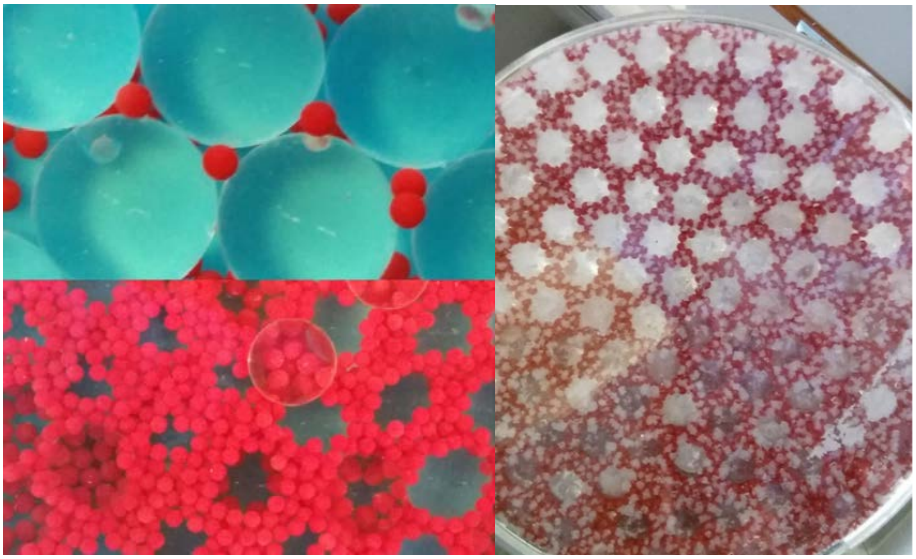

Figure 42: Binary granular crystal of acrylic particles 10 and 2 mm in diameter. By varying the number of each particle size, the organizational configuration changes. 10 mm particles are clear and 2mm particles are red in color. On the left side the large particles were shaken to organize and varying amounts of small particles were then added to the stagnant particle bed. On the right side, the particles were agitated on the shaker plate and the salt water was allowed to evaporate fully prior to imaging. The salt crystallized and remained in the interstitial spaces between the particles.

The crystallized structures are similar to those created in the sonication-based experiments in Chapters 2 and 3, however are likely clustering and organizing from different physics due to the unidirectional agitation and the strong influence of confinement to promote clustering. The vibration table induced motion among the particle in a similar way to the sonication bath but did not effectively induce crystallization like the shaker plate because the energy input was not impactful. Interestingly, the vortex produced an agitation effect most similar to the sonication effects in the case of microparticles. Results can be seen in Figure 43 for granular organization induced by a vortex.

Multilayer arrangements were also studied under these conditions as well and in all case the agitation strong enough to coerce collisions and macroscopic particle rearrangement. In these

studies, long range order was never achieved and the results are relatively inconclusive. An LS_2 configuration, was best achieved when the large particles were first organized and then the small particles were allowed to settle into their interstitial gaps. Co-crystallization did not autonomously occur with agitation. Further exploration into different solvent systems and perhaps a different agitation source should be explored to promote the formation of an LS_2 or LS_6 configuration. Additionally, varying the particle number ratios may help achieve this balance.

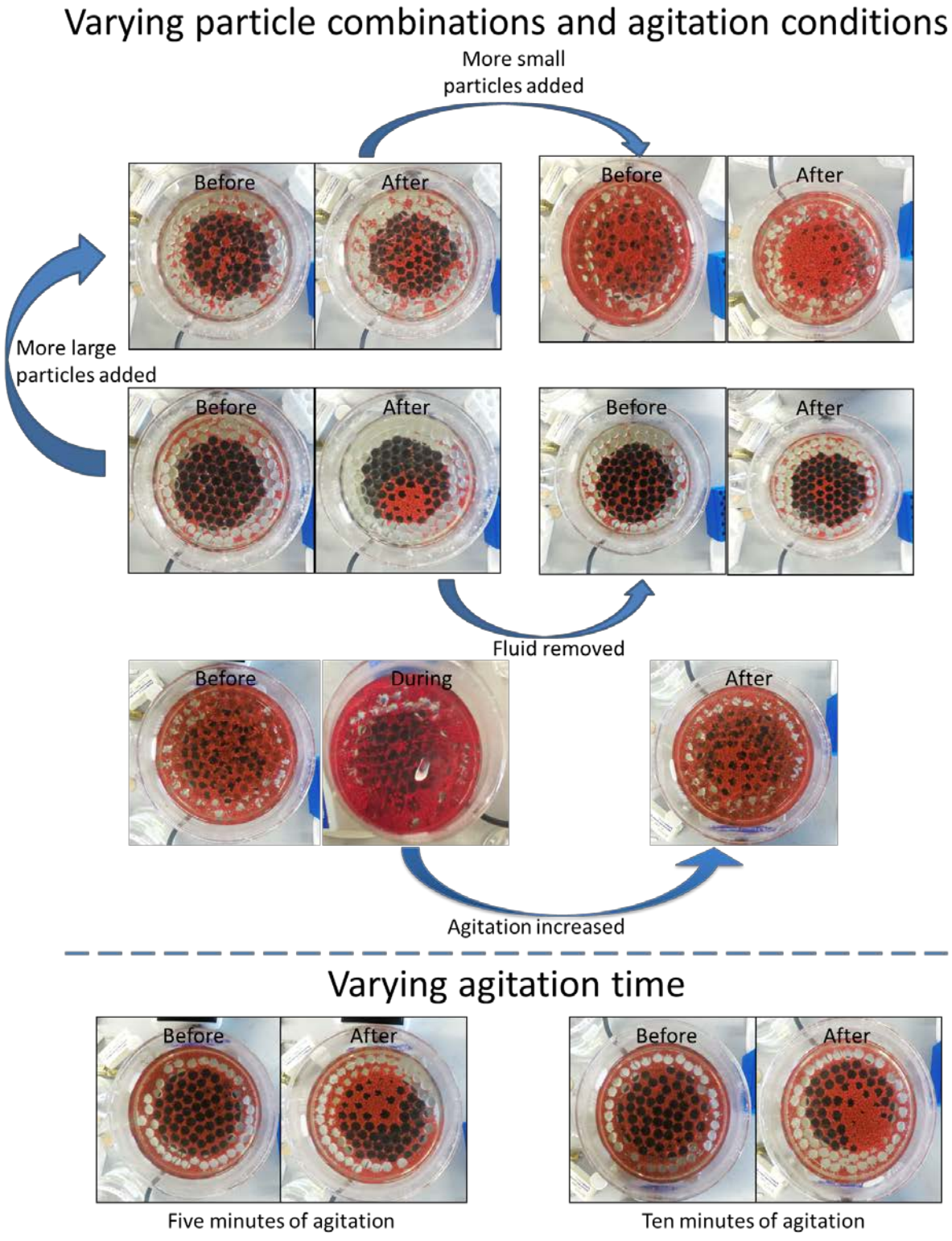

Figure 43: Binary particle mixture of 10 and 2 mm acrylic beads agitated with a vortex under a variety of processing conditions

BIBLIOGRAPHY

[1] Z. Tang, N. A. Kotov, S. Magonov, B. Ozturk, *Nat. Mater.* **2003**, *2*, 413.

[2] K. S. Katti, B. Mohanty, D. R. Katti, *J. Mater. Res.* **2006**, *21*, 1237.

[3] Z. Huang, Z. Pan, H. Li, Q. Wei, X. Li, *J. Mater. Res.* **2014**, *29*, 1573.

[4] Y. Li, Z.-Y. Fu, B.-L. Su, *Adv. Funct. Mater.* **2012**, *22*, 4634.

[5] R. Lakes, *Nature* **1993**, *361*, 511.

[6] S. Bechtle, S. F. Ang, G. A. Schneider, *Biomaterials* **2010**, *31*, 6378.

[7] T. Sano, C. L. Randow, *JOM* **2012**, *64*, 212.

[8] Z. Zhang, Y.-W. Zhang, H. Gao, *Proc. Biol. Sci.* **2011**, *278*, 1.

[9] A. Wang, J. Huang, Y. Yan, *Soft Matter* **2014**, *10*, 3362.

[10] R. C. Hardie, *Curr. Biol.* **2012**, *22*, R12.

[11] M. Friedrich, *Integr. Comp. Biol.* **2003**, *43*, 508.

[12] J. Lim, J. Crespo-Barreto, P. Jafar-Nejad, A. B. Bowman, R. Richman, D. E. Hill, H. T. Orr, H. Y. Zoghbi, *Nature* **2008**, *452*, 713.

[13] J. P. Li, S. H. Li, C. a Van Blitterswijk, K. de Groot, *J. Biomed. Mater. Res. A* **2005**, *73*, 223.

[14] I. Solomonov, D. Talmi-Frank, Y. Milstein, S. Addadi, A. Aloshin, I. Sagi, *Sci. Rep.* **2014**, *4*, 1.

[15] P. Ball, *Nature* **2007**, *449*, 10.

[16] F. H. Kaatz, A. Bultheel, T. Egami, *Naturwissenschaften* **2008**, *95*, 1033.

[17] R. M. L. Guimarães, B. C. Ball, C. a. Tormena, *Soil Use Manag.* **2011**, *27*, 395.

[18] P. Ball, *Archit. Des.* **2012**, *82*, 22.

[19] Z. Guo, W. Liu, B. L. Su, *Appl. Phys. Lett.* **2008**, *93*, 1.

[20] G. M. Whitesides, B. A. Grzybowski, *Science* **2002**, *295*, 2418.

[21] R. L. Jack, M. F. Hagan, D. Chandler, *Phys. Rev. E - Stat. Nonlinear, Soft Matter Phys.* **2007**, *76*, 1.

[22] D. J. Campbell, E. R. Freidinger, J. M. Hastings, M. K. Querns, *J. Chem. Educ.* **2002**, *79*, 201.

[23] B. Sweeney, T. Zhang, R. Schwartz, *Biophys. J.* **2008**, *94*, 772.

[24] L. Cademartiri, K. J. M. Bishop, *Nat. Mater.* **2014**, *14*, 2.

[25] M. Boncheva, D. Bruzewicz, G. M. Whitesides, *Pure Appl. Chem.* **2003**, *75*, 621.

[26] B. R. Groq, M. Dorigo, *Proc. IEEE* **2008**, *96*, 1490.

[27] O. Carvente, J. Ruiz-Suárez, *Phys. Rev. E* **2008**, *78*, 011302.

[28] D. Klotsa, R. L. Jack, *Soft Matter* **2011**, *7*, 6294.

[29] M. H. Lash, M. V. Fedorchak, S. R. Little, J. J. McCarthy, *Langmuir* **2015**, *31*, 898.

[30] N. Bowden, M. Weck, I. S. Choi, G. M. Whitesides, *Acc. Chem. Res.* **2001**, *34*, 231.

[31] Y. a Diaz Fernandez, T. a Gschneidtner, C. Wadell, L. H. Fornander, S. Lara Avila, C. Langhammer, F. Westerlund, K. Moth-Poulsen, *Nanoscale* **2014**, *6*, 14605.

[32] M. Boncheva, G. M. Whitesides, *MRS Bull.* **2005**, *30*, 736.

[33] N. D. Petkovich, A. Stein, *Chem. Soc. Rev.* **2013**, *42*, 3721.

[34] A. Stein, B. E. Wilson, S. G. Rudisill, *Chem. Soc. Rev.* **2013**, *42*, 2763.

[35] M. Maldovan, *Nature* **2013**, *503*, 209.

[36] O. Carvente, G. G. Peraza-Mues, J. M. Salazar, J. C. Ruiz-Suárez, *Granul. Matter* **2012**, *14*, 303.

[37] G. M. Whitesides, M. Boncheva, *Proc. Natl. Acad. Sci. U. S. A.* **2002**, *99*, 4769.

[38] R. Kubo, *Reports Prog. Phys.* **2002**, *29*, 255.

[39] X. C. Jiang, Q. H. Zeng, C. Y. Chen, a. B. Yu, *J. Mater. Chem.* **2011**, *21*, 16797.

[40] Y. Li, T. Kunitake, S. Fujikawa, *Colloids Surfaces A Physicochem. Eng. Asp.* **2006**, *275*, 209.

[41] A. Yethiraj, *Soft Matter* **2007**, *3*, 1099.

[42] S.-W. Choi, I. W. Cheong, J.-H. Kim, Y. Xia, *Small* **2009**, *5*, 454.

[43] K. J. Lee, J. Yoon, S. Rahmani, S. Hwang, S. Bhaskar, S. Mitragotri, J. Lahann, *Proc. Natl. Acad. Sci. U. S. A.* **2012**, *109*, 16057.

[44] Y. S. Zhang, J. Yao, L. V Wang, Y. Xia, *Polymer (Guildf).* **2014**, *55*, 445.

[45] S. K. Y. Tang, R. Derda, A. D. Mazzeo, G. M. Whitesides, *Adv. Mater.* **2011**, *23*, 2413.

[46] N. A. Kotov, Y. Liu, S. Wang, C. Cumming, *Langmuir* **2004**, *20*, 7887.

[47] Y. Liu, S. Wang, J. W. Lee, N. A. Kotov, *Chem. Mater.* **2005**, *17*, 4918.

[48] H. M. Santos, C. Lodeiro, J.-L. Capelo-Martinez, in *Ultrasound Chem. Anal. Appl.* (Ed.: José-Luis Capelo-Martínez), **1998**, pp. 17–20.

[49] Y. Zhang, S. Wang, M. Eghtedari, M. Motamedi, N. A. Kotov, *Adv. Funct. Mater.* **2005**, *15*, 725.

[50] M. J. Cuddihy, N. A. Kotov, *Tissue Eng. Part A* **2008**, *14*, 1639.

[51] J. E. Nichols, J. Cortiella, J. Lee, J. A. Niles, M. J. Cuddihy, S. Wang, J. Bielitzki, A. Cantu, R. Mlcak, E. Valdivia, R. Yancy, M. L. McClure, N. A. Kotov, *Biomaterials* **2009**, *30*, 1071.

[52] M. J. Cuddihy, Y. Wang, C. Machi, J. H. Bahng, N. A. Kotov, *Small* **2013**, *9*, 1008.

[53] S.-W. Choi, J. Xie, Y. Xia, *Adv. Mater.* **2009**, *21*, 2997.

[54] S.-W. Choi, Y. Zhang, S. Thomopoulos, Y. Xia, *Langmuir* **2010**, *26*, 12126.

[55] A. N. Stachowiak, A. Bershteyn, E. Tzatzalos, D. J. Irvine, *Adv. Mater.* **2005**, *17*, 399.

[56] A. N. Stachowiak, D. J. Irvine, *J. Biomed. Mater. Res. A* **2008**, *85*, 815.

[57] Y. Zhang, S.-W. Choi, Y. Xia, *Macromol. Rapid Commun.* **2012**, *33*, 296.

[58] Y. Nahmad-Molinari, J. Ruiz-Suárez, *Phys. Rev. Lett.* **2002**, *89*, 264302.

[59] Z. Cheng, W. Russel, P. Chaikin, *Nature* **1999**, *401*, 893.

[60] O. Carvente, J. Ruiz-Suárez, *Phys. Rev. Lett.* **2005**, *95*, 018001.

[61] A. Panaitescu, A. Kudrolli, *Phys. Rev. E* **2014**, *90*, 1.

[62] J. Chopin, A. Kudrolli, *Phys. Rev. Lett.* **2011**, *107*, 1.

[63] J. Olafsen, J. Urbach, *Phys. Rev. Lett.* **1998**, *81*, 4369.

[64] A. Yu, X. An, R. P. Zou, R. Y. Yang, K. Kendall, *Phys. Rev. Lett.* **2006**, *97*, 265501.

[65] C. X. Li, X. Z. An, R. Y. Yang, R. P. Zou, A. B. Yu, *Powder Technol.* **2011**, *208*, 617.

[66] O. Pouliquen, M. Nicolas, P. D. Weidman, *Phys. Rev. Lett.* **1997**, *79*, 3640.

[67] A. Panaitescu, K. A. Reddy, A. Kudrolli, *Phys. Rev. Lett.* **2012**, *108*, 1.

[68] T. C. Hales, *J. Comput. Appl. Math.* **1992**, *44*, 41.

[69] E. R. Chen, D. Klotsa, M. Engel, P. F. Damasceno, S. C. Glotzer, *Phys. Rev. X* **2014**, *4*, 011024.

[70] A. Donev, I. Cisse, D. Sachs, E. a Variano, F. H. Stillinger, R. Connelly, S. Torquato, P. M. Chaikin, *Science* **2004**, *303*, 990.

[71] S. Torquato, T. M. Truskett, P. G. Debenedetti, *Phys. Rev. Lett.* **2000**, *84*, 2064.

[72] S. M. Allen, E. L. Thomas, *The Structure of Materials*, **1999**.

[73] V. Prasad, D. Semwogerere, E. R. Weeks, *J. Phys. Condens. Matter* **2007**, *19*, 113102.

[74] N. W. Mueggenburg, H. M. Jaeger, S. R. Nagel, *Phys. Rev. E - Stat. Nonlinear, Soft Matter Phys.* **2002**, *66*, 1.

[75] N. Sushko, P. Van Der Schoot, *Phys. Rev. E - Stat. Nonlinear, Soft Matter Phys.* **2005**, *72*, 6.

[76] E. Nowak, J. Knight, E. Ben-Naim, H. Jaeger, S. Nagel, *Phys. Rev. E* **1998**, *57*, 1971.

[77] Y. Koh, C. Wong, *Langmuir* **2006**, *22*, 897.

[78] E. C. H. Ng, K. M. Chin, C. C. Wong, *Langmuir* **2011**, *27*, 2244.

[79] Q. Chen, L. Zhu, C. Zhao, Q. Wang, J. Zheng, *Adv. Mater.* **2013**, *25*, 4171.

[80] K. Singh, M. Tirumkudulu, *Phys. Rev. Lett.* **2007**, *98*, 1.

[81] O. Cedex, L. Limat, *Phys. Rev. Lett.* **1995**, *74*, 2981.

[82] Y. K. Koh, L. K. Teh, C. C. Wong, *Thin Solid Films* **2008**, *516*, 5637.

[83] W. Han, B. Li, Z. Lin, *ACS Nano* **2013**, *7*, 6079.

[84] C. H. Yi, Y. Liu, T. De Miao, Q. S. Mu, Y. L. Qi, *Granul. Matter* **2007**, *9*, 195.

[85] N. D. Petkovich, A. Stein, *Chem. Soc. Rev.* **2013**, *42*, 3721.

[86] H. Iddir, H. Arastoopour, C. M. Hrenya, *Powder Technol.* **2005**, *151*, 117.

[87] U. G. K. Wegst, H. Bai, E. Saiz, A. P. Tomsia, R. O. Ritchie, *Nat. Mater.* **2014**, *14*, 23.

[88] Z. Zhang, Y.-W. Zhang, H. Gao, *Proc. Biol. Sci.* **2011**, *278*, 1.

[89] N. Brun, S. R. S. Prabaharan, C. Surcin, M. Morcrette, H. Deleuze, M. Birot, O. Babot, M. F. Achard, R. Backov, *J. Phys. Chem. C* **2012**, *116*, 1408.

[90] G. Singh, S. Pillai, A. Arpanaei, P. Kingshott, *Adv. Funct. Mater.* **2011**, *21*, 2556.

[91] J. Wang, Q. Li, W. Knoll, U. Jonas, *J. Am. Chem. Soc.* **2006**, *128*, 15606.

[92] Z. Cai, J. Teng, Y. Wan, X. S. Zhao, *J. Colloid Interface Sci.* **2012**, *380*, 42.

[93] M. H. Lash, J. C. Jordan, L. C. Blevins, M. V. Fedorchak, S. R. Little, J. J. McCarthy, *Angew. Chem. Int. Ed. Engl.* **2015**, *54*, 5854.

[94] E. C. M. Vermolen, A. Kuijk, L. C. Filion, M. Hermes, J. H. J. Thijssen, M. Dijkstra, A. van Blaaderen, *Proc. Natl. Acad. Sci. U. S. A.* **2009**, *106*, 16063.

[95] R. Radhakrishnan, B. L. Trout, in *Handb. Mater. Model.*, **2005**, pp. 1613–1626.

[96] A. R. Kansal, T. M. Truskett, S. Torquato, *J. Chem. Phys.* **2000**, *113*, 4844.

[97] M. D. Rintoul, S. Torquato, *J. Chem. Phys.* **1996**, *105*, 9258.

[98] B. Klumov, Y. Jin, H. Makse, *Soft Condens. Matter* **2013**, 1.

[99] C. R. Wassgren, M. L. Hunt, P. J. Freese, J. Palamara, C. E. Brennen, *Phys. Fluids* **2002**, *14*, 3439.

[100] N. Boechler, G. Theocharis, C. Daraio, *Nat. Mater.* **2011**, *10*, 665.

[101] C. Daraio, V. F. Nesterenko, E. B. Herbold, S. Jin, *Phys. Rev. E - Stat. Nonlinear, Soft Matter Phys.* **2006**, *73*, 1.

[102] C. Li, L. Qi, *Adv. Mater.* **2010**, *22*, 1494.

[103] A. Vantomme, A. Léonard, Z. Y. Yuan, B. L. Su, *Colloids Surfaces A Physicochem. Eng. Asp.* **2007**, *300*, 70.

[104] E. DeGiuli, G. Düring, E. Lerner, M. Wyart, *Soft Condens. Matter* **2014**, 1.

[105] A. Haji-Akbari, M. Engel, A. S. Keys, X. Zheng, R. G. Petschek, P. Palffy-Muhoray, S. C. Glotzer, *Nature* **2009**, *462*, 773.

[106] P. Richard, M. Nicodemi, R. Delannay, *Nat. Mater.* **2005**, 121.

[107] D. B. Cines, T. Lebedeva, C. Nagaswami, V. Hayes, W. Massefski, R. I. Litvinov, L. Rauova, T. J. Lowery, J. W. Weisel, *Blood* **2014**, *123*, 1596.

[108] Y. S. Zhang, S.-W. Choi, Y. Xia, *Soft Matter* **2013**, *9*, 9747.

[109] C. F. C. João, J. M. Vasconcelos, J. C. Silva, J. P. Borges, *Tissue Eng. Part B. Rev.* **2014**, *20*, 437.

[110] J. Lee, M. J. Cuddihy, G. M. Cater, N. A. Kotov, *Biomaterials* **2009**, *30*, 4687.

[111] T. K. Nguyen, O. Carpentier, P. Herin, P. Hivart, *Transp. Porous Media* **2012**, *96*, 255.

[112] S. Shanbhag, J. Woo Lee, N. A. Kotov, *Biomaterials* **2005**, *26*, 5581.

[113] Y. Zhang, K. Regan, Y. Xia, *Macromol. Rapid Commun.* **2013**, *34*, 485.

[114] K. Takagi, T. Takahashi, K. Kikuchi, A. Kawasaki, *J. Eur. Ceram. Soc.* **2010**, *30*, 2049.

[115] X. Cai, Y. Zhang, L. Li, S.-W. Choi, M. R. MacEwan, J. Yao, C. Kim, Y. Xia, L. V Wang, *Tissue Eng. Part C. Methods* **2013**, *19*, 196.

[116] F. M. Klenke, Y. Liu, H. Yuan, E. B. Hunziker, K. a Siebenrock, W. Hofstetter, *J. Biomed. Mater. Res. A* **2008**, *85*, 777.

[117] S.-W. Choi, Y. Zhang, Y. Xia, *Langmuir* **2010**, *26*, 19001.

[118] S. Zhu, D. Zhang, Z. Chen, G. Zhou, H. Jiang, J. Li, *J. Nanoparticle Res.* **2010**, *12*, 2445.

[119] Y. M. Soliman, M. F. Su, Z. C. Leseman, C. M. Reinke, I. El-Kady, R. H. Olsson, *Appl. Phys. Lett.* **2010**, *97*, 45.

[120] Y. Xia, B. Gates, Y. Yin, Y. Lu, *Adv. Mater.* **2000**, *12*, 693.

[121] J.-T. Zhang, N. Smith, S. A. Asher, *Anal. Chem.* **2012**, *84*, 6416.

[122] M. Rycenga, P. H. C. Camargo, Y. Xia, *Soft Matter* **2009**, *5*, 1129.

[123] D. J. Beltran-Villegas, M. a. Bevan, *Soft Matter* **2011**, *7*, 3280.

[124] S.-H. Kim, J.-M. Lim, S.-K. Lee, C.-J. Heo, S.-M. Yang, *Soft Matter* **2010**, *6*, 1092.

[125] F. Li, D. P. Josephson, A. Stein, *Angew. Chem. Int. Ed. Engl.* **2011**, *50*, 360.

[126] P. N. Poon, W.C.K.; Pusey, *Obs. Predict. Simul. phase transitions complex fluids* **1995**, 3.

[127] A. J. Goldmant, R. G. Cox, H. Brenner, *Chem. Eng. Sci.* **1967**, *22*, 653.

[128] P. Colson, R. Cloots, C. Henrist, *Langmuir* **2011**, *27*, 12800.

[129] P. Jiang, T. Prasad, M. J. McFarland, V. L. Colvin, *Appl. Phys. Lett.* **2006**, *89*, 011908.

[130] Z. Zhou, X. S. Zhao, *Langmuir* **2004**, *20*, 1524.

[131] Z. Cai, J. Teng, Q. Yan, X. S. Zhao, *Colloids Surfaces A Physicochem. Eng. Asp.* **2012**, *402*, 37.

[132] J. H. Fendler, *Chem. Mater.* **1996**, *4756*, 1616.

[133] J. Zhang, Y. Li, X. Zhang, B. Yang, *Adv. Mater.* **2010**, *22*, 4249.

[134] A. S. Dimitrov, K. Nagayama, *Langmuir* **1996**, *12*, 1303.

[135] N. D. Denkov, O. D. Velev, P. A. Kralchevsky, I. B. Ivanov, H. Yoshimura, K. Nagayama, *Nature* **1993**, *361*.

[136] L. Malaquin, T. Kraus, H. Schmid, E. Delamarche, H. Wolf, *Langmuir* **2007**, *23*, 11513.

[137] N. B. Crane, O. Onen, J. Carballo, Q. Ni, R. O. Guldiken, *Microfluid. Nanofluidics* **2012**, *14*, 383.

[138] K. Kamalasanan, S. Jhunjhunwala, J. Wu, A. Swanson, D. Gao, S. R. Little, *Angew. Chem. Int. Ed. Engl.* **2011**, *50*, 8706.

[139] M. Mastrangeli, S. Abbasi, C. Varel, C. Van Hoof, J.-P. Celis, K. F. Böhringer, *J. Micromech. Microeng.* **2009**, *19*, 83001.

[140] E. C. H. Ng, Y. K. Koh, C. C. Wong, in *Mod. Asp. Bulk Cryst. Thin Film Prep.*, **2012**.

[141] J. J. F. Spengler, W. T. Coakley, *Langmuir* **2003**, *19*, 3635.

[142] Q. Ye, M. Loisiou, B. L. Levine, M. M. Suhoski, J. L. Riley, C. H. June, G. Coukos, D. J. Powell, *J. Transl. Med.* **2011**, *9*, 131.

[143] T. H. Besseling, M. Hermes, a. Fortini, M. Dijkstra, a. Imhof, a. van Blaaderen, *Soft Matter* **2012**, *8*, 6931.

[144] J. Cai, X. Huai, S. Liang, X. Li, *Front. Energy Power Eng. China* **2009**, *4*, 313.

[145] S.-H. Yang, S. S.-Y. Jaw, K. K.-C. Yeh, *Exp. Fluids* **2009**, *47*, 343.

[146] R. R. H. Liu, J. Yang, M. Z. M. Pindera, M. Athavale, P. Grodzinski, *Lab Chip* **2002**, *2*, 151.

[147] Branson Ultrasonics, *Ultrasonic Cleaners Operating Manual*, **n.d.**

[148] M. Elwenspoek, L. Abelmann, E. Berenschot, J. van Honschoten, H. Jansen, N. Tas, *J. Micromechanics Microengineering* **2010**, *20*, 064001.

[149] Z. P. Zhang, A. Yu, R. Oakeshott, *J. Phys. A …* **1996**, *2671*, 2671.

[150] K. D. Danov, P. A. Kralchevsky, *Adv. Colloid Interface Sci.* **2010**, *154*, 91.

[151] N. D. Denkov, O. D. Velev, P. A. Kralchevsky, I. B. Ivanov, H. Yoshimura, K. Nagayamat, *Langmuir* **1992**, *8*, 3183.

[152] U. Gasser, E. R. Weeks, A. Schofield, P. N. Pusey, D. A. Weitz, *Science* **2001**, *292*, 258.

[153] G. C. Agbangla, É. Climent, P. Bacchin, *Comput. Fluids* **2014**, *94*, 69.

[154] X. Ye, L. Qi, *Sci. China Chem.* **2013**, *57*, 58.

[155] Z. Cai, Y. J. Liu, X. Lu, J. Teng, *ACS Appl. Mater. Interfaces* **2014**, *6*, 10265.

[156] H. Yang, X. Dou, Y. Fang, P. Jiang, *J. Colloid Interface Sci.* **2013**, *405*, 51.

[157] N. J. Lorenz, H. J. Schöpe, H. Reiber, T. Palberg, P. Wette, I. Klassen, D. Holland-Moritz, D. Herlach, T. Okubo, *J. Phys. Condens. Matter* **2009**, *21*, 464116.

[158] K. J. M. Bishop, C. E. Wilmer, S. Soh, B. A. Grzybowski, *Small* **2009**, *5*, 1600.

[159] J. Zheng, Z. Dai, F. Mei, X. Xiao, L. Liao, W. Wu, X. Zhao, J. Ying, F. Ren, C. Jiang, *J. Phys. Chem. C* **2014**, *118*, 20521.

[160] L. Wang, Y. Wan, Y. Li, Z. Cai, H. Li, X. Zhao, Q. Li, *Langmuir* **2009**, *25*, 6753.

[161] T. Muangnapoh, A. L. Weldon, J. F. Gilchrist, *Appl. Phys. Lett.* **2013**, *103*, 181603.

[162] J. S. Vesaratchanon, A. Nikolov, D. Wasan, D. Henderson, *Ind. Eng. Chem. Res.* **2009**, *48*, 6641.

[163] R. Dickman, P. Attard, V. Simonian, *J. Chem. Phys.* **1997**, *107*.

[164] A. Jain, M. J. Metzger, B. J. Glasser, *Powder Technol.* **2013**, *237*, 543.

[165] M. J. Metzger, B. Remy, B. J. Glasser, *Powder Technol.* **2011**, *205*, 42.

[166] R. Brito, R. Soto, *Eur. Phys. J.* **2009**, *179*, 207.

[167] Z. Xie, P. Wu, S. Wang, Y. Huang, S. Zhang, S. Chen, C. Jia, C. Liu, L. Wang, *Soft Matter* **2013**, *9*, 5074.

[168] R. Thiruvengadathan, V. Korampally, A. Ghosh, N. Chanda, K. Gangopadhyay, S. Gangopadhyay, *Rep. Prog. Phys.* **2013**, *76*, 066501.

[169] N. Vogel, L. de Viguerie, U. Jonas, C. K. Weiss, K. Landfester, *Adv. Funct. Mater.* **2011**, *21*, 3064.

[170] Z. Dai, Y. Li, G. Duan, L. Jia, W. Cai, *ACS Nano* **2012**, *6*, 6706.

[171] S. V. Karpov, I. L. Isaev, a. P. Gavrilyuk, V. S. Gerasimov, a. S. Grachev, *Colloid J.* **2009**, *71*, 329.

[172] J. Wang, S. Ahl, Q. Li, M. Kreiter, T. Neumann, K. Burkert, W. Knoll, U. Jonas, *J. Mater. Chem.* **2008**, *18*, 981.

[173] M. Retsch, U. Jonas, *Adv. Funct. Mater.* **2013**, *23*, 5381.

[174] Y. Wan, Z. Cai, L. Xia, L. Wang, Y. Li, Q. Li, X. S. Zhao, *Mater. Lett.* **2009**, *63*, 2078.

[175] C. M. Andres, M. L. Fox, N. A. Kotov, *Chem. Mater.* **2012**, *24*, 9.

[176] S.-W. Choi, Y. Zhang, M. R. Macewan, Y. Xia, *Adv. Healthc. Mater.* **2013**, *2*, 145.

[177] B. Suki, R. Lutchen, *J. Appl. Physiol.* **1994**, *76*, 2749.

[178] S. Shanbhag, S. Wang, N. A. Kotov, *Small* **2005**, *1*, 1208.

[179] Z. Schwartz, B. D. Boyan, *J. Cell. Biochem.* **1994**, *56*, 340.

[180] J. R. Porter, T. T. Ruckh, K. C. Popat, *Biotechnol. Prog.* **2009**, *25*, 1539.

[181] J. S. Carson, M. P. G. Bostrom, *Injury* **2007**, *38*, DOI 10.1016/j.injury.2007.02.008.

[182] N. H. Dormer, C. J. Berkland, M. S. Detamore, *Ann. Biomed. Eng.* **2010**, *38*, 2121.

[183] M. Singh, C. Berkland, M. S. Detamore, *Tissue Eng. Part B. Rev.* **2008**, *14*, 341.

[184] K. Lin, C. Wu, J. Chang, *Acta Biomater.* **2014**, *10*, 4071.

[185] P. N. Kumta, C. Sfeir, D.-H. Lee, D. Olton, D. Choi, *Acta Biomater.* **2005**, *1*, 65.

[186] T. Albrektsson, C. Johansson, *Eur. Spine J.* **2001**, 96.

[187] K. Kikuchi, K. Ikeda, R. Okayasu, K. Takagi, A. Kawasaki, *Mater. Sci. Eng. A* **2011**, *528*, 8292.

[188] S. Pronk, D. Frenkel, *Phys. Rev. Lett.* **2003**, *90*, 255501.

[189] S. C. Balmert, S. R. Little, *Adv. Mater.* **2012**, *24*, 3757.

[190] S. N. Rothstein, S. R. Little, *J. Mater. Chem.* **2011**, *21*, 29.

[191] P. Q. Ruhe, E. L. Hedberg, N. T. Padron, P. H. M. Spauwen, J. A. Jansen, A. G. Mikos, *J. Bone Joint Surg. Am.* **2003**, *85-A Suppl*, 75.

[192] A. J. Glowacki, R. Gottardi, S. Yoshizawa, F. Cavalla, G. P. Garlet, C. Sfeir, S. R. Little, *Ann. Biomed. Eng.* **2014**, *43*, 593.

[193] D. Olton, J. H. Li, M. E. Wilson, T. Rogers, J. Close, L. Huang, P. N. Kumta, C. Sfeir, *Biomaterials* **2007**, 1267.

[194] D. Y. E. Olton, J. M. Close, C. S. Sfeir, P. N. Kumta, *Biomaterials* **2011**, 7662.

[195] M. Borden, S. F. El-Amin, M. Attawia, C. T. Laurencin, *Biomaterials* **2003**, *24*, 597.

[196] S. Cohen, T. Yoshioka, M. Lucarelli, L. H. Hwang, R. Langer, *Pharm. Res.* **1991**, *8*, 713.

[197] A. J. Glowacki, R. Gottardi, S. Yoshizawa, F. Cavalla, G. P. Garlet, C. Sfeir, S. R. Little, *Ann. Biomed. Eng.* **2014**, *43*, 593.

[198] A. Zaki, J. Xu, G. Stoclet, S. Casale, J.-P. Dacquin, P. Granger, *Microporous Mesoporous Mater.* **2015**, *208*, 140.

[199] Y.-S. Kim, X.-F. Guo, G.-J. Kim, *Catal. Today* **2010**, *150*, 91.

[200] S. G. Rudisill, Z. Wang, A. Stein, *Langmuir* **2012**, *28*, 7310.

[201] G. Veser, *Catal. Today* **2010**, *157*, 24.

[202] G. Guan, R. Zapf, G. Kolb, Y. Men, V. Hessel, H. Loewe, J. Ye, R. Zentel, *Chem. Commun. (Camb).* **2007**, *1*, 260.

[203] R. Karinen, K. Vilonen, M. Niemelä, *ChemSusChem* **2011**, *4*, 1002.

[204] G. Groppi, E. Tronconi, *Chem. Eng. Sci.* **2000**, *55*, 2161.

[205] N. Kränzlin, M. Niederberger, *Adv. Mater.* **2013**, *25*, 5599.

[206] V. Tomašić, F. Jović, *Appl. Catal. A Gen.* **2006**, *311*, 112.

[207] S. Hartmann, A. Sachse, A. Galarneau, *Materials (Basel).* **2012**, *5*, 336.

[208] F. Li, Z. Wang, N. S. Ergang, C. a Fyfe, A. Stein, *Langmuir* **2007**, *23*, 3996.

[209] L. Whaley, Synthesis and Evaluation of Metal-Silica Core-Shell Nanomaterials for Catalysis, University of Pittsburgh, **2012**.

[210] C. Gao, Z. Lu, Y. Yin, *Langmuir* **2011**, *27*, 12201.

[211] M. Retsch, U. Jonas, *Adv. Funct. Mater.* **2013**, *23*, 5381.

[212] A. Stein, *Microporous Mesoporous Mater.* **2001**, *44-45*, 227.

[213] S. Bhavsar, M. Najera, R. Solunke, G. Veser, *Catal. Today* **2014**, *228*, 96.

[214] H. Yang, P. Jiang, *J. Colloid Interface Sci.* **2010**, *352*, 558.

[215] R. Epur, P. J. Hanumantha, M. K. Datta, D. Hong, B. Gattu, P. N. Kumta, *J. Mater. Chem. A* **2015**, *3*, 11117.

[216] Y. Yao, M. T. McDowell, I. Ryu, H. Wu, N. Liu, L. Hu, W. D. Nix, Y. Cui, *Nano Lett.* **2011**, *11*, 2949.

[217] N. Wang, B. J. P., D. E. Ingber, *Science (80-.).* **1993**, *260*, 1124.

[218] A. Grakoui, S. K. Bromley, C. Sumen, M. M. Davis, A. S. Shaw, P. M. Allen, M. L. Dustin, *Science* **1999**, *285*, 221.

[219] B. Prakken, M. Wauben, D. Genini, R. Samodal, J. Barnett, A. Mendivil, L. Leoni, S. Albani, *Nat. Med.* **2000**, *6*, 1406.

[220] A. A. Shah, B. Schultz, K. L. Kohlstedt, S. C. Glotzer, M. J. Solomon, *Langmuir* **2013**, *29*, 4688.

[221] A. B. Pawar, I. Kretzschmar, *Macromol. Rapid Commun.* **2010**, *31*, 150.

[222] H. Bao, W. Peukert, R. N. K. Taylor, *Adv. Mater.* **2011**, *23*, 2644.

[223] T. Soukka, H. Härmä, J. Paukkunen, T. Lövgren, *Anal. Chem.* **2001**, *73*, 2254.

[224] P. Kumnorkaew, Y.-K. Ee, N. Tansu, J. F. Gilchrist, *Langmuir* **2008**, *24*, 12150.

[225] N. J. Wagner, J. F. Brady, *Phys. Today* **2009**, *62*, 27.

[226] S. Bhavsar, M. Najera, G. Veser, *Chem. Eng. Technol.* **2012**, *35*, 1281.

[227] K. Strandburg, F. Prinz, R. H. Swendsen, *Phys. Rev. Lett.* **1987**, *58*, 1038.

[228] S. K. Chung, S. K. Cho, *Microfluid. Nanofluidics* **2008**, *6*, 261.